UNIVERSITY OF CALIFORNIA
SANTA CRUZ

FAST RADIO BURSTS: THEIR LOCAL ENVIRONMENTS AND APPLICATIONS TO MAGNETIC FIELD MEASUREMENTS

A dissertation submitted in partial satisfaction of the
requirements for the degree of

DOCTOR OF PHILOSOPHY

in

ASTRONOMY & ASTROPHYSICS

by

Alexandra G. Mannings

June 2025

The Dissertation of
Alexandra G. Mannings is approved:

Professor Jason Xavier Prochaska, Chair

Assistant Professor Nia Imara

Professor Andrew Skemer

Associate Professor Wen-fai Fong

Dean Bryan Gaensler

Dr. Peter F. Biehl
Vice Provost and Dean of Graduate Studies

Table of Contents

List of Figures

List of Tables

Abstract

Fast Radio Bursts: Their Local Environments and Applications to Magnetic Field Measurements

by

Alexandra G. Mannings

Two primary questions that exist within the field of fast radio bursts (FRBs) are: "What are the sources of Fast Radio Bursts?" and "How can they serve our understanding of magnetism in the universe?". This has been against the backdrop of a quickly-evolving field with an ever-changing understanding of this mysterious phenomenon. This thesis is a story told in a few parts: (i) an introduction to the world of FRBs; (ii) a look into my work on characterizing the local environments surrounding these bursts, and any connections this may have with their burst properties or any similarities to other transient classes; and (iii) a test of whether or not we can use FRBs as probes of the magnetic fields in their host galaxies. My works find a tentative connection between FRBs and spiral arms which I explore further in subsequent chapters. I develop more rigorous methods of testing this possible relationship between FRBs and spiral structure by measuring the minimum distance between a spiral arm and the FRB position. We find that most FRBs are at distances less than 1 kpc from the nearest arm, tracing the distributions of Type II and Ia relative to spiral arms in their respective hosts. I also explore the connections between burst and local characteristics and find a tentative positive correlation between stellar mass surface density and scattering times. Finally, I explore the power of FRBs to measure magnetic field strengths in their host galaxies. My findings show that we can indeed use FRBs to probe galactic magnetic fields.

To my friends and family.

Acknowledgments

Thank you to my mother for her support throughout my life. Your presence has been such a tremendous gift in my life, and has gotten me to where I am now. To my father, thank you for the random stories and wonderful chats. Your spirit is a light that keeps me going. To my brothers, you are both such wonderful people that I am blessed to call friends. I am glad that I get to be tied to you for life. To Sierra, thank you for all of the laughs, hugs, and shopping sprees. I cannot imagine my life without you, and I am the luckiest person in the world to call you a friend. To my siblings and housemates, Tenley and Arcelia: you both have been my rocks and the best people to live with. The love that has grown within me towards you both will last the rest of my life. I am so blessed to live with and love such beautiful people. To my friend Kat: thank you or making me feel so loved and silly and joyous. Thank you for keeping my love for dance alive and even changing my relationship to it. Meeting you has forever changed me. To Veriche, thank you for the opportunity to know and love the silly, caring, wonderful person that you are. I will never find another bike baddie like you, and I hope many more bike rides and play dates await us. To my friends Maddy and Jules, I will never forget our bubble times, and I am so excited to meet you all on this side of graduation and dissertating! To my fellow slugbugs: going through grad school with you all has been such a treat. I am lucky to be surrounded by such caring, empathetic, kind people. Thank you to my committee for all of your efforts to ensure this came to fruition and that my future career is fulfillig. To my previous mentors — Regina, Mordecai, KD, Jeremy, Krista, Jana, Andrew, Rebecca, Lawrence, and so many more: thank you for all of your support, guidance, teaching, and mentorship. Thank you to the friends I have made along the way and whose paths have crossed mine and made it all the brighter — Rosa, Mike, Kate, Annette, and so many more. Rosa and Mike, your influence on my life cannot be exaggerated. I think about your love, kindness, and insights constantly. To

anyone, not mentioned by name: know that your love, support, and presence live within these pages and my heart. Thank you.

Chapter 1

An Introduction to Fast Radio Bursts

1.1 Transients and Mysterious Origins

The first supernova in recorded history was observed by Chinese astronomers in the year 185 C.E.. They observed the presence of a "guest star" over the course of eight months. Over the course of the 20th century, scientists came to understand that the life-ending processes of stars can result in incredibly bright explosions that can be seen over vast distances. Through the efforts of theorists and observers, scientists built an understanding of the workings of stars, their fuel sources, their lifetimes, what happens when they run out of fuel, and what the remnants they leave behind look like. These transformations in our knowledge and technological capabilities completely overhauled our understanding of stars and the universe as a whole.

It was not until 2006 that the specific origins of this almost 2000 year old "guest star" were revealed. For decades, scientists knew that a supernova must have occurred, and that is what the Chinese astronomers recorded. However, in 2006, further inspection of what remains of the supernova pointed scientists towards a specific *kind* of supernova that they had not suspected as the source initially. They found that it must — instead of a core-collapse supernova resulting

from a massive star 10 or more times as massive as our sun — have come from a Type Ia supernova. When our sun eventually runs out of fuel, it will likely turn into a white dwarf. If we were to plop another, puffy star next to this white dwarf, the white dwarf might collect material from its puffy neighbor until one day, it explodes! This gives us a Type Ia supernova. Finally, the 2000-year-old mystery was solved (Hill, 2023).

The tapestry of Astrophysics is filled with these kinds of stories; beginning with a strange observation and ending with new understandings of the workings of the universe. We can see this being especially true for events called "transients". These events are special because they occur and change on timescales that humans can observe during the course of their lifetimes. Supernovae, for example, are transient events. They brighten and fade on timescales that range from days to years — allowing scientists to understand the full time evolution of such events.

1.2 The Mystery of Fast Radio Bursts

In 2007, a new mystery excited radio astronomers. Only a year after our supernova mystery was solved, Fast Radio Bursts perplexed observers. They appeared in archival data of pulsars — rapidly rotating remnants of massive stars left behind after a core-collapse supernova. However, they were far too bright and quick to be a pulsar signal. It also became clear that the origin of these bursts reached beyond our own Milky Way galaxy. Pulsars that we detect are within the Galaxy, and therefore have a low dispersion measure (DM). Different wavelengths of light travel through mediums at different velocities, and while we often assume space is a vacuum, in reality, it is full of ionized material. Dispersion measure is the result of the different frequencies contained within a single burst interacting with that ionized material and arriving to detectors at slightly different times — resulting in a characteristic "sweep" (see Figure 1.1.) The dispersion measure can then be given as

$$\mathrm{DM} = \int \frac{\mathrm{n_e}}{(1+\mathrm{z})}\mathrm{dl} \tag{1.1}$$

which is the integrated electron density (n_e) along some path length (dl; generally from observer to burst). Generally, sources within the Milky Way have dispersion measures of approximately 40 DM units ($\mathrm{pc\,cm^{-3}}$), but FRBs often show DMs well above this threshold — pointing towards mysterious, extragalactic origins. Closer investigation of the bursts also showed that the signals are polarized and interact with magnetic fields along their propagation path. These interactions result in Faraday rotation, which is the rotation of the plane of oscillations for polarized emission. The rotation measure (RM) is given as

$$\mathrm{RM} = \int \frac{\mathrm{B_\parallel n_e}}{(1+\mathrm{z})^2}\mathrm{dl} \tag{1.2}$$

where $B_\parallel$ is the component of the magnetic field parallel to the line of sight or path of propagation. The change in polarization angle (Θ) is frequency dependent and can be shown as

$$\Theta = \mathrm{RM}\,\lambda^2 \tag{1.3}$$

where lambda is the wavelength.

Additionally, FRBs can be scattered by turbulent material, which causes the signal to propagate along multiple paths. This results in temporal broadening where parts of the signal that traveled along longer paths, arrive to the detector later. Where DM describes the total amount of ionized material along the line of sight, scattering describes its fluctuations and distribution. The scattering measure is given as

$$\mathrm{SM} = \int \mathrm{C^2_{n_e}(l)dl} \tag{1.4}$$

where $C^2_{n_e}$ describes the strength of the fluctuations along the path length.

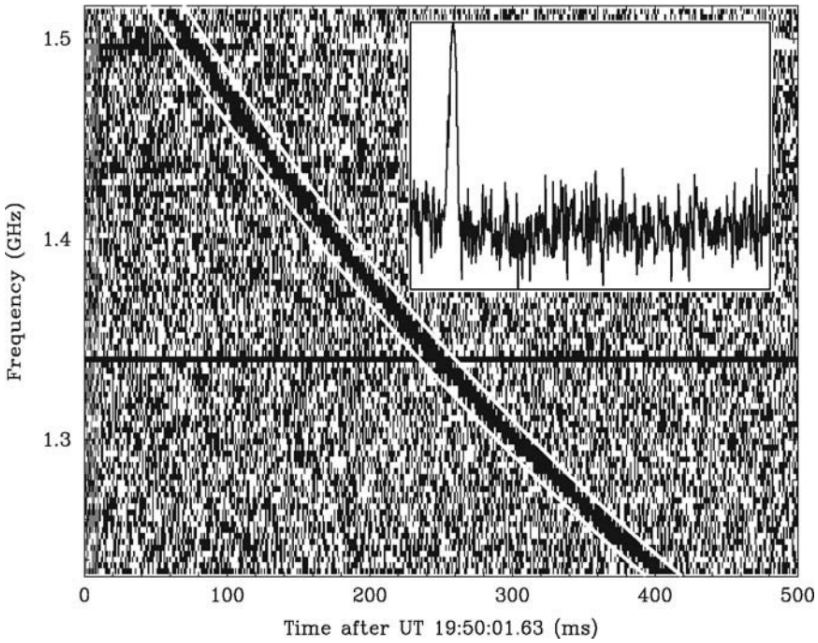

Figure 1.1: Figure showing the signal of the first FRB published (Lorimer et al., 2007).

With these burst characteristics, it was also apparent that FRBs could be used to understand characteristics of the universe overall — where ionized material is located, its density, the strength of magnetic fields throughout the universe, etc.

After finding this first burst in 2007, it became clear that there should be dedicated searches to try and detect FRB-like bursts for confirmation. While searches went on, many questions arose about what the origins of these powerful bursts could be. Do they come from black holes? Are they connected to massive star death through supernovae? Are magnetic fields involved? A comprehensive list of theories was put forward by Platts et al. (2019). The intrinsic FRB properties and the characteristics of their host galaxies promised to illuminate the answers to these questions.

From that point onward, dedicated searches for Fast Radio Bursts found more and more events. This effort included experiments such as the Commensal Real-Time ASKAP Fast

Transient (CRAFT) Survey, the Canadian Hydrogen Intensity Mapping Experiment (CHIME) Survey, and more! Some bursts repeated while others were only one-off occurrences (e.g. Bannister et al., 2017; Spitler et al., 2016). The bursts that repeated allowed observers to produce highly precise localizations and confirm the extragalactic origin of Fast Radio Bursts, associating bursts to other galaxies (Marcote et al., 2017, 2020).

1.3 From Big to Small: FRB Localizations

First, most localizations were on the order of arcminutes, sometimes encompassing multiple possible host galaxies (Eftekhari and Berger, 2017). Studies such as this proved helpful and informative, but the depth of the studies was greatly limited by the inability to make robust host associations. As time went on, the CRAFT survey was able to precisely localize one-off bursts as well, greatly increasing the number of FRBs with secure host associations (Bannister et al., 2019). This enabled an explosion in host galaxy studies that provided incredible information on possible FRB origins (Bhandari et al., 2020b; Heintz et al., 2020).

Fortunately, precise localizations also set the stage for studies that focused on the local environments of FRBs. Through studies such as Fruchter et al. (2006); Fong et al. (2010), and others, we see the importance of high-resolution imaging follow-up of transient events to gain an understanding of their origins, especially in the context of what we know about other transient events. Local environment studies have the potential to uncover which particular stellar populations the bursts originate from. Importantly, these studies make use of Hubble Space Telescope (HST) and ground-based adaptive optics (AO) observations that provide high-resolution imaging that can match the precision of the FRB localizations. HST in particular also provides a broad wavelength coverage that includes NUV which is very challenging to capture from ground-based observations. With this wavelength coverage, we can then understand the distribution of

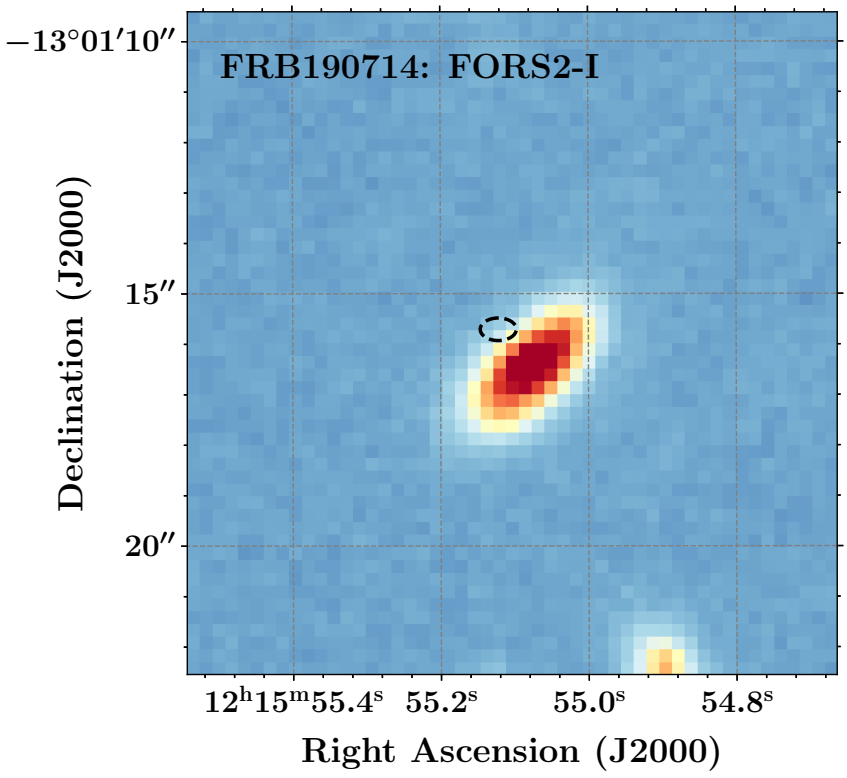

Figure 1.2: Image of the host galaxy of FRB20190714A published by Heintz et al. (2020).

stars that span young to old ages where bluer light traces more recent star-formation, and redder wavelengths trace the general distribution of stellar mass (which also includes older stars).

Beyond host properties, it is becoming clear that present and future progenitor-related studies must make use of burst characteristics in conjunction with local measures as a tool to better understand FRBs as a whole. Much information lies in the burst properties like RM and DM, so we must utilize them to understand what the FRB and its environment are saying about one another.

1.4 This Thesis

My thesis research engages with these questions through the following two broader prongs of FRB studies: (i) source-related studies that elucidate the physical origins of FRBs; (ii) the use of FRBs as probes of otherwise difficult-to-measure properties of the universe. My goals have been this: (i) to utilize high-precision localizations and burst characteristics accompanied by high-resolution, deep imaging to learn more about the particular environment from which FRBs originate, and (ii) combine our knowledge of host/local properties and rotation measures to understand magnetic fields and their connection to galaxy evolution in FRB host galaxies.

Chapter 2 focuses on the first, ever statistical study of FRB local environments using HST imaging. This provided the first look into the specific locations of FRBs within their hosts and the implications for progenitor channels. Chapter 3 builds on this work by making use of ground-based AO resources that expanded the sample of hosts with high-resolution imaging. This proved the efficacy of ground-based resources as a tool for high-resolution follow-up of FRBs, and provided additional information about the locations of FRBs within their hosts. Chapter 4 explores the connections between burst characteristics and their local environments, in order to better understand imprints the local environments may be leaving on the hosts. As researchers

have done for Supernovae and other transients, understanding the energetics, behavior, and characteristics of the transient itself in addition to where it is located in its host, can help paint a much clearer picture of progenitor pathways. I sought to do just that in this study. Finally, Chapter 5 focuses on the second prong of FRB studies: their use as probes of astrophysical properties. We look at the power of FRBs to measure the magnetic field strengths in their host galaxies, and make comparisons to magneto-hydrodynamic simulations to better understand the physical mechanisms of magnetic field generation and amplification. I will end with overall conclusions in Chapter 6.

Chapter 2

The First High-resolution, Statistical Study of FRB Environments

Since the discovery of fast radio bursts (FRBs) in 2007 (Lorimer et al., 2007) – dispersed, millisecond-timescale transients, traced primarily to cosmological distances (Thornton et al., 2013; Cordes and Chatterjee, 2019) – their definitive origins have remained elusive. The emerging association of FRBs with magnetized neutron stars ("magnetars") was catalyzed by the discovery and sub-arcsecond localization of the repeating FRB 121102 (Spitler et al., 2016; Chatterjee et al., 2017; Tendulkar et al., 2017), which was found to be spatially consistent with a compact, persistent radio source (Chatterjee et al., 2017) postulated to be a synchrotron nebula powered by an embedded magnetar (Marcote et al., 2017; Margalit and Metzger, 2018) or an offset active galactic nucleus (AGN; Marcote et al. 2017; Eftekhari et al. 2020). The association of at least some FRBs with magnetars was further solidified by the detection of multiple FRB events from the Galactic magnetar SGR 1935+2154 (CHIME/FRB Collaboration et al., 2020; Bochenek et al., 2020). However, a myriad of progenitor models still exist (Platts et al., 2019; Petroff et al., 2019), and the precise connection to magnetars for the extragalactic population has yet to be made

definitive. Moreover, given the diversity of their observed FRB properties, it is not clear if there is one or multiple progenitor channels for FRB production.

The advent of dedicated FRB experiments are fueling an unprecedented rise in their detection rates (CHIME/FRB Collaboration et al., 2018; Macquart et al., 2010). One of the most promising ways to make progress on their origins is through robust associations to host galaxies, which generally requires precise localizations of $\lesssim 1''$ (Eftekhari and Berger, 2017). Indeed, different progenitor channels will yield distinct host galaxy demographics and host stellar population properties (e.g., Margalit et al. 2019). It is also expected that different production pathways will be imprinted in how FRBs are distributed with respect to their host galaxies. Prior to recent advancements in our ability to localize FRBs, surveys were only able to produce arc-second localizations for repeating bursts such as 121102 and 180916. Repeating bursts, however, are thought to only make up $\simeq 2-5\%$ of all bursts. This means that, as of now, repeating bursts are over-represented in the sample of precisely localized FRBs. With surveys such as CRAFT (Shannon et al., 2018) coming online that provide sub-arcsecond localizations of apparently non-repeating bursts, we can form a more complete picture of FRB host characteristics and therefore production pathways.

Locations have historically played an important role in delineating the progenitors of a wide range of transients. For instance, the spatial distributions and strong correlation with the UV light distributions of their hosts for super-luminous supernovae (SLSNe) and long-duration gamma-ray bursts (LGRBs) is commensurate with their massive star origins (Woosley, 1993; Fruchter et al., 2006; Lunnan et al., 2015; Perley et al., 2016), while the significant offsets of short-duration gamma-ray bursts (SGRBs) and weaker correlation to UV light is indicative of an older stellar progenitor (e.g. Fong and Berger, 2013). Moreover, quantifying the relationship between the locations of core-collapse SNe (CCSNe, Types Ib/c, II) and Type Ia SNe, to detailed morphological features such as spiral arms, can serve as an indirect indicator of the age of their

stellar and/or white dwarf progenitors (Audcent-Ross et al., 2020).

For FRBs, two primary pathways that have been considered for magnetar formation are "prompt" magnetars, formed from massive star progenitors, and "delayed"-channel magnetars, formed from existing compact objects and their interactions, e.g., neutron star mergers or accretion-induced collapse (AIC) of a white dwarf to a NS (Nicholl et al., 2017b; Margalit et al., 2019). Detailed studies using ground-based observations based on the first ∼dozen well-localized FRBs and their host galaxies have shown that their spatial distributions are inconsistent with engine-driven massive star explosions (LGRBs, SLSNe; Li et al. 2019; Bhandari et al. 2020b; Heintz et al. 2020; Bochenek et al. 2020).

One is therefore motivated to characterize, as precisely as possible, the local environments of FRBs within their host galaxies. Furthermore, the competing progenitor models offer distinct predictions for the ages and masses of the responsible compact object(s). For young progenitors, there must be a direct link to ongoing or recent star-formation activity. Older progenitor channels, meanwhile, may track the underlying stellar mass of the galaxy. Thus motivated, we have designed an experiment to examine the local environments of FRBs, in both active star-formation (via near-UV light) and stellar mass (near-IR) and at the highest spatial resolution afforded by space-borne instrumentation.

Against this backdrop, we present the first comprehensive sample of *HST* observations for eight FRB host galaxies, six of which are newly presented in this work. In Section 2.1, we describe our sample, observations and data reduction. In Section 2.2, we present the spatial distribution of FRBs (angular, physical and host-normalized offsets) and the locations of FRBs with respect to their host light distributions. In Section 2.3, we present the results of surface brightness profile fits, including the revelation of spiral structure in several hosts; constraints on the star formation rate and stellar mass densities at the FRB positions; and deep limits on possible satellite or background galaxies. In Section 2.4, we discuss the implications of our results

in terms of FRB progenitors. We highlight our main conclusions in Section 2.5. Throughout the paper, we employ a Planck cosmology with $H_0 = 67.8$ km s^{-1} Mpc^{-1}, $\Omega_M = 0.308$, and $\Omega_\Lambda = 0.692$ (Planck Collaboration et al., 2016). All of the data and analysis code are made available via GitHub[1].

2.1 Data

2.1.1 Sample of FRB Host Galaxies

Here we present observations of eight FRB host galaxies obtained with the Wide-Field Camera 3 using the infrared and ultra-violet-visual channels (WFC3/IR and WFC3/UVIS). The data for six of the FRB host galaxies were collected between October 2019 and April 2020 as part of programs 15878 (PI: Prochaska) and 16080 (PI: Mannings), which targeted galaxies for which FRB events have been detected and localized by the Commensal Real-time ASKAP Fast Transients (CRAFT) survey on the Australian Square Kilometer Array Pathfinder (ASKAP; Bannister et al. 2019; Day et al. 2020; Bhandari et al. 2020b; Chittidi et al. 2021; Macquart et al. 2020). These bursts were localized to sub-arcsecond precision, with $\sigma_{\rm FRB} \approx 0.1 - 0.7''$.

We also include two additional FRB hosts with *HST* observations, FRB20121102A[2] (Bassa et al., 2017) under program 14890 (PI: Tendulkar) taken in February 2017 and FRB 20180916B (Tendulkar et al., 2020) under program 16072 (PI: Tendulkar) taken in July 2020. FRB 20121102A was discovered by the Arecibo telescope (Spitler et al., 2016), and subsequently localized via repeating bursts with the Very Large Array (VLA; Chatterjee et al. 2017), and with European Very Long Baseline Interferometry (VLBI) Network (EVN; Marcote et al. 2017) with $\sigma_{\rm FRB} = 0.0045''$. FRB 20180916B is the closest and most precisely localized FRB with $\sigma_{\rm FRB} = 0.0023''$ (Marcote et al., 2020). Our sample thus comprises all eight FRB host galaxies

[1]https://github.com/FRBs/FRB
[2]The Transient Name Server (TNS) name for this burst is FRB20121102A.

Table 2.1: Data are from programs 15878 (FRB 180924, 190102, 190608, PI: Prochaska), 16080 (FRBs 190711, 190714, and 191001, PI: Mannings), 14890 (FRB 121102, PI: Tendulkar), and 16072 (FRB 180916, PI: Tendulkar). $\sigma_{\rm Host}$ is the 1σ positional uncertainty of the host (RA and Dec components added in quadrature). M_* is the host stellar mass. † S/N of host galaxy is not sufficient to obtain an uncertainty on the position.

Redshift References– Tendulkar et al. (2017); Bannister et al. (2019); Marcote et al. (2020); Bhandari et al. (2020b); Heintz et al. (2020)

FRB	$\rm RA_{Host}$	$\rm Dec_{Host}$	$\sigma_{\rm Host}$	z	M_*	Instrument	Filter	Date	Exp. Time
	(J2000)	(J2000)	(mas)		$(10^9 M_\odot)$			(UT)	(sec)
20121102	$05^{\rm h}31^{\rm m}58.69^{\rm s}$	$+33°08'52.43''$	6.3	0.1927	0.14 ± 0.07	WFC3/IR	F160W	2017 Feb 23	1197
						WFC3/UVIS	F763M	2017 Feb 23	1940
20180916	$01^{\rm h}58^{\rm m}00.29^{\rm s}$	$+65°42'53.09''$	1.8	0.0337	2.15 ± 0.33	WFC3/IR	F110W	2020 Jul 17	5623
						WFC3/UVIS	F673N	2020 Jul 16	2877
20180924	$21^{\rm h}44^{\rm m}25.256^{\rm s}$	$-40°54'00.80''$	0.4	0.3212	13.23 ± 5.06	WFC3/IR	F160W	2019 Nov 27	2470
			3.1			WFC3/UVIS	F300X	2019 Nov 26	2492
20190102	$21^{\rm h}29^{\rm m}39.577^{\rm s}$	$-79°28'32.52''$	14.2	0.2912	3.39 ± 1.02	WFC3/IR	F160W	2020 Jan 14	2470
			—†			WFC3/UVIS	F300X	2019 Oct 07	2776
20190608	$22^{\rm h}16^{\rm m}04.903^{\rm s}$	$-07°53'55.91''$	0.8	0.1177	11.57 ± 0.84	WFC3/IR	F160W	2019 Dec 01	2295
			0.8			WFC3/UVIS	F300X	2019 Oct 11	2400
190711	$21^{\rm h}57^{\rm m}40.613^{\rm s}$	$-80°21'29.05''$	5.2	0.522	0.81 ± 0.29	WFC3/IR	F160W	2020 May 11	2470
			7.7			WFC3/UVIS	F300X	2020 May 09	2780
20190714	$12^{\rm h}15^{\rm m}55.090^{\rm s}$	$-13°01'15.96''$	1.1	0.2365	14.92 ± 7.06	WFC3/IR	F160W	2020 Apr 30	2295
			—†			WFC3/UVIS	F300X	2020 May 19	2396
20191001	$21^{\rm h}33^{\rm m}24.440^{\rm s}$	$-54°44'54.53''$	0.5	0.2340	46.45 ± 18.80	WFC3/IR	F160W	2020 Apr 28	2296
			—†			WFC3/UVIS	F300X	2020 Apr 25	2580

Table 2.2: $a_{\rm stat}, a_{\rm sys}$ are the angular size of the semi-major axis describing the 1σ statistical and systematic uncertainties respectively. b refers to the semi-minor axis. PA is the sky position angle of the error ellipse. Sources without reported systematic error have been incorporated in the statistical. Data from Day et al. (2020); Tendulkar et al. (2017); Marcote et al. (2020); Heintz et al. (2020).

FRB	$\rm RA_{FRB}$	$\rm Dec_{FRB}$	$a_{\rm stat}$	$a_{\rm sys}$	$b_{\rm stat}$	$b_{\rm sys}$	PA
	(J2000)	(J2000)	($''$)	($''$)	($''$)	($''$)	(deg)
20121102	82.994589	33.1479316	0.004	0.00	0.002	0.00	90.0
20180916	29.503126	65.7167542	0.001	0.00	0.001	0.00	0.0
20180924	326.105229	−40.9000278	0.07	0.09	0.06	0.07	0.0
20190102	322.415667	−79.4756944	0.21	0.52	0.17	0.44	0.0
20190608	334.019875	−7.8982500	0.19	0.19	0.18	0.18	90.0
20190611	320.745458	−79.3975833	0.34	0.60	0.32	0.60	0.0
20190711	329.419500	−80.3580000	0.12	0.38	0.07	0.32	90.0
20190714	183.979667	−13.0210278	0.17	0.32	0.10	0.23	90.0
20191001	323.351554	−54.7477389	0.13	0.11	0.08	0.10	90.0
20200430	229.706417	12.3768889	0.01	0.02	0.24	1.00	0.0

for which there exist available *HST* observations. Table 2.1 summarizes all of these data and Table 2.2 summarizes coordinates and the localization errors of the FRBs.

All of the host galaxies in our *HST* sample have spectroscopically-confirmed redshifts. These are considered secure associations[3] with probabilities of chance coincidence of $P_{\rm chance} \lesssim 0.05$ (Heintz et al., 2020) with their most likely host galaxy. The *HST* data for FRB 20121102A and FRB 180916 were previously published by Bassa et al. (2017) and Tendulkar et al. (2020), respectively, while the WFC3/UVIS image for FRB 20190608B and its local environment was previously published and analyzed by Chittidi et al. (2021). All of the remaining *HST* observations are newly presented here. Three of the bursts are known "repeating" FRBs (FRBs 20121102A, 20190711A and 20180916B; Spitler et al. 2016; Kumar et al. 2020) while the remaining bursts

[3]See also Aggarwal et al. (2021) for a Bayesian analysis that reaches similar conclusions.

are apparent "non-repeaters".

We supplement this sample with ground-based data from two other FRB hosts presented by Heintz et al. (2020) with secure host associations (FRB 20190611A and FRB 20200430A) when computing cumulative distributions of offsets in § 2.2.2. Both of these FRBs in the ground-based sample are apparent non-repeaters. Combined, our ground-based and *HST* sample comprises all FRBs with sub-arcsecond localizations discovered over 2012-2020. The exception is FRB 20190614D which does not have a clear host galaxy association (Law et al., 2020), and is not included in the sample.

In current surveys (including this one), repeating bursts are over-represented within the sample of precisely localized FRBs. Because of their repetition, they are more likely to be localized and make up around half of these precisely localized bursts. Only $\sim 4\%$ of FRBs are known to repeat (The CHIME/FRB Collaboration et al., 2021). Differentiating between repeaters and non-repeaters will be important in future studies with larger sample sizes, as the non-repeaters will represent the majority of all FRBs.

2.1.2 Observations

For the WFC3/UVIS observations under programs 15878 and 16080, we use the ultra-wide F300X filter to sample the rest-frame near- and far-ultraviolet (NUV/FUV) wavelengths with the aim of capturing the distribution of star formation in the host galaxies. This filter provides increased throughput in the NUV compared to the standard wide filters (although it has a minor red tail out to $\sim$4000 Å), and is chosen to maximize the signal-to-noise (S/N) in a single orbit of *HST* imaging. To minimize the effects of charge transfer efficiency (CTE) degradation, we set up the observations to position the targets near the readout on amplifier C located on chip 2. We used a 4-point dither pattern to sub-sample the point spread function (PSF) and remove detector artifacts. We increase the line and point spacing by a factor of 5 over

the standard box pattern to remove residual background patterns as described by Rafelski et al. (2015). The data from program 15878 include a 9 e^- post-flash per exposure to reach 12 e^- per pixel background. Recently there was a new recommendation to reach a background of 20e^-, and therefore the data obtained in program 16080 included a 17 e^- post-flash to reach this level (Anderson et al., 2012).

For the WFC3/IR observations under programs 15878 and 16080, we use the F160W filter, the reddest wide filter available with *HST*, to cover the rest-frame optical band to assess the distribution of the stellar mass as traced by older stellar populations. We use SPARS25 and NSAMP15 to ensure that the observations remain in the linear count regime, and obtain clean images by dithering over the known IR "blobs" with a seven-point dither pattern with a factor 3 increase in spacing of the 7 point wide dither pattern provided by Anderson (2016). Finally, the data for FRB 121102 under program 14890 employ a two-point and four-point dither pattern for the WFC3/UVIS and IR observations, while the data for 180916 employ a three point and four-point dither pattern, respectively (Bassa et al., 2017; Tendulkar et al., 2020). The details of these observations are listed in Table 2.1.

2.1.3 Image Processing

The data were retrieved from the Barbara A. Mikulski Archive for Space Telescopes (MAST), and the WFC3/UVIS data are custom calibrated. These data have degraded CTE, and therefore require pixel-based CTE corrections (Anderson et al., 2012). In addition, the degradation requires improved dark, hot pixel, and bias level corrections. First, we use a new correction for the CTE. Second, we apply concurrent superdarks to the data, reducing the blotchy pattern otherwise present (Rafelski et al., 2015). Third, we identify hot pixels in the darks such that the number of hot pixels is consistent as a function of the distance to the readout amplifiers based on the number of hot pixels identified close to the readout. This is accomplished

by modifying the threshold for hot pixel detection as a function of distance to the readout (Prichard et al. in prep). Lastly, we normalize the amplifiers since the applied superbias is based on bias files with insufficient background levels for a pixel based CTE correction. We measure the background level in each amplifier after masking sources, and match the background level between the amplifiers.

To combine the images for each FRB and in each filter, we used the AstroDrizzle routine as part of the DrizzlePac software package (Avila et al., 2015) employing a `pixfrac`= 0.8, `pixscale`= 0.033″ for UVIS images, and 0.064″ for IR images. As part of AstroDrizzle, we also perform cosmic ray removal and sky subtraction. The final drizzled images are shown in Figures 2.1-2.3.

2.2 FRB Locations & Offsets

In this section, we present the locations of the FRBs in our sample with respect to their host galaxy centers. We introduce their angular and physical offsets (θ and δR, respectively), "host-normalized" offsets ($\delta R/r_e$) which are normalized by the half-light radii r_e of their host galaxies, the location with respect to their host galaxy light distribution ("fractional flux"; $\mathrm{F_F}$), and the fraction of light enclosed $\mathrm{F_e}$ within the radius of the FRB.

2.2.1 Astrometry & Uncertainties

We first perform absolute astrometry using sources in common between available deep, optical ground-based imaging and the Gaia DR2 catalog. The ground-based imaging is sourced from the Gemini-North Observatory (FRB 20121102A), Gemini-South Observatory (FRB 20190711A), Very Large Telescope (VLT; FRBs 20190102C, 20190714A, 20191001A), the Dark Energy Survey (DES; FRB 20180924B) and the Sloan Digital Sky Survey (SDSS;

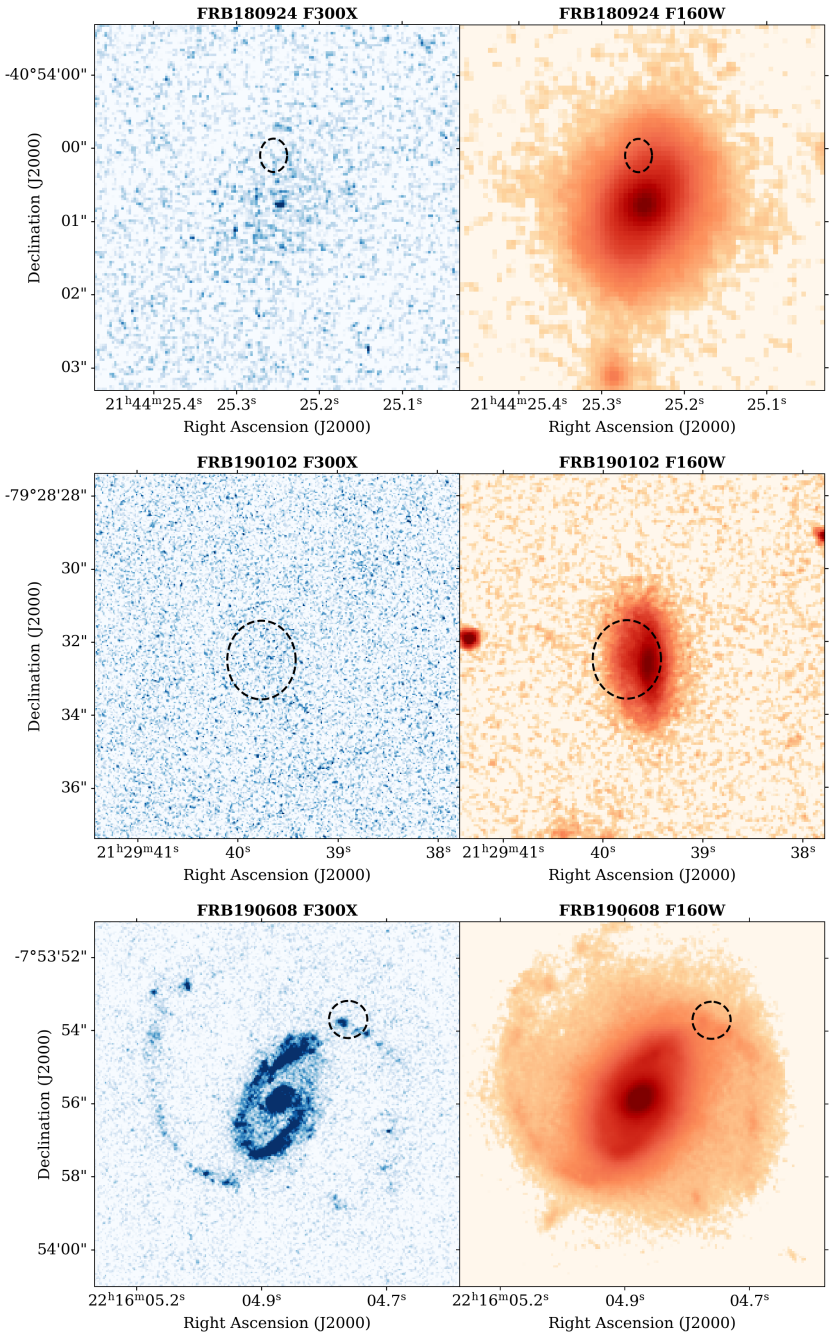

Figure 2.1: *HST* imaging of three of the host galaxies in our sample, for FRB20180924B, FRB20190102C, and FRB20190608B. Blue images were taken with F300X filter, while the images in red color-bar were taken with the F160W filter. The black ellipse in each image denotes the FRB position (2σ uncertainty in each coordinate). All images are oriented with North up and East to the left.

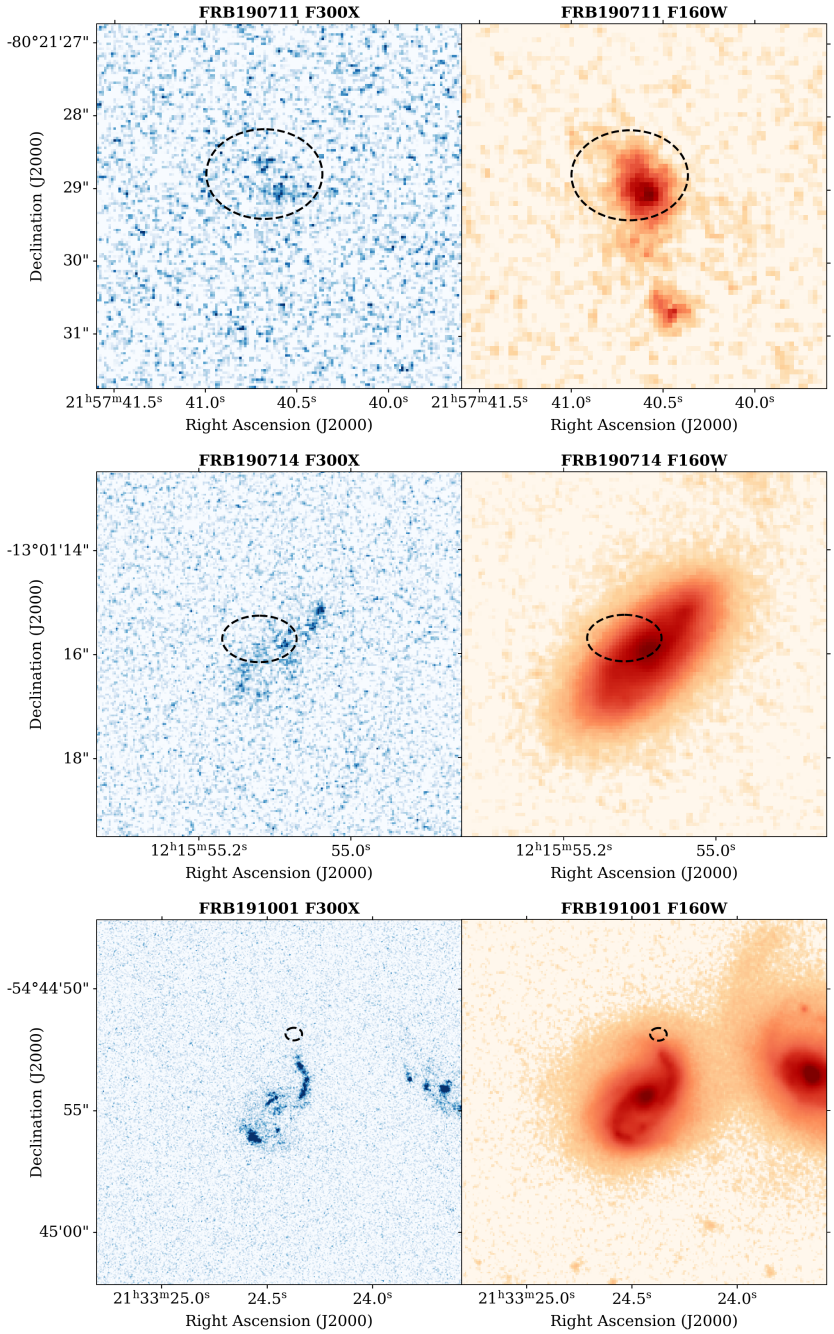

Figure 2.2: *HST* imaging of three of the host galaxies in our sample, for FRB20190711A, FRB20190714A, and FRB20191001A. Color scheme and ellipses are as in Figure 2.2.

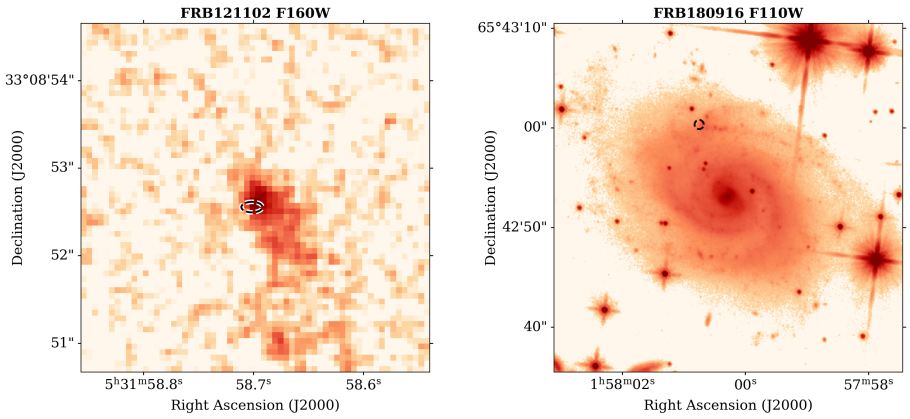

Figure 2.3: *HST* IR imaging of the host galaxies of FRB20121102A (F160W) and FRB20180916B (F110W). The black dashed ellipse represents 30 times the 1σ uncertainty from the VLBI localization for FRB 121102 (Marcote et al., 2017) and 200 times the 1σ uncertainty for FRB 20180916B (Marcote et al., 2020).

FRB 20190608B). We then perform relative astrometry to tie the ground-based images to the WFC3/IR images. This series of astrometric ties ensures that there are enough sources in common with the WFC3 imaging, which has a significantly narrower field-of-view than the ground-based imaging, to properly calculate the total astrometric uncertainty. For astrometry, we employ a six-order polynomial accounting for linear shifts, rotation, and skew, using IRAF/`ccmap` and `ccsetwcs`. We calculate a range of tie uncertainties in each coordinate, of $\sigma_{\rm tie,RA} \approx 0.014-0.073''$ and $\sigma_{\rm tie,Dec} \approx 0.015-0.097''$.

We also use the `SourceExtractor` tool (Bertin and Arnouts, 1996) to determine the FRB galaxy centroid positions and associated uncertainties ($\sigma_{\rm host}$). These positions and values for $\sigma_{\rm host}$ are listed in Table 2.1. The final source of uncertainty is the positional uncertainty of the FRB ($\sigma_{\rm FRB}$), which is derived from the statistical and systematic uncertainties from the FRB detections (Table 2.2).

Table 2.3: FRBs 190611 and 200430 are derived from ground-based imaging as reported by Heintz et al. (2020)

FRB	Filter	θ	δR	$\delta R/r_e$	F_F	F_e
		($''$)	(kpc)			
121102	F160W	0.23 ± 0.02	0.75± 0.05	0.37 ± 0.02	0.70 ± 0.07	0.24 ± 0.12
	F763M				0.67 ± 0.10	
180916	F110W	7.760 ± 0.023	5.386± 0.016	0.897 ± 0.003	0.32 ± 0.07	0.90 ± 0.09
	F673N				0.32 ± 0.25	
180924	F160W	0.71 ± 0.12	3.37± 0.56	1.20 ± 0.20	0.24 ± 0.11	0.66 ± 0.07
	F300X					
190102	F160W	0.80 ± 0.39	2.26± 2.22	0.45 ± 0.44	0.39 ± 0.25	0.25 ± 0.16
	F300X				0.36 ± 0.29	
190608	F160W	2.98 ± 0.27	6.52± 0.60	0.88 ± 0.08	0.19 ± 0.06	0.82 ± 0.08
	F300X				0.39 ± 0.28	
190611	GMOS-S$_r$	2.24 ± 0.66	11.36± 3.59	5.29 ± 1.67		
190711	F160W	0.53 ± 0.27	1.94± 2.30	0.78 ± 0.93	0.55 ± 0.27	0.61 ± 0.22
	F300X					
190714	F160W	0.61 ± 0.29	1.97± 1.18	0.51 ± 0.31	0.34 ± 0.23	0.23 ± 0.10
	F300X				0.38 ± 0.31	
191001	F160W	2.74 ± 0.15	10.49± 0.59	2.87 ± 0.16	0.09 ± 0.03	0.91 ± 0.09
	F300X				0.29 ± 0.25	
200430	Pan-STARRS$_r$	1.30 ± 0.79	2.97± 2.36	1.81 ± 1.44		
Median (IR)		1.1	3.2	0.9	0.33	0.6
16,84% Interval		[0.6,2.9]	[2.0,8.7]	[0.5,2.4]	[0.20,0.53]	[0.2,0.9]
Median (UV)					0.37	
16,84% Interval					[0.32,0.45]	

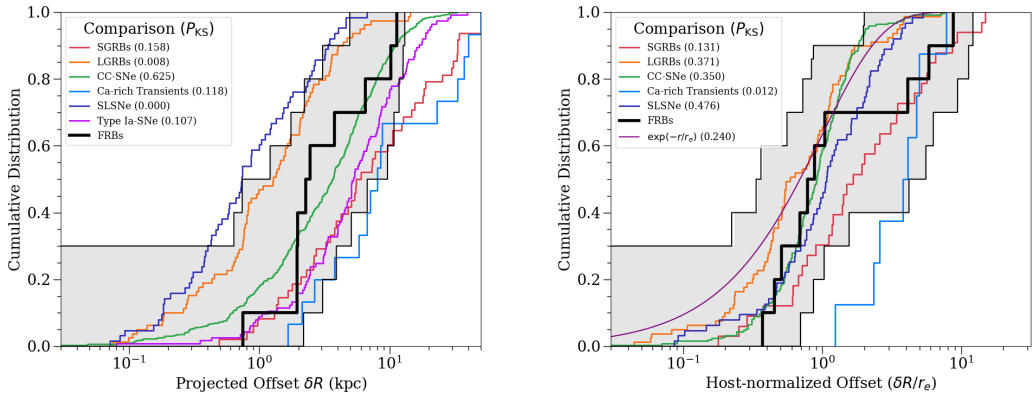

Figure 2.4: *Left:* Cumulative distribution of projected physical offsets, δR, for the 10 FRBs in the *HST* and ground-based samples (black line). The gray shaded region is a bootstrap estimate of the RMS of the distribution, which accounts for both uncertainties on individual measurements, as well as statistical uncertainties due to the sample size. Comparison samples are included for SGRBs (Fong et al., 2010; Fong and Berger, 2013), LGRBs (Blanchard et al., 2016), Ca-rich transients (Lunnan et al., 2017; De et al., 2020), Type Ia SNe (Uddin et al., 2020), CCSNe (Schulze et al., 2020), and SLSNe (Lunnan et al., 2015; Schulze et al., 2020) for events at $z < 1$. The computed P-values from a two-sided KS test are listed for each population relative to the FRB sample. *Right:* The same as the right-hand panel but for the host-normalized offsets ($\delta R/r_e$). This plot also shows the profile of an exponential disk.

2.2.2 Physical & Host-normalized Offsets

Given that FRB localizations are typically non-circular (elliptical) in shape, and that their values span a range ($\sigma_{\rm FRB} \approx 0.0023 - 0.7''$), it is necessary to take their shape, size, and orientation into account when calculating the angular, physical, and host-normalized offsets. While the synthesized beam and hence localization ellipse of the FRB can in principle have any position angle, most FRB detections have been made with beams that are close to circular

and report the positional uncertainties projected onto the right ascension and declination axes, and we construct our localization ellipses using these projected values. To determine the total uncertainty on offset measurements, we sum each of the RA and Dec components of the three sources of uncertainty, $\sigma_{\rm tie}$, $\sigma_{\rm host}$, and $\sigma_{\rm FRB}$ in quadrature. We use the total uncertainties in RA and Dec to define an ellipsoidal region that represents the FRB location on the *HST* image.

The estimated angular offset θ is then the convolution of the offset from the galaxy centroid α_g with the FRB localization:

$$\theta = \int d\omega \, |\alpha_g - \omega| L(\alpha_{\rm FRB} - \omega) \tag{2.1}$$

with L a 2-D Gaussian set by the ellipsoidal region described above. To evaluate this convolution, we divide each 5σ region around the FRB into four million grid points by imposing a 2000×2000-point sub-grid. We measure the angular offset between each grid-point i and the host galaxy center to obtain a distribution of angular offsets θ_i for each FRB. Finally, we apply a 2-D Gaussian probability distribution within the FRB localization ellipse, centered on the central RA and Dec of the FRB, and weight the angular offset distribution by the corresponding values. We estimated the variance in θ in a similar manner and report the RMS in Table 2.3.

For each FRB, we determine the median offset and standard deviation. We find a range of projected angular offsets of $\theta \approx 0.23 - 7.87''$. The values for each FRB are listed in Table 2.3. We note that we only obtained offsets for observations in which the host galaxy center could be well determined, so this includes all hosts for which there are IR images, as well as the host galaxy of FRB 20190608B in both the IR and UV.

We convert the angular offsets to projected physical offsets using the redshift of each FRB host galaxy and a Planck cosmology with $H_0 = 67.8$ km s^{-1} Mpc^{-1}, $\Omega_M = 0.308$, $\Omega_\Lambda = 0.692$ (Planck Collaboration et al., 2016). For the *HST* offsets, we find a range of $\delta R \approx 0.75 - 10.5$ kpc

with the lower and upper bounds set by FRB 20121102A and FRB 20191001A, respectively[4]. Finally, we use the host galaxy half-light radii (r_e), as measured from *HST* imaging (see Section 2.3.1) to determine the host-normalized offsets, $\delta R/r_e$. The values for the projected angular, physical, and host-normalized offsets for the eight FRBs in our sample are listed in Table 2.3.

We supplement the FRB distributions with two FRB host galaxies by Heintz et al. (2020), FRBs 20190611B and 20200430A, both of which have offsets determined from ground-based imaging with seeing of $\sim 0.8''$. To determine the uncertainty on the cumulative distribution, we follow the method of Palmerio et al. (2019) and create 10,000 realizations of asymmetric Gaussian PDFs using the errors on the offset measurements for each FRB, derived from the previously described weighted grid analysis. We then use a bootstrap method to sample from the PDF in each realization, allowing us to compute a CDF of the bootstrapped sample. Finally, we compute the median of all the resulting CDFs, as well as the upper and lower bounds for each bin. We perform this same analysis for the projected physical and host-normalized offset distributions. The resulting median cumulative distributions, and bootstrap estimate of the uncertainty (shown as the shaded gray region) are shown in Figure 2.4.

To compare the FRB distribution to the offset distributions of other transients, we draw relevant comparison samples from the literature. Included are long-duration gamma-ray bursts (LGRBs; Blanchard et al. 2016, short-duration gamma-ray bursts (SGRBs; Fong et al. 2010; Fong and Berger 2013), Ca-rich transients (Lunnan et al., 2017; De et al., 2020), Type Ia supernovae (Type Ia SNe; Uddin et al. 2020), core-collapse SNe (CCSNe; Schulze et al. 2020) and super-luminous SNe (SLSNe; Lunnan et al. 2015; Schulze et al. 2020). To align with the redshift distributions of the FRBs, we only include values for events with $z < 1$. We perform a two-sided KS-test between the median FRB distribution and each of the transient populations

[4]We note that the ground-based determination for FRB 20190611B is the largest physical offset, with ≈ 11.4 kpc.

to test the null hypothesis that the (median) distribution of FRBs and each transient population is drawn from the same underlying distribution. Using this analysis for projected offsets, we find $P_{\rm KS} < 0.05$ for both LGRBs and SLSNe, rejecting the null hypothesis that they are drawn from the same continuous distributions. We caution, however, that we only report KS-test results on the median FRB distribution.

However, for host-normalized offsets, we also find $P_{\rm KS} < 0.05$ for Ca-rich transients and for LGRBs. The remaining p-values are $P_{\rm KS} > 0.05$, and thus we cannot reject the null hypothesis for any other population tested. Finally, we compare the distribution to an exponential disk light profile (light purple curve in Figure 2.4). While the distribution overall appears to be at larger offsets, the $P_{\rm KS} = 0.066$ value is not conclusive. In this analysis, we note that we are treating the FRB population as a single distribution with a dominant progenitor population. The sample size considered here prevents meaningful constraints on the presence of multiple, equally dominant progenitor populations, each of which have distinct offset distributions.

2.2.3 Fractional Flux

We now explore the location of the FRBs with respect to their host galaxy light distributions ("fractional flux"; $\rm F_F$). The brightness of the burst site in relation to how its rest-frame UV and optical host light is distributed is a crucial tool for determining how star formation activity and stellar mass are tracked (Fruchter et al., 2006). Compared to offsets, which can depend on host size and morphology, the fractional flux method is independent of these physical characteristics. Specifically, the measurement determines the fraction of host light fainter than the flux at the burst position, where a value of unity corresponds to the brightest light level of the host ($\rm F_F = 1$).

Foreground stars in the field of FRB 20180916B preclude the direct application of this analysis to the field. Since PSF photometry and subtraction of many of these stars were difficult

as they were saturated; in this case we decided to use an alternate, "brute-force" approach. We first performed an isophote fit to the galaxy using `photutils` (Bradley et al., 2020), clipping pixels which were over the 3σ level compared to the local mean. This left all the foreground stars and subtracted most of the galaxy light. Then we created a segmentation map from the residual image with a threshold level of 4σ over the sky background and minimum source area of 5 pixels (the default value). From the objects extracted, we selected those with a peak pixel value of 1 e^- per sec or greater and created a masked image. This masked out all star light above the segmentation map threshold value. We then replaced the masked pixels with the isophote fit from earlier and used this stitched image for the fractional flux analysis.

We center a 2D cutout on each host galaxy, making sure that we include a sufficient amount of background. We then determine which pixels lie within the 3σ FRB localization ellipse. We note that unlike how we determined the offsets (Section 2.2.2), we do not apply a sub-grid to the localization, as the main limitation is the pixel scale, and we cannot resolve the fractional flux below this scale. The fractional flux for each ith pixel on N pixels within the localization is then calculated as

$$F_F = \frac{\sum_i (F_i < \text{limit})}{\sum_i F_i}. \tag{2.2}$$

We then use a 2-D Gaussian distribution to develop a weighting scheme with each FRB localization ellipse in the same manner as that described in Section 2.2.2. From the distribution of F_F values for each FRB, we determine the median F_F and its standard deviation. The values for the fractional flux for each FRB can be found in Table 2.3.

Figure 2.5 shows the F_F CDF for the sample of eight *HST* hosts from the IR images (corresponding to rest-frame optical; right panel), and four hosts from the UV images (left panel). The gray region was generated in the same manner described in Section 2.2.2. We exclude the

UV imaging of FRBs 20180924B and 20190711A from this analysis because they are effectively non-detections with very large error, while we include the $H\alpha$ imaging for FRB 180916 as a proxy for star formation (Tendulkar et al., 2020). Given that the UV and IR imaging can be used as proxies for star formation and stellar mass, respectively, we keep the two wavelength regimes separated. In this method, the 1:1 dashed line represents a population of events which traces the light of its host galaxy in that band. Adherence to the 1:1 line would indicate that FRBs may trace the distribution of star-forming regions and stellar mass of their galaxies, respectively.

For the IR (rest-frame optical) distribution which can be used as a proxy for stellar mass, the $\mathrm{F_F}$ values span a wide range, $\approx 0.09 - 0.70$, where the lower and upper bounds are set by FRB 20190714A and FRB 20121102A, respectively (Table 2.3). The median of the distribution is 0.33.

Figure 2.5 highlights that the median distribution of FRBs overall traces the fainter rest-frame optical regions of their host galaxies, with a location to the left/above of the 1:1 line. However, the relatively large positional uncertainties which extend to $\sigma_{\mathrm{FRB}} \approx 0.7''$, coupled with the small sample size of eight events leads to a non-trivial uncertainty in the distribution, which is consistent with the 1:1 line. Thus, while FRBs appear to trace the fainter regions of their hosts in terms of stellar mass, at present it is not possible to make a strong statistical statement.

For comparison, we draw $\mathrm{F_F}$ measurements from the literature for SGRBs (Fong et al., 2010; Fong and Berger, 2013), LGRBs (Blanchard et al., 2016), SLSNe (Lunnan et al., 2015), CCSNe (Svensson et al., 2010), and Type Ia SNe (Wang et al., 2013) and divide them into rest-frame UV and optical measurements for direct comparisons. Performing two-sided KS tests with respect to the median FRB distribution, we can rule out the null hypothesis that the LGRBs, SGRBs and FRBs are from the same underlying population as they all yield p-values of $P_{KS} < 0.05$. For CCSNe, Type Ia SNe, and the 1:1 distribution, we find $P_{KS} > 0.05$ and cannot rule out the null hypothesis.

For the UV distribution, which can be used as a proxy for the distribution of current star formation, there are six data points and their median values fall in a fairly narrow range of ≈ 0.29 (for FRB 20191001A) to ≈ 0.67 (for FRB 20121102A). Despite the small sample size, the KS test does reject the null hypothesis that both LGRBs and SLSNe and the median FRB distribution come from the same underlying population with $P_{KS} < 0.05$. However, we caution that the very small sample size coupled with large localization uncertainties (which translate to large measurement uncertainties in $\mathrm{F_F}$) effectively means that almost the entire parameter space of $\mathrm{F_F}$ is included in the uncertainty region. We also note that the IR $\mathrm{F_F}$ contains all three repeating FRBs, whereas the UV $\mathrm{F_F}$ contains two.

2.2.4 Fraction of enclosed light

While the $\mathrm{F_F}$ metric is designed to assess the local environment of the FRB in the galaxy *independent* of its morphology, we introduce an alternative metric to better assess its global position: the fractional flux enclosed

$$\mathrm{F_e} = \frac{\sum\limits_{\mathrm{r_i < r_{FRB}}} \mathrm{F_i}}{\sum\limits_{\mathrm{i}} \mathrm{F_i}} \tag{2.3}$$

with r_i the radius of pixel i and r_{FRB} the distance of the FRB from the galaxy centroid. In practice, we estimate $\mathrm{F_e}$ using the isophotal analysis of Section 2.3.1. Specifically, we find the isophote closest to the FRB localization and measure the flux enclosed within it (and all interior isophotes). Furthermore, we allow for the FRB localization error by performing a weighted average of individual $\mathrm{F_e}$ evaluations across the FRB localization.

Figure 2.6 shows the $\mathrm{F_e}$ results derived from the WFC3/IR images and a 1:1 line corresponding to the null hypothesis that FRBs are biased in tracking the host's light. The close correspondence between the two lends credence to the null hypothesis and the resultant

Table 2.4: Magnitudes are not corrected for Galactic extinction in the direction of the FRB (A_λ). Limits correspond to 5σ confidence.

FRB	Filter	Host Magnitude	A_λ	$\mu_{\rm FRB}$	$\Sigma_{\rm SFR(FRB)}$
		(AB mag)	(mag)	(μJy arcsec^{-2})	($M_\odot\,{\rm yr}^{-1}\,{\rm kpc}^{-2}$)
180924	F300X	23.478 ± 0.058	0.12	< 0.85	< 0.006
190102	F300X	> 27.200	1.40	< 2.58	< 0.016
190608	F300X	19.765 ± 0.014	0.30	1.73 ± 0.033	0.007 ± 0.001
190711	F300X	25.008 ± 0.121	0.88	< 1.61	< 0.016
190714	F300X	23.072 ± 0.053	0.39	< 1.12	< 0.006
191001	F300X	21.228 ± 0.020	0.18	< 0.88	< 0.005

$P_{\rm KS} = 0.73$ value offers statistical support. Similar to Safarzadeh et al. (2020), we infer that FRBs track the general distribution of light and, by inference, stellar mass in their host galaxies.

2.3 Morphological & FRB Site Properties

2.3.1 Galaxy Light Profile Fitting

We fit the light profile for the eight FRB hosts with *HST* data to determine the half-light radii (r_e), which are used to compute the host-normalized offsets. The half-light radii from *HST* imaging are valuable in comparison to previous ground-based imaging, where the measurements are based on seeing-limited images, allowing for more accurate estimates. The increased sensitivity of *HST* also presents the opportunity to search for alternate, fainter host galaxy candidates. Thus, in what follows, we also use light profile fitting to develop a galaxy model, and subtract it from the images to determine constraints on possible alternative, host galaxy candidates (e.g., low-luminosity galaxies or background galaxies) at the position of each FRB.

Table 2.5: Magnitudes are not corrected for Galactic extinction in the direction of the FRB (A_λ). Limits correspond to 5σ confidence.

FRB	Filter	r_e (Isophotal)	r_e (GALFIT)	Host Magnitude	Limit	A_λ	$\mu_{\rm FRB}$	$\Sigma_{M*(FRB)}$
		(kpc)	(kpc)	(AB mag)	(AB mag)	(mag)	(μJy arcsec^{-2})	($10^8\,M_\odot\,{\rm kpc}^{-2}$)
121102	F160W	0.99 ± 0.07	2.05 ± 0.11	23.435 ± 0.055	27.4	0.40	14.57 ± 0.20	0.130 ± 0.002
180916	F110W	2.52 ± 0.15	6.00 ± 0.01	16.178 ± 0.005	25.4	0.88	31.00 ± 0.10	0.115 ± 0.000
180924	F160W	2.54 ± 0.41	2.82 ± 0.53	19.349 ± 0.002	26.2	0.01	20.69 ± 0.10	0.810 ± 0.010
190102	F160W	4.87 ± 0.34	5.00 ± 0.15	20.550 ± 0.006	27.1	0.11	11.10 ± 0.11	0.093 ± 0.002
190608	F160W	2.65 ± 0.53	7.37 ± 0.06	16.693 ± 0.001	25.2	0.02	17.80 ± 0.10	0.340 ± 0.001
190711	F160W	2.88 ± 0.32	2.48 ± 0.13	22.899 ± 0.014	27.6	0.07	6.17 ± 0.11	0.045 ± 0.004
190714	F160W	4.07 ± 0.35	3.85 ± 0.03	18.896 ± 0.002	25.9	0.03	18.00 ± 0.10	1.752 ± 0.018
191001	F160W	6.05 ± 0.66	6.23 ± 0.04	17.135 ± 0.001	24.8	0.01	7.99 ± 0.10	0.322 ± 0.007

First, we use the elliptical isophotal model from `photutils.isophote` to map the light of the eight FRB hosts. We begin with an initial guess, providing values for the central position, ellipticity, semi-major axis, and position angle. The function then fits a series of isophotes which we then use to create a model and residual image. We determine the value of r_e from our isophotal fits, taking this to be the semi-major axis in which half of the total light is enclosed. These values are listed in Tables 2.4-2.5, and are used in our calculation of the host-normalized offsets (see Section 2.2.2).

In addition to the isophotal fits, we also compute residuals from Sérsic profile fits using `GALFIT` v.3 (Peng et al., 2010) for the IR images. Our model has two Sérsic components for all galaxies except the hosts of FRBs 20180924B and 20190711A. These two components roughly correspond to a central bulge and an outer disk. In the case of FRB 20180924B, we use a single Sérsic component because there is no obvious improvement in the residuals relative to performing a multi-component fit. In the case of the host galaxy of FRB 180924, the two components converged to the same effective radii, similar Sérsic indices and similar magnitudes, implying that `GALFIT` could not distinctly identify separate core and disk components. For FRB 190711, the relatively low signal-to-noise of the host galaxy image precludes the identification of two distinct components.

The residual images from the fits are shown in Figure 2.7. The `GALFIT` half-light radii (r_e) reported in Table 2.5 correspond to the larger component (i.e. the disk component) in the case of the two-component fits. While the residual images of FRBs 20121102A, 20190711A and 20190102C do not show clear, symmetric structures, there are such morphological structures in the residual images of the remaining hosts. In particular, spiral arm structure becomes very apparent for FRB 20180924B and 20190714A, as well as the previously-known structure for FRBs 20180916B (Tendulkar et al., 2020), 20190608B (Chittidi et al., 2021) and 191001 (Bhandari et al., 2020a). Therefore we can see in Figure 2.7 that *all* of the FRBs which are localized to

hosts with spiral structure land on or very near to a spiral arm; this point is discussed further in Section 2.4.

2.3.2 Star Formation Rate and Stellar Mass Constraints

In addition to relative photometric measures, these data enable precise photometric measurements at the burst positions. Furthermore, we may convert these light measurements into physical quantities – the star-formation rate (SFR) density $\Sigma_{\rm SFR}$ and stellar mass surface density $\Sigma_{\rm M*}$ - to give additional insight into the local properties of FRB burst sites. It is also informative to compare the local values to the global mean surface densities of their host galaxies, to understand if the locations of FRBs are, for example, elevated or not in terms of these quantities.

To complete the photometric measurements, we create apertures with $r = 3$ pixels at each pixel within the FRB localization. These aperture sums are then weighted by a 2-D Gaussian probability distribution centered on the measured FRB position, the same as that used for the offset and fractional flux determinations in Sections 2.2.2-2.2.3 – with the resolution of the grid being limited by the image pixel scale. We then take the weighted average and divide by the area of the aperture to get an aperture sum per arcsec^2. We compute the magnitude using WFC3 tabulated zeropoints, the corresponding flux in both filters, and the luminosity for the UV band (Table 2.4).

Next, we use the UV luminosity-SFR relation from Kennicutt (1998a) to convert UV measures into star formation rate and subsequently the star formation rate surface density per kpc^2, $\Sigma_{\rm SFR}$ at the burst site in 6 of the HST hosts. For FRB 121102, we use the H-alpha luminosity-SFR relation from Kennicutt (1998b), to obtain a value of 3.99 $M_\odot$ yr^{-1} kpc^{-2}. For the stellar mass surface density per kpc^2, $\Sigma_{\rm M*}$ we compute the ratio of FRB flux to total host flux and adopt the total stellar mass estimates from Heintz et al. (2020) to estimate the local

value. We derive 3σ upper limits on star formation rate densities in the same manner, relevant for hosts that are non-detections or have very low S/N at the FRB site.

In terms of $\Sigma_{\rm SFR}$ Figure 2.8 shows that most FRBs do not obviously occur in elevated regions of star formation with respect to the global values of their host galaxies (albeit most of the UV values are upper limits). The two FRBs with measurements in our sample, FRBs 20121102A and 20190608B lie above the 1:1 line, in concert with previous conclusions (Bassa et al., 2017; Chittidi et al., 2021). We do however find that FRB 191001 lies below this 1:1 line. This burst also has the highest offset and, as is apparent in the UV image, is offset from the UV-bright regions of its host.

For context, Galactic star-forming clouds such as the Lupus and Perseus clouds (Evans et al., 2009) are shown to be well above the 1:1 line in comparison to the Milky Way average as reported by Kennicutt and Evans (2012). The FRB locations, except that of FRB 121102, do not reach these levels of elevated star-formation.

One caveat is that the Galactic star forming clouds and their measurements are derived from pc-scale measurements as opposed to the kpc scales for FRB localizations. Ideally, we would like resolve down to scales that are considered "local" in studies of star formation in the Milky Way. This will require additional $\sim$mas-level localizations and larger aperture space or ground-based observations (e.g. JWST, ALMA).

In terms of stellar mass surface density $\Sigma_{\rm M*}$ Figure 2.8 reinforces several of the conclusions from Heintz et al. (2020). For example, a continuum of characteristics between "repeaters" and "non-repeaters" arises when investigating the stellar mass of the host and the burst site. Like the SFR density, FRBs also do not clearly occur in regions of elevated stellar mass surface densities with respect to the global values of their hosts, and only a few FRBs deviate from the 1:1 relation. We use Milky Way Giant Molecular Clouds (GMCs; Lada and Dame 2020) as a point of comparison to put into context the characteristics of these burst sites

with other sites of star-formation. The stellar mass surface density for these sites relative to their hosts is slightly above, but are not very disparate from that shown for the Galactic GMCs which are $\approx 35\ M_{\odot}$ parsec^{-2} as concluded by Lada and Dame (2020).

2.3.3 Luminosity Constraints on Satellite or Background Galaxies

With the early association of FRB 121102 to a very faint host, the community was led to expect that other FRBs would be found in galaxies of similar type. The subsequent association of FRBs to brighter galaxies (e.g. Bannister et al., 2019) has therefore led some to question whether a fainter, true host galaxy lurks below. To place constraints on an alternate, apparently fainter host galaxy candidate at the FRB position, we use the `GALFIT` residual images (Figure 2.7), in which the elliptical components from the bright, putative host galaxy have been removed to derive point-source limiting magnitudes at the FRB position. We then compute the residual flux value using a circular aperture of $0.5''$ diameter, corresponding to ~ 2.5 times the PSF FWHM. We compute the net standard deviation for all pixels within this aperture. We then take the larger of the flux measurement and five times the net standard deviation as the upper limit on any point source flux that can be detected from the residual images (5σ limit). We find limits of $24.8 - 27.6$ AB mag (see Table 2.5).

We convert each of the at-position limits to an IR luminosity as a function of redshift (Figure 2.9). First, we explore these limits in the context of a spatially coincident satellite galaxy at the same redshift as the putative (brighter) host galaxy (triangles in Figure 2.9). At these redshifts, the limits of $L_{\rm IR} \lesssim (0.5 - 9.2) \times 10^7\ L_{\odot}$, are significantly deeper than the luminosity of any known FRB host, including FRB 121102. This means that despite the presence of morphological features in the `GALFIT` residuals which preclude extremely deep limits, we can still rule out a galaxy with similar luminosity to the host of FRB 121102, which is now considered an outlier in terms of FRB host stellar mass and luminosity (Tendulkar et al., 2017; Li et al.,

2019; Bhandari et al., 2020b; Heintz et al., 2020). Any underlying host would need to have an IR luminosity of $\lesssim 0.02 - 0.31$ times that of the host of FRB 121102 if it was at the same redshift of the brighter host galaxy (Figure 2.9). For reference, we measure IR luminosities for the putative hosts of $\approx 3.0 \times 10^8 - 1.1 \times 10^{11}\ L_\odot$ (set by FRB 20121102A and FRB 20191001A, respectively). It is also worthwhile to explore whether or not a low-luminosity host galaxy of the same luminosity as the host of FRB 20121102A may reside at a *higher* redshift than the apparently brighter galaxy. In this case, we find that the redshift of any background galaxy must be at $z \gtrsim 0.4$ (Figure 2.9). The exception is FRB 20180916B, which still has a meaningful constraint of $z \gtrsim 0.25$. We also calculate the upper limit on the redshift inferred from the Macquart relation for each FRB following the methods of Macquart et al. (2020), and assuming a Milky Way DM = 50 pc cm^{-3} and a host DM = $50/(1 + z_{\rm FRB})$ pc cm^{-3}. This analysis results in limits of $z \lesssim 0.17 - 0.75$ (95% confidence). These redshift limits provide an absolute upper bound on the allowed luminosity of an underlying host of $\approx 4 \times 10^7 - 8 \times 10^8\ L_\odot$. In all cases except for FRBs 20190714A and 20191001A, we can thus rule out an underlying background galaxy of similar luminosity to the host of FRB 20121102A. We note that raising the required luminosity of the host galaxy would only push the required redshift to a higher range. We therefore find that the presence of background galaxies at higher redshifts are not likely for these FRBs given the *HST* limits and constraints from the measured DMs of the FRBs.

2.4 Discussion

Here we discuss the locations, luminosity limits, and morphological features revealed by *HST* imaging in the context of other transient populations with known progenitors, and implications for FRB progenitors.

2.4.1 The Locations of FRBs with Respect to their Host Galaxies

The high angular resolution of the *HST* imaging enables the determination of effective radii and the precise locations for FRB events with respect to their host galaxies using a variety of measures. In general, locations have been used in a variety of transient studies as a major diagnostic to uncovering their progenitors (Prieto et al., 2008; Fong et al., 2010; Fong and Berger, 2013; Blanchard et al., 2016; Lunnan et al., 2017; De et al., 2020; Audcent-Ross et al., 2020; Schulze et al., 2020), as well as the relation to the distribution of young stars (UV, Hα light) and stellar mass (IR light) in their host galaxies. As a means to deciphering the origins of FRBs, we consider comparison data sets from transients which span a wide range of progenitor systems, from those which originate from massive stars in which the populations follow the UV light and exponential disk profiles of their hosts (LGRBs, CCSNe, SLSNe; Fruchter et al. 2006; Lunnan et al. 2015); to those with older stellar progenitors associated with compact objects which are weakly correlated with the UV light of their hosts (SGRBs, Type Ia SNe; Fong and Berger 2013; Wang et al. 2013; Audcent-Ross et al. 2020); to those with unknown progenitors and larger offsets from their hosts (Ca-rich transients[5]).

Comparative studies based on ground-based observations of FRBs have found that the spatial distribution of FRBs are inconsistent with the distribution of LGRBs and SLSNe, both of which originate from stripped-envelope massive stars (Fruchter et al., 2006; Lunnan et al., 2015), but are consistent with other transient types (Bhandari et al., 2020b; Heintz et al., 2020; Bochenek et al., 2020). Our results support these studies, where we find that the locations of FRBs as a population are clearly more extended than LGRBs and SLSNe in terms of physical offsets, with a median of 3.2 kpc (68% interval of [2.0, 8.7] kpc). However, the host galaxies of FRBs are on average larger in physical size (and also stellar mass; c.f., Bhandari et al. 2020b; Heintz et al. 2020) than the hosts of LGRBs and SLSNe (Blanchard et al., 2016; Lunnan et al.,

[5]These are also referred to as Ca-strong transients or CASTs; Shen et al. (2019)

2015), with a range of sizes, $r_e \approx 0.7 - 5.6$ kpc. Due to the larger FRB host galaxy sizes among the transient populations, the differences in offsets becomes less significant when normalized by the size of their host galaxies: the host-normalized offsets of FRBs has a median of 1.4 r_e (68% interval of [0.6, 2.1]r_e), and are only statistically distinct from Ca-rich transients. Finally, FRBs appear to occur at slightly larger host-normalized offsets than expected given an exponential disk profile.

In terms of their host galaxy rest-frame optical and NIR light distributions, the FRBs are on moderately fainter regions of their host galaxies (median F_F=0.33). These distributions serve as proxies for the distribution of stellar mass in their galaxies, and older, moderately massive to low-mass stars, respectively. As a population, FRBs are once again statistically distinct from LGRBs and SLSNe which on average occur on the brighter regions of their host galaxies (Fruchter et al., 2006; Blanchard et al., 2016). The locations of FRBs are also distinct from SGRBs which are very weakly correlated with stellar mass, a consequence of their compact object progenitors which experience kicks and moderate delay times (Fong et al., 2010; Fong and Berger, 2013). Notably, unlike SGRBs, *no* FRBs in our sample occur on the faintest regions of their host galaxies (tempered by the FRB localization errors and the small sample).

The locations of FRBs are consistent with the *radial* distribution of their host rest-frame optical light (fraction of enclosed light), and are indistinguishable from the locations of CCSNe in this regard (c.f., Audcent-Ross et al. 2020). Indeed, the fact that the locations of FRBs trace the 1:1 distribution of the radial distribution of their host light, coupled with the fact that their local stellar mass surface densities are representative of their global host galaxy values, is indicative that their locations are consistent with the stellar mass within their host galaxies. We further find that while two FRBs have elevated local star formation rate densities compared to their global host values, as a population we do not find any clear correlation between FRBs and regions of elevated local star formation rate densities.

In general, the host galaxies of known repeating FRBs tend to have bluer colors, lower stellar masses, and higher star forming rates than those of apparent non-repeating FRBs (Bhandari et al., 2020b; Heintz et al., 2020). This is most saliently highlighted in the star-forming low-mass host galaxy of the repeating FRB 121102 (Chatterjee et al., 2017), which is an outlier in most host galaxy properties. Here, we find that, in terms of the IR distributions, the three known repeaters in this sample (FRBs 20121102A, 20180916B and 20190711A) span the full range of offsets (physical and host-normalized) populated by apparent non-repeaters, as well as fractional flux and enclosed flux. While there do not appear to be any obvious trends in these properties between known repeaters and apparent non-repeaters, we caution that the sample sizes considered here are small.

Overall, the locations of FRBs support the picture that if there is one dominant progenitor population, that they do not originate from massive stars which are stripped of H and/or He (the progenitors of engine-driven SNe such as LGRBs and H-poor SLSNe). We further find that their locations are inconsistent with compact object progenitors which experienced kicks or long delay times transients from significantly older stellar progenitors (SGRBs, Ca-rich transients). However, given the size of the current sample, it is still possible that a fraction of FRBs originate from one of these alternative progenitor channels. These conclusions overall support previous results based on host stellar population properties that LGRB/SLSNe progenitors are not significant contributors (Heintz et al., 2020; Li et al., 2019; Bhandari et al., 2020b; Bochenek et al., 2020). Furthermore, we cannot differentiate the population of FRBs from CCSNe or Type Ia SNe based on their locations, although FRBs do not clearly trace either of these populations in every measured quantity. Therefore, we find it less plausible that the main progenitor channel of FRBs are compact object progenitors such as neutron star mergers or neutron star-black hole mergers, although progenitors which invoke white dwarfs (e.g., accretion-induced collapse of a WD to a NS), which are expected to resemble the properties of Type Ia SNe (Margalit et al.,

2019) could still play a role.

It should be noted, however, that there may be selection effects at play in the observed locations of FRBs. For example, FRBs in dense regions of galaxies such as near the center or inside a spiral arm may be more difficult to detect. As they interact with a denser medium like a star-forming region, the signal is dispersed by the local environment and the DM could exceed the limit of detection (James et al., 2021), i.e. high DM smears the signal leading to a lower S/N. The majority of FRBs presented here were derived from the CRAFT experiment on the ASKAP telescope. That survey has performed searches allowing for bursts with DM$>$ 1000 pc cm^{-3} and have detected several to date (Shannon et al., 2018). Furthermore, the smaller sample of well-localized events, including those presented here, follow the predicted Macquart relation (Macquart et al., 2020). These searches have not detected any bursts with DM greatly in excess of the Macquart relation, and models of the intrinsic host DM distribution indicate a median value of $\approx$ 150 pc cm^{-3} (Macquart et al., 2020; James et al., 2021). Therefore, current expectation is that there is not a large sample bursts with high host-DM missing from the sample. However, this is an important effect to consider given the constraints locations provide for progenitor channels and, analysis of future samples will need to consider further the implications of DM smearing.

It also is possible that scattering will be induced by local material increasing the width of the burst so that it is too faint to be detected or cause it to be falsely rejected by search algorithms. However, the scattering measure is also known to vary considerably, and this variation does not seem to correlate with DM (Qiu et al., 2020). Therefore, we currently consider this a less important bias relative to DM smearing.

2.4.2 The Association of FRB Locations with Spiral Arm Structure

In addition to precise location information, the deep *HST* imaging presented here also enhances low surface brightness features and morphological structure. In particular, previous *HST* studies of two galaxies, those of FRBs 20190608B and 20180916B, demonstrate that they both exhibit complex spiral arm structure (Chittidi et al., 2021; Tendulkar et al., 2020). Spiral structure was also apparent in ground-based imaging for the host galaxy of FRB 20191001A, and supported by extended, continuum radio emission indicative of star formation (Bhandari et al., 2020a). Here, we find an *additional* two FRB hosts with clear spiral arm structure; those of FRBs 20180924B and 20190714A (Figure 2.7), and further uncover a bar feature in the host galaxy of FRB 20180924B. With the exception of FRB 20180916B, all FRB spiral-arm hosts are associated with apparent non-repeaters. The two remaining known repeaters in the sample are FRBs 20121102A and 20190711A; the former originates from a low-luminosity host, while the latter originates in a host at the high redshift end of our sample. Thus we do not consider the non-detection of spiral features from these hosts to be constraining or informative.

Overall the prevalence of clear spiral structure (5/8, or $\approx$ 60% in our sample) is consistent with the observed galaxy population (Willett et al., 2013). Furthermore, despite the larger offsets of FRBs, we find that the locations of *all* well-localized FRBs with hosts that exhibit spiral structure are consistent with major spiral arm features. It is important to note that the IR light profile is dominated by red supergiants, AGB stars, and low-mass stars, as opposed to young, massive O- and B-stars seen in Hα and UV imaging. In particular, in accordance with the density wave theory of spiral structure, the IR spiral arms generally spatially lag the Hα light (Pour-Imani et al., 2016), although significant enhancement in star formation in the vicinity of the IR spiral arms is expected (Seigar and James, 2002). The signal-to-noise of the FRB UV images prevent such a constraint for FRB hosts.

The locations of transients with respect to spiral arm features, as well as offsets from regions of peak brightness within the spiral arms, can serve as a major clue for their progenitors. In particular, the offset from bright peaks serves as a proxy of the spatial drift from birth to explosion site, and can set a timescale for the lifetime of the progenitor. Indeed, SNe exhibit distributions of offsets from the peak of their spiral arms in accordance with their progenitor age, with stripped-envelope SNe (Type Ib/c) having smaller offsets from the peak than Type II or Type Ia SNe (Aramyan et al., 2016). If all FRBs originated from young magnetars, it is expected that their positions would generally correlate with the UV spiral arms of their hosts, and at small offsets from star-forming features (c.f., the distribution of Galactic magnetars; Olausen and Kaspi 2014). However, we find that while the FRB positions are consistent with spiral features, they are not on the brightest part of the spiral arms. Indeed, UV and Hα studies of the known repeating FRBs 20121102A and 20180916B found clear offsets from the closest star-forming features of ≈ 250 pc (Bassa et al., 2017; Tendulkar et al., 2020). This is also in agreement with the results by Chittidi et al. (2021), who found from detailed analysis of the UV imaging of FRB 190608 that the FRB did not prefer the most active star-forming region in the galaxy.

Taken together, this supports a picture that FRBs do not originate from the youngest, most massive stars, in concert with previous, comparative results with other transients (Li et al., 2019; Heintz et al., 2020; Bhandari et al., 2020b). We also find that FRBs do not appear to reside in the inner bulges of their host galaxies, which are generally dominated by older, higher-metallicity stars in comparison to the spiral arms (Peletier and Balcells, 1996). It is further worth noting that the main selection effect at play in FRB discovery is the difficulty of detecting highly-scattered FRB signals, where the signal is temporally broadened by multipath propagation in a dense, turbulent medium. Since such sites are preferentially associated with star formation, one might naively expect there to be additional observational challenges in detecting FRBs in spiral arms where the chance of the FRB sightline intersecting an enhanced

region of turbulence is higher. However, the precise effects of discovering FRBs with respect to morphological structure is not well-quantified.

2.4.3 Luminosity Limits on Alternative Host Candidates

Finally, we remark on the presence of fainter, alternative host galaxy candidates at the positions of the FRBs. This question is in part motivated by the low-luminosity host galaxy of FRB 20121102A (Tendulkar et al., 2017), which, coupled with the remaining FRB hosts suggests a broad host galaxy luminosity function spanning the full range of galaxies (Heintz et al., 2020). Here we have explored the presence of both satellite galaxies at the same redshift as the putative host, and background galaxies at higher redshifts. The relatively low redshift range of the population examined here, $0.03 \lesssim z \lesssim 0.522$, enables deep constraints even in the presence of strong morphological features. In both scenarios, we find it unlikely that the FRBs originated from an underlying galaxy. The exceptions are FRBs 20190714A and 20191001A: in the former case, a galaxy of equal luminosity to FRB 20121102A would approach the redshift limit, while in the latter case, the high DM allows a host with ≈ 8 times the luminosity of FRB 20121102A, albeit still on the faint-end slope of the galaxy luminosity function ($\approx 8 \times 10^8\ L_\odot$).

2.5 Summary & Conclusions

In this paper we used high-resolution *HST* imaging to perform a detailed study on the locations of 8 FRBs and their environments, 6 of which are newly presented here. We used these data to place constraints on the spatial distributions (physical and host-normalized), in support of previous works based on ground-based imaging. We find a median host-normalized offset of 1.4 ($[0.6, 2.1]r_e$; 68% interval), and overall a distribution that lies between the more centrally concentrated LGRBs and SLSNe, and the extended SGRBs and Ca-rich transients. We also

determine the distribution of FRBs with respect to their IR (rest-frame optical) host galaxy light (fractional flux, and radial distribution), showing that FRBs are consistent with tracing the stellar mass distribution of their host galaxies.

The sensitivity of *HST* additionally enables constraints on possible alternative host galaxy candidates; we find it improbable that there exists a satellite or background galaxy at the FRB locations, strengthening the associations with the brighter, putative hosts identified in ground-based imaging for this sample. We explore the FRB site properties in terms of star formation rate (near-UV) and stellar mass (IR) surface densities, finding that the locations are not particularly enhanced in either property compared to the global values of their hosts (although few measurements exist for the star formation rate densities). Finally, we find that 5/8 FRB host galaxies in the sample have spiral arm features, and that these FRBs are consistent with the locations of those spiral arms (albeit inconsistent with locations on the *brightest* peaks of these spiral arms). If there is a dominant progenitor population among this tested distribution, we thus do not find strong support for a connection to the most massive (stripped-envelope) stars, or events which require kicks and long delay times.

The promise of sub-arcsecond localized FRBs in solving the progenitor question is being realized, in part, with the first population studies of their local and host galaxy environments. Such precisely-localized FRBs are and will continue to be detected at growing rates. As the number of secure associations continues to increase, we will be able to make significant progress toward understanding their progenitors, as well as connecting the properties of FRBs to those of their host galaxies. The current sample of well-localized FRBs is admittedly small, much less those with high-resolution imaging. Moreover, the current sample with secure host galaxies is subject to various selection biases which have been mentioned throughout this paper.

Looking toward the future, upcoming FRB experiments and upgrades to existing ones will deliver larger, more uniform samples of sub-arcsecond localized FRBs, which importantly

will push beyond the current DM or redshift horizons. Equipped with a large sample of FRBs with high-resolution imaging, we will be able to identify trends between the locations of FRBs in known repeaters and apparent non-repeaters, in host galaxies of different morphological types (e.g., prevalence of spiral sub-structure, star-forming vs. quiescent), and make more statistically significant statements about their similarities or differences to other transient populations. Matched to the increased sensitivities of discovery experiments, we will also explore evolution of the local properties of FRBs with redshift. All of these studies will provide important clues to their origins. Larger samples will also enable tighter constraints to be placed on local contributions to the dispersion measure in DM and IGM studies, optimizing the use of FRBs as a cosmological probe. Finally, *HST* and soon *JWST* will also aid in our understanding of whether FRBs originate from a single, dominant progenitor channel or multiple contributing channels, a central question in FRBs.

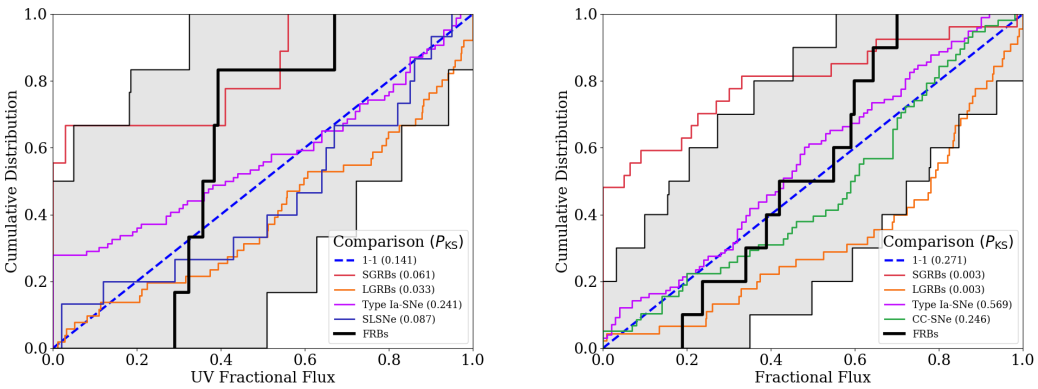

Figure 2.5: *Left:* Cumulative distribution of UV fractional flux (F_F) of the 6 FRB hosts in the *HST* sample with WFC3/UVIS imaging. The gray shaded region is a bootstrap estimate of the RMS of the distribution, which accounts for both uncertainties on individual measurements, as well as statistical uncertainties due to the sample size. For comparison, the corresponding distributions for SGRBs (Fong et al., 2010; Fong and Berger, 2013), LGRBs (Blanchard et al., 2016), Type Ia-SNe (Wang et al., 2013), CCSNe (Svensson et al., 2010), and SLSNe (Lunnan et al., 2015) are shown. Also shown is the dashed, 1:1 line, representing the distribution of host galaxy light. The p-values from two-sided KS tests between each population and the median FRB distribution are listed. *Right:* The same as the left-hand panel but for all eight FRB hosts with *HST*/IR imaging.

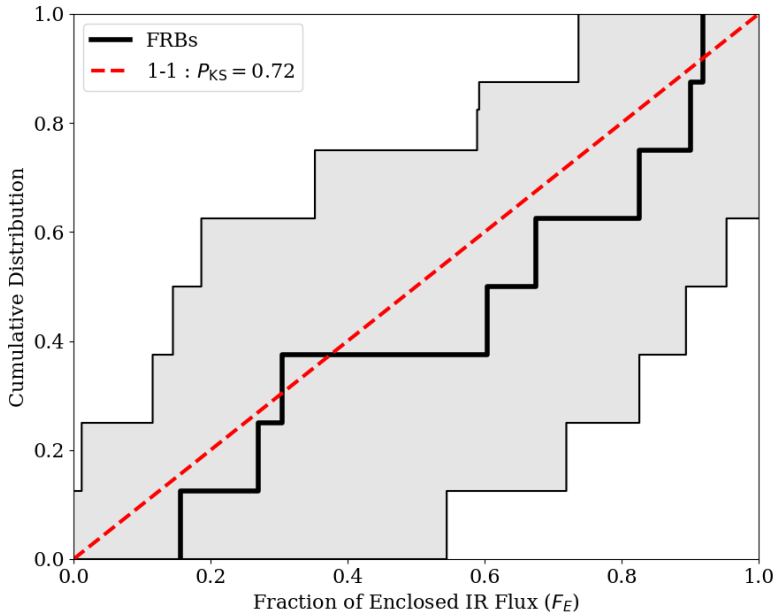

Figure 2.6: The median FRB cumulative distribution of enclosed flux (black line), which is the fraction of host light enclosed within a radius set by the position of the FRB. The values are derived for eight host galaxies with IR images. The gray shaded region represents the 1σ uncertainty in the CDF, while the blue dashed line indicates a 1:1 mapping. A KS test between the median distribution and 1:1 line does not reject the null hypothesis that the distributions are drawn from the same underlying population.

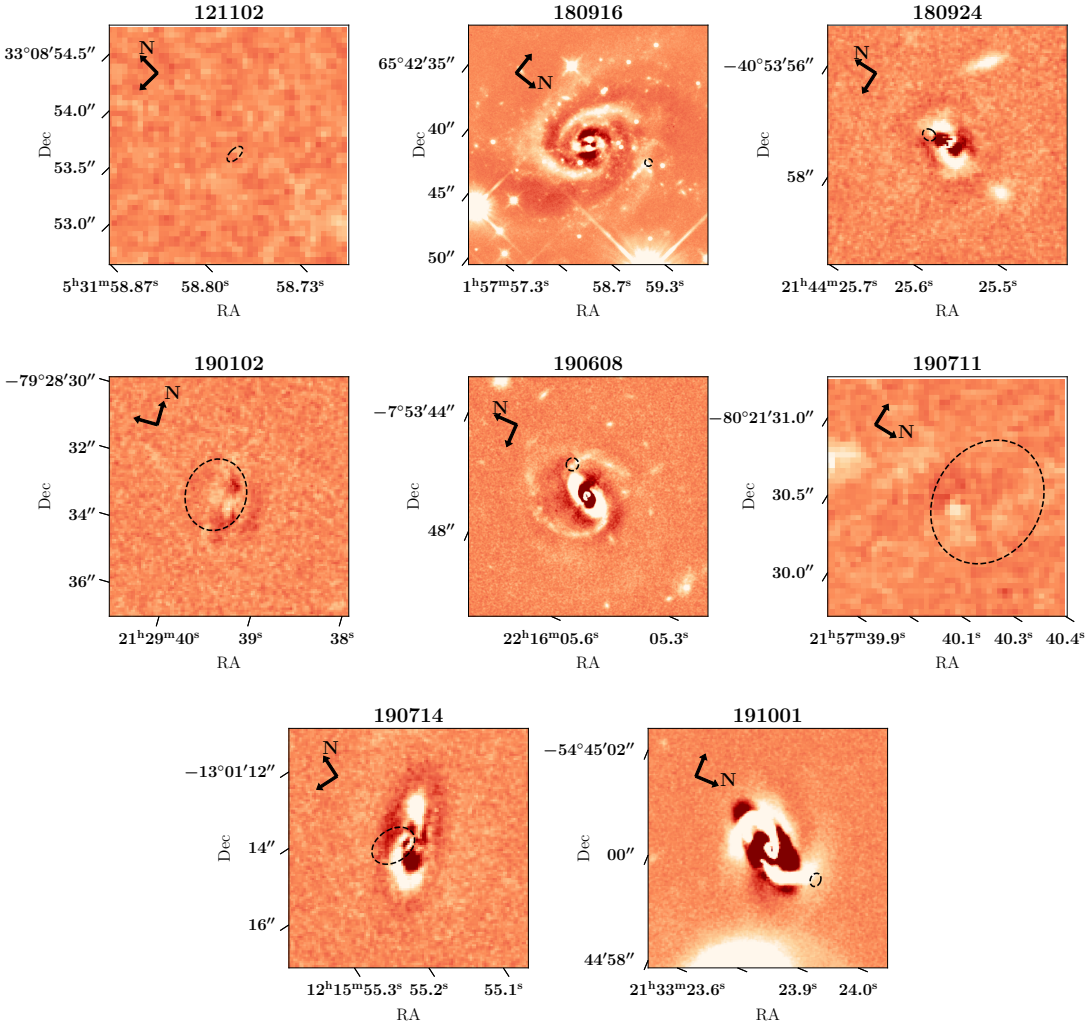

Figure 2.7: Residual images produced by `GALFIT` from the F160W host galaxy image set (and FRB 20180916B for F110W). The North and East directions are indicated by the black arrows at the top left. The light distribution for all galaxies was modeled as a sum of two Sérsic profiles corresponding to a central core and an outer disk, except in the host galaxies of FRBs 180924 and 190711. In those two galaxies, a single Sérsic profile fit was used because a two component fit did not produce a significant improvement in the visual quality of the residuals. It is interesting to note that five of the eight FRB locations, marked by the dashed 2σ localization ellipses (200σ for 180916 and 30σ for 121102), are coincident with spiral structures in their respective hosts.

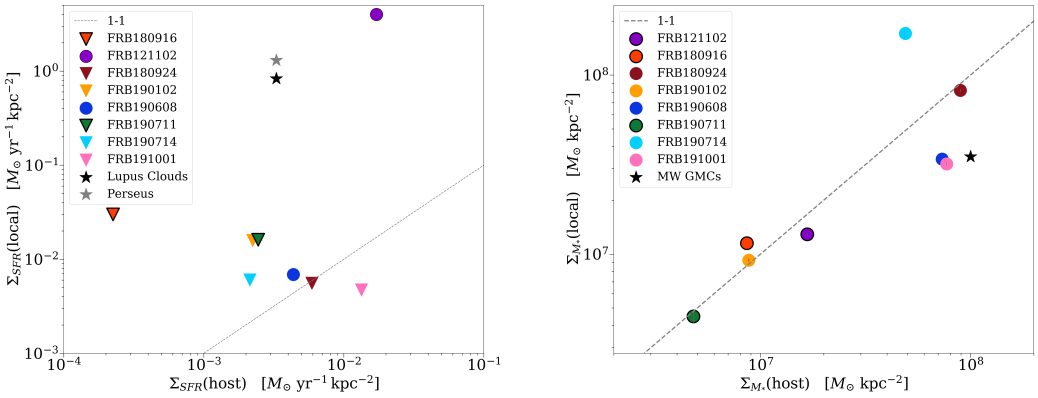

Figure 2.8: Comparisons of local FRB properties to global host properties. The points with black outlines are "repeaters". The triangles denote 3σ upper limits on the SFR. *Left:* Star formation rate surface density at FRB location versus star formation rate surface density of the host. Compared to the 1:1 line, the sites of FRBs are not clearly elevated in star formation rate surface densities with respect to their hosts, and do not reach the surface densities of Galactic star-forming regions (Evans et al., 2009). *Right:* Average stellar mass surface density at the burst site versus average stellar mass surface density of the host. Most FRB locations track the 1:1 line, with a few deviating from this relation. The average value for Milky Way GMCs is marked shown as the black star (Lada and Dame, 2020).

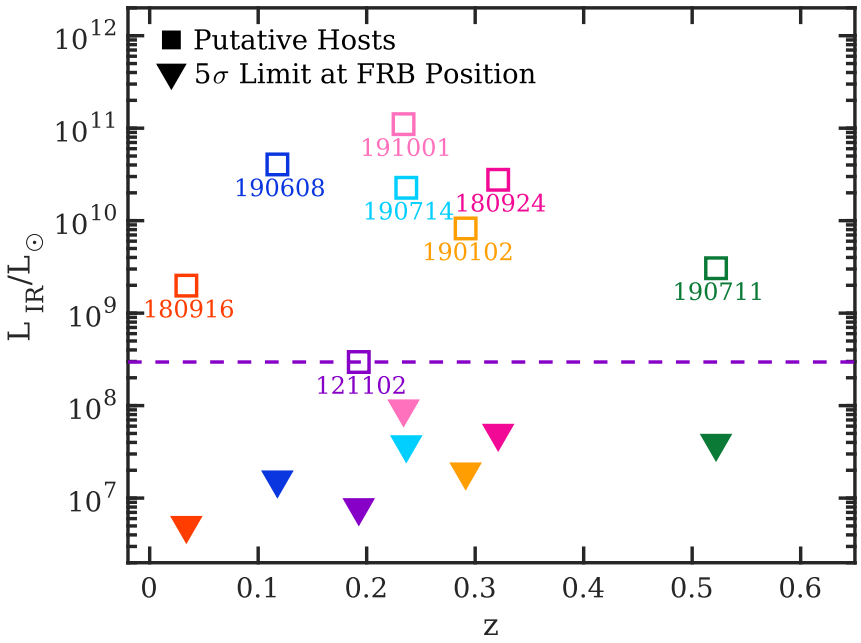

Figure 2.9: Limits on the near-IR luminosity at the FRB positions (lines) as a function of redshift, derived from `GALFIT` residual images after a Sérsic component is removed. Filled triangles represent 5σ limits at the redshift of the putative, brighter FRB host galaxy. The limits rule out satellite galaxies at the FRB positions at the same redshift as the bright host to deep limits. If instead a background galaxy exists with a host luminosity similar to FRB 121102, this would require redshifts larger than allowed by the measured DM (diamonds, 95% confidence) in all cases except FRB 190714 and 191001.

Chapter 3

Imaging FRB Hosts from the Ground with Adaptive Optics

3.1 Introduction

Fast Radio Bursts (FRBs) are luminous millisecond-duration bursts of radio waves that originate from extragalactic sources. FRBs were first discovered in 2007 (Lorimer et al., 2007), but it was not until 2017 that the first FRB — FRB 20121102A — was precisely localized and associated with a host galaxy at $z = 0.19$, providing the first direct evidence of their cosmological origins (Chatterjee et al., 2017; Marcote et al., 2017; Tendulkar et al., 2017). However, despite the continued FRB detections, and subsequent host galaxy studies (e.g. Tendulkar et al., 2017; Heintz et al., 2020; Chittidi et al., 2021; The CHIME/FRB Collaboration et al., 2021; Kirsten et al., 2022; Bhandari et al., 2023; Ryder et al., 2023; Law et al., 2023), the sources of FRBs remain largely a mystery.

While some FRBs are known to repeatedly burst, most FRBs are only associated with a single burst and are considered apparent non-repeaters (e.g. The CHIME/FRB Collaboration

et al., 2021). Repetition aids in localization, as demonstrated by the fact that all of the first precisely localized FRBs were repeaters until the Commensal Real-time ASKAP Fast Transient (CRAFT) survey (e.g. Bannister et al., 2017; Marcote et al., 2017, 2020; Tendulkar et al., 2020; Bhandari et al., 2020b). However, with advances in FRB searches more broadly, the capability to localize apparent non-repeaters to sub-arcsecond scales is sharply increasing. A greater number of FRBs are now being detected with sub-arcsecond and even milli-arcsecond localizations by fast transient searches using radio interferometers (Driessen et al., 2023; Law et al., 2023). A high volume of well-localized FRB detections (multiple per day) from the CHIME Outriggers, CRACO on ASKAP (successor to CRAFT), and DSA-110 looms on the horizon (Kocz et al., 2019; Leung et al., 2021).

Though an FRB-like burst was localized to a Galactic magnetar (Bochenek et al., 2020; CHIME/FRB Collaboration et al., 2020, SGR 1935 + 2154;) a great diversity of host galaxy characteristics and FRB locations could support the efficacy of multiple progenitor pathways. FRBs have been localized to a globular cluster (Bhardwaj et al., 2021; Kirsten et al., 2022), star-forming dwarf-galaxies (Marcote et al., 2017; Bhandari et al., 2023), and massive spiral galaxies with varying offsets and associations to underlying morphological structure (e.g. Chittidi et al., 2021; Marcote et al., 2020; Mannings et al., 2021; Dong et al., 2023). The repeating bursts FRBs 20121102A and 20190520B have also been associated with compact, persistent radio sources Marcote et al. (2017); Niu et al. (2022). Thus, more well-localized FRB detections and host observations are necessary to create a larger sample from which we can derive meaningful statistics and continue making robust associations.

Local environment studies, in conjunction with the characterization of global host properties and constraints on multi-wavelength or persistent counterparts, have been transformative in our understanding of the origins of other transients such as short- and long-duration gamma-ray bursts (e.g. Fruchter et al., 2006; Fong et al., 2010; Fong and Berger, 2013; Zhang et al., 2018)

and various types of supernovae (e.g. Kuncarayakti et al., 2018; Hsu et al., 2023). In this study, we utilize adaptive optics (AO) imaging from the Gemini South Telescope to study the local environments of five FRBs along with their global host properties to help better understand FRBs and their origins.

Improvements in FRB detection rates and localization precision will have — and are already having — important implications for progenitor studies. A key to understanding FRB sources lies in our ability to characterize the local environments of these bursts. This, in combination with analysis of burst properties and propagation effects such dispersion measures, time-variability of rotation measures, and scattering can provide key insights to FRB production mechanisms and sources. Many such local environment studies have relied on space-based observations to achieve depth and resolution that reaches sub-arcsecond scales (Mannings et al., 2021, etc.). Unfortunately, as the sample of FRBs grows, it may not be feasible to follow up each event with space-based resources. Therefore, we find it necessary to develop a ground-based follow-up approach that utilizes adaptive optics as an alternative for accommodating high-spatial-resolution for high-volume follow-up efforts. While it is true that more information about burst properties can provide much-needed information, we use this paper to focus on the investigation of the efficacy of ground-based AO observations in relation to follow-up work. Future papers will explore these details, possible correlations, and therefore physical explanations of observed effects.

This paper is organized as follows: in §3.2 we describe the sample selection and observations. In §3.3, we present our analysis and results on the brightness of the host galaxy at the FRB location in comparison with the rest of the galaxy. In §3.4, we discuss the FRB physical locations and offsets relative to the structure of their host galaxies. We discuss these results in §3.5 and conclude in §3.6. Throughout the paper, we employ a Planck cosmology with $H_0 = 67.8$ km s^{-1} Mpc^{-1}, $\Omega_M = 0.308$, and $\Omega_\Lambda = 0.692$ (Planck Collaboration et al., 2016).

However, it can be noted that changes in these values do not significantly affect the results.

3.2 FRB Data and Sample Selection

3.2.1 Sample of FRB Host Galaxies

Here we present observations of seven FRB host galaxies obtained with the Gemini South Adaptive Optics Imager (GSAOI) and the Gemini Multi-conjugate adaptive optics System (GeMS) on Gemini South. The data for these FRB host galaxies were collected between July 2021 and April 2022 as part of the programs GS-2021A-C-2, GS-2021B-C-3, and GS-2022A-C-2.

All of the host galaxies in our sample have spectroscopically confirmed redshifts (Heintz et al., 2020; Bhandari et al., 2020b, 2023; Glowacki et al., 2023) and their FRBs were discovered with the Australian Square Kilometre Array Pathfinder (ASKAP) telescope through the CRAFT survey. These are considered secure associations with PATH (Aggarwal et al., 2021) posterior probabilities of $P(O|x) \geq 0.93$. None of the FRB samples in this sample have yet been observed to repeat. Many of these FRBs have been presented in previous works (e.g. Prochaska et al., 2019c; Heintz et al., 2020; Mannings et al., 2021; Bhandari et al., 2023; Glowacki et al., 2023), but the hosts of FRBs 20210807D and 20211212A are newly presented here. In a companion paper, we describe imaging of the hosts of FRBs 20210807D, and 20211212A, including the FRB localization, using the Very Large Telescope (VLT) (Deller et al., in prep). To be included in this sample, the hosts also had to be in a field that satisfied the guide star requirements outlined in §3.2.2.

3.2.2 Host Observations

Laser guide star adaptive optics-assisted near-IR observations of the FRB host galaxies were obtained with GeMS/GSAOI on the 8.1-m Gemini South telescope. GSAOI is fed by GeMS

and covers an $85'' \times 85''$ field-of-view (FoV) with a pixel scale of $0.0197''$ pixel^{-1}, delivering close to diffraction-limited images between 0.9 and 2.4 μm. Uniform AO correction across the full GeMS FoV requires up to three natural guide stars (NGS) in addition to the five-point sodium laser guide star (LGS) pattern. However partial AO correction is still possible with two (or even one) NGS of sufficient brightness ($m_R < 15.5$ mag) within the $1''$ patrol field of the wavefront sensor probes, as well as one on-detector guide window star ($m_H < 13.5$ mag) within the $40''$ FoV of any of the four GSAOI detectors at all dither positions.

Each target was imaged in the K_s filter [1962.58-2335.92 nm][1] using a nine-step dither pattern, with 2 co-adds of 60 sec at each position and a step size large enough ($5''$) to cover the gaps between the detectors. The targets were positioned within one of GSAOI's four detectors, with the array orientation set by the locations of the NGS. Including overheads and interruptions due to aircraft and satellite avoidance, a complete observation required 1–1.5 hours. These observations are summarized in Table 5.1.

For FRB 20210117A, the host was not detected with GeMS/GSAOI at the FRB coordinates and only 5/9 dithers were completed. This host is a faint dwarf galaxy as discussed by Bhandari et al. (2023); as is consistent with our non-detection.

3.2.3 Image Processing

The data were retrieved from the Gemini Observatory Archive (GOA) at NSF's NOIRLab. The data were reduced using the Gemini DRAGONS (Data Reduction for Astronomy from Gemini Observatory North and South; Labrie et al. (2019)) package version 3.1.

The dark current is very low for GSAOI (~ 0.01 e-/s/pix), thus dark subtraction was not necessary. A master-flatfield was created from a series of lamp-on and lamp-off exposures. A stack was made for each, and the lamp-off stack was then subtracted from the lamp-on stack.

[1] https://www.gemini.edu/instrumentation/gsaoi/components

Table 3.1: RA_{Host} and Dec_{Host} are the host coordinates in the GeMS/GSAOI image WCS. σ_{Host} was calculated by summing the RA and Dec errors in quadrature. For 20181112A σ_{Host} represents the uncertainty in the host position due to astrometric corrections. For 20210117A no host was detected and the astrometry of the image was not corrected, thus we do not have a value for σ_{Host}. NGS is the number of natural guide stars used during observation. Date refers to the date of observation.

FRB	RA_{Host}	Dec_{Host}	σ_{Host}	z	PA	$M_\star$	NGS	Exposure Time
	(J2000)	(J2000)	(arcsec)		($10^9 M_\odot$)		(UT)	(s)
20180924B	21h44m25.2s	−40d54m00.9s	0.13	0.321	24.5	3	2021 Aug 1	540
20181112A	21h49m23.7s	−52d58m15.3s	0.13	0.475	7.4	1	2021 Aug 2	480
20191001A	21h33m24.4s	−54d44m54.3s	0.29	0.234	53.7	2	2021 Aug 1	1860
20210117A	22h39m55.1s	−16d09m05.4s	-	0.214	0.4	1	2021 Aug 2	240
20210807D	19h56m52.8s	−00d45m44.5s	1.03	0.129	93.3	3	2021 Sep 13	1020
20211127I	13h19m13.9s	−18d50m16.1s	0.28	0.047	24.5	3	2022 Apr 15	2040
20211212A	10h29m24.2s	+01d21m39.0s	0.71	0.071	19.0	1	2022 Apr 15	1140

This result was normalized. The static bad pixel masks (BPMs) were fetched from the GOA. The science files were then flatfield-corrected, aligned, and stacked. The final reduced images are shown in Figure 3.1.

3.2.4 Astrometry and Uncertainties

We performed absolute astrometry using the Gaia DR2 and Gaia DR3 catalogs. To do this, we utilized PHOTUTILS.SEGMENTATION to create a segmentation map of each respective image. We then cross-matched these x and y centroids with the Gaia sources within 3 arcseconds of these coordinates. For the cases where the WCS information of the image is offset by more than 3 arcseconds, a manual correction was done by cross-matching the x and y centroid values with the determined Gaia sources based upon a visual (by-eye) association. A new WCS header was then created with this information. We calculated the RMS uncertainty of the astrometry of the images as $\sigma_{\rm ast}$.

Due to lack of Gaia sources in the fields for FRBs 20181112A and 20211212A, the process above was followed but using the Dark Energy Survey (DES) (Abbott et al., 2021) and Panoramic Survey Telescope and Rapid Response System (Pan-STARRS) (Chambers et al., 2016; Flewelling et al., 2020) respectively, as reference catalogs from which to extract stellar positions.

We then used GALIGHT (Ding et al., 2021) to determine the host galaxy centroid positions and their associated uncertainties ($\sigma_{\rm host}$). Inputs for GALIGHT included the radius for cutout around the galaxy and guesses for the galaxy centroid position and position angle. The positions and $\sigma_{\rm host}$ values are listed in Table 3.1.

Since we analyze the host brightness at the FRB location, the associated localization uncertainty ($\sigma_{\rm FRB}$) is also incorporated into our calculations. The statistical and systematic uncertainties from the FRB localizations are included in $\sigma_{\rm FRB}$ (Table 3.2).

3.3 Light at FRB Locations

Placing transients in relation to the distribution of various wavelengths of light (related to ionized gas, neutral gas, stellar components, etc.) in their hosts can be an important piece of evidence for tying them to a source or progenitor event (Fruchter et al., 2006; Fong et al., 2010; Fong and Berger, 2013). In the infrared, we are most sensitive to the distribution of the older (more numerous) stellar populations. Here we complete morphological studies of each host and study the light at the location of the burst. In combination with one another, these analyses provide information on the local environment of the burst and therefore likely sources. For FRB 20191001A it was found that the coordinates published previously in other works were offset in the incorrect direction in declination (see Bhandari et al. (2020a)). The coordinates presented in this paper are the updated coordinates.

3.3.1 Galaxy Light Profile Fitting

We use GALIGHT (Ding et al., 2021) to fit the light profile for five of the FRB hosts, to determine the half-light radii (r_e) and study low-surface brightness structures and host morphologies. Owing to the faintness of the hosts for FRBs 20181112A and 20210117A, we were unsuccessful at creating a segmentation image with GALIGHT and could not complete related analyses. These analyses are also limited by the relatively poor localization precision of FRB 20181112A, where any relationship to the underlying sub-structure would be difficult to determine and, therefore, interpret.

Using GALIGHT, we first created a cutout around the host galaxy and masked any unwanted sources. We then defined the coordinates of at least four stars in the original image and created PSF models to choose from and utilize. We used the GALIGHT model to compute residuals from Sérsic profile fits, where the Sérsic index n defines the steepness of the radial

Table 3.2: a refers to the angular size of the semi-major axis describing the 1σ statistical ($a_{\rm stat}$) and systematic ($a_{\rm sys}$) uncertainties added in quadrature. The same applies to b, the semi-minor axis. PA refers to the position angle of the error ellipse on the sky. Data from Heintz et al. (2020), Bhandari et al. (2020b), Gordon et al. (2023), Deller et al., in prep, and Glowacki et al. (2023). For FRB 20191001A it was found that the coordinates published previously in other works were offset in the incorrect direction in declination (see Bhandari et al. (2020a)). The coordinates presented here are the updated coordinates.

FRB	$\rm RA_{FRB}$	$\rm Dec_{FRB}$	a	b	PA
	(J2000)	(J2000)	(arcsec)	(arcsec)	(degrees)
20180924B	21h44m25.25s	−40d54m00.10s	0.18	0.18	0
20181112A	21h49m23.62s	−52d58m15.39s	5.75	1.44	120
20191001A	21h33m24.42s	−54d44m53.58s	0.27	0.19	79
20210117A	22h39m55.01s	−16d09m05.45s	0.13	0.12	90
20210807D	19h56m53.14s	−00d45m44.49s	0.40	0.40	0
20211127I	13h19m14.08s	−18d50m16.69s	0.80	0.20	0
20211212A	10h29m24.16s	+01d21m37.67s	0.80	0.60	0

surface brightness profile. A larger n value indicates a steeper inner profile and an extended outer wing. The hosts of FRB 20180924B, FRB 20211127I, and FRB 20211212A were fit using two Sérsic components, equating to a disc and a bulge. FRBs 20191001A and 20210807D were fit utilizing three Sérsic components.

The GALIGHT half-light radii r_e are presented in Table 3.3. The values correspond to the effective radius of the disk component of the fit produced by GALIGHT. The $r_{\rm e}$ values range from $0.43''$ to $2.80''$. We then converted these angular offsets to physical offsets using the host redshifts and Planck 15 cosmology as detailed in §3.1. The physical effective radii range from 2.07 to 6.67 kpc, those values belonging to the host galaxies for FRB 20180924B and FRB 20191001A, respectively. Inclination is accounted for.

The residual images from the GALIGHT fits are shown in Figure 3.2. After removing the smooth light of the galaxies from the GALIGHT Sèrsic models, the spiral structure is quite apparent for four out of five hosts, with hints of spiral structure for the host of FRB 20180924B. This host provides a test case for comparisons between space- and ground-based imaging. Though the Hubble Space Telescope (HST) image (and associated residual) presented by Mannings et al. (2021) showed more extended, spiral structure, GeMS+GSAOI does somewhat recover the structure in this host as evidenced by Figure 3.2. The spiral structure for FRB 20211212A is newly presented here with further discussion in Deller et al. (in prep). The spiral structure for FRB 20180924B was previously known (Mannings et al., 2021), as well as the structures for FRB 20191001A (Bhandari et al., 2020a), FRB 20210807D, and FRB 20211127I (Glowacki et al., 2023).

While the spiral structure is already apparent in Figure 3.1, the arms are more defined in the residual images and thus better for the spiral arm offset analysis described in §**??**. For each host, the FRB occurs either on or close to a spiral arm of the galaxy. The host of FRB 20211127I is now one of only four reported FRBs with a clear bar structure observed in the host galaxy (along with the hosts of FRB 20190608B, FRB 20201124A and FRB 20220319D; Chittidi et al., 2021; Xu et al., 2022; **?**).

3.3.2 Stellar Mass Surface Density

Due to the high precision sub-arcsecond localizations of the FRBs in this sample as matched by the image resolution, photometric measurements could be made at the immediate burst position. The following photometric analysis was modeled after that performed by Mannings et al. (2021) on *HST* imaging in service of better understanding the local environment properties, and how they compare to global host properties.

We measured the stellar mass surface density (Σ_{M*}) at the location of the FRB by

Table 3.3: FRB 20181112A and FRB 20210117A are not included in these calculations due to the large FRB positional uncertainty relative to the size of the host and the detection not being significant enough for the host to be identified by GALIGHT (see §3.3.1). Limiting Magnitudes correspond to 5σ detection thresholds.

FRB	r_e	r_e	i	Host Magnitude	Limiting Magnitude	Σ_{M*}
	(arcsec)	(kpc)	(degrees)	(AB mag)	(AB mag)	($10^8 M_\odot kpc^{-2}$)
20180924B	0.43 ± 0.01	2.07 ± 0.03	51	18.841 ± 0.006	28.0	1.832 ± 0.001
20191001A	1.74 ± 0.01	6.67 ± 0.04	59	15.883 ± 0.003	26.4	3.278 ± 0.001
20210807D	2.76 ± 0.01	6.56 ± 0.04	60	16.729 ± 0.003	27.1	1.695 ± 0.001
20211127I	2.80 ± 0.01	2.67 ± 0.01	33	16.059 ± 0.002	28.0	4.612 ± 0.004
20211212A	2.36 ± 0.01	3.29 ± 0.01	40	15.790 ± 0.002	25.8	2.461 ± 0.001

determining the IR surface brightness within the FRB localization region. We account for the uncertainty in the FRB localization in our estimate. We do so by computing a weighted average where the relative weights are given by a 2D Gaussian probability distribution function (PDF) along the axes of the localization uncertainty. We create circular apertures with a radius of 3 pixels, equating to the size of the PSF, at each pixel within the FRB localization. These aperture sums are then weighted accordingly, with the resolution of the Gaussian grid and binning being limited by the image pixel scale. We then divide this weighted average by the area of the aperture to get an aperture sum per square arcsecond, or surface brightness.

We separately determine the magnitude of the host galaxies using the GSAOI zero-point and the corresponding flux. The magnitude of each host galaxy is presented in Table 3.3. We then calculate the ratio between the flux at the FRB site to the flux of the entire galaxy and adopt the total stellar mass estimates from Heintz et al. (2020) and Bhandari et al. (2020b) to estimate the host $\Sigma_{\rm M*}$ (Table 3.3). The relationship between the local stellar mass surface density at the FRB location and the average stellar mass surface density of the entire galaxy is shown in Figure 3.3.

Figure 3.3 reveals that the stellar mass surface densities $\Sigma_{M_\star}$ at the FRB locations are elevated compared to the global stellar mass surface densities of their host galaxies for 4/5 hosts. The other host (FRB 20180924B) has a stellar mass surface density lower at the FRB location in comparison to the galaxy as a whole, however this value is fairly close to the 1:1 line. Error bars for each of the points are significantly smaller than the marker size. We use Milky Way giant molecular clouds (GMCs; Lada and Dame 2020) as a means of comparing the locations of FRBs to sites of active star formation within the Milky Way. The stellar mass surface density at the FRB positions relative to their hosts is three times or more than that shown for the Galactic GMCs, which is $\approx 35 \times 10^6\ M_\odot\,{\rm kpc}^{-2}$ according to Lada and Dame (2020).

3.3.3 Luminosity Constraints on Background Galaxies

With hosts such as those of FRBs 20121102A (Tendulkar et al., 2017), 20190711A (Heintz et al., 2020) and 20210117A(**?**), associations show that FRBs can originate in less massive – and therefore fainter – hosts than the primarily massive, star-forming hosts shown in this sample. With our high-resolution, deep AO imaging, we may test the scenario in which the true host is a dwarf and possible companion to the putative host, along with the scenario where a higher-z, background galaxy may be the true host.

To put a constraint on a fainter host galaxy candidate at the FRB position, we use the GALIGHT residual images as shown in Figure 3.2, where the smooth elliptical components from the putative host have been removed to derive point-source limiting magnitudes (shown in Table 3.3) at the FRB position. We calculate the residual flux using a circular aperture of $0.5''$ in diameter and compute the net standard deviation for the pixels within this aperture. We then take the flux measurement with five times the net standard deviation as the upper limit on any point source flux that could be detected from the residual images. Our limits and visual inspection of the images indicate that there are no galaxies brighter than an apparent magnitude of 26 at the FRB position. At these redshifts, the limits of $L_{IR} \lesssim (0.02 - 0.39) \times 10^6\, L_\odot$ are significantly deeper than the luminosity of even the faintest known dwarf galaxies associated to FRBs, namely $10^8 < L_\odot < 10^9$ (e.g. Bassa et al., 2017; Bhandari et al., 2023).

3.3.4 Fractional Flux

We next examine the location of the FRBs relative to their host galaxy light distributions, a measure known as fractional flux ($\mathrm{F_F}$). The $\mathrm{F_F}$ is independent of host size and morphology, as the measurement determines the fraction of host light fainter than the flux at the burst position. A value of 1 would indicate that the transient occurred in the brightest location within

the host. This measure follows the F_F calculation used by Fruchter et al. (2006), which was an important factor in differentiating Long Gamma Ray Bursts (LGRBs) from core collapse supernovae (CC-SNe) locations in their respective hosts. In the IR, as with the K-band images presented here, we are able to probe the relationship between FRBs and the distribution of stellar mass in their hosts. A higher fractional flux in this regime points towards FRB locations coincident with high concentrations of stellar mass — like the centers of galaxies.

To determine F_F, we create a 2D cutout around each host galaxy large enough to include background pixels. We then identify the N pixels that lie within the 3σ FRB localization ellipse. The fractional flux for a given (ith) pixel within the localization ellipse is given by:

$$F_F = \frac{\Sigma_j^N (F_j < F_i)}{\Sigma_j^N F_j} \tag{3.1}$$

where F_i is the flux value in pixel i. We then weight the F_F values by the 2D Gaussian distribution of the FRB localization ellipse. The F_F values for each FRB can be found in Table 3.4. The values range from 0.24 to 0.64 with a median of 0.59. The lower and upper limits were set by FRBs 20211127I and 20211212A, respectively.

We combine our sample with the Mannings et al. (2021) sample to determine the distribution of these values for a larger sample of 10 FRB host galaxies. The additional hosts that were chosen are those with WFC3/IR F160W imaging that were not included in the sample imaged with Gemini (FRB 20121102A, FRB 20190102C, FRB 20190608B, FRB 20190711A, and FRB 20190714A). This will hereafter be referred to as the combined FRB sample, whereas the GeMS/GSAOI sample will be referred to as such.

In order to determine the uncertainty on the cumulative distributions, we utilize the method of Heintz et al. (2020) to create 10 000 realizations of asymmetric Gaussian PDFs using the calculated offset errors for each FRB. Finally, we use a bootstrap method to compute a

cumulative distribution function (CDF) of the bootstrapped sample and calculate the median of these CDFs, in addition to the lower and upper bounds for each bin. Figure 3.4 shows the fractional flux CDF for the combined FRB sample along with the cumulative distributions of other transient class samples pulled from other publications (Fong et al., 2010; Fong and Berger, 2013; Wang et al., 2013; Lunnan et al., 2015; Blanchard et al., 2016).

In Figure 3.4 we can see that the FRB cumulative distribution (shown in black) differs markedly from the distributions of Short Gamma Ray Bursts (SGRBs, red) and LGRBs (orange). The FRB distribution appears similar to that of the 1-1 line (blue), Type-Ia SNe (purple) and CC-SNe (green). However, due to the small sample size (10 FRBs) and the FRB positional uncertainties, the overall uncertainty is substantial and cannot be ignored. We also assume here that the 10 FRBs have the same physical origin, which cannot necessarily be taken for granted. We explore these relationships with more rigorous statistical testing.

Using the Kolmogorov-Smirnov (KS) test, we test the null hypothesis that FRBs come from the same underlying distribution as the samples of other transient classes shown here. We require $P_{KS} < 0.05$ in order to reject this null hypothesis. We test against CC-SNe, SGRBs, LGRBs, and Type Ia SNe. The resulting P_{KS} values are shown in the legend of Figure 3.4. We find that the KS-test rejects the null hypothesis that SGRBs or LGRBs are from the same underlying population as FRBs. CC-SNe, and Type Ia-SNe could not be rejected.

3.4 FRB Physical Locations and Offsets

In this section, we study the locations of the FRBs in our sample with respect to their host galaxy centers and spiral structure. We introduce their angular and physical offsets (θ and δR, respectively); their "host-normalized" offsets ($\delta R/r_{\rm e}$), which are normalized by the half-light radii $r_{\rm e}$ of their host galaxies; and the locations with respect to the closest spiral arm

of their host galaxy (spiral offset; SO). We then compare the galacto-centric offset distributions to distributions of other transient events as we did for F_F in §3.3.4. We also investigate the relationship between FRBs and spiral arms and how this compares to other transient populations and previous FRB studies.

3.4.1 Galacto-centric Offsets

The shape, size, and orientation of FRB localization ellipses must be taken into account when determining the angular, physical, and host-normalized offsets from the center of their host galaxies. We define ellipsoidal regions representing the uncertainty in the FRB position relative to its host galaxy nucleus.

Following the scheme from Mannings et al. (2021), we apply a weighted 2D Gaussian probability distribution centered on the FRB localization ellipse to determine the mean and variance in θ. Because the host of FRB 20210117A is not detected, it is not included in this analysis. FRB 20181112A is also not included due to (i) the large uncertainty relative to the size of the host and (ii) the host not being identified by GALIGHT at sufficient significance (see §3.3.1).

The projected angular offsets (θ) range between $0.7''$ and $5.0''$, with a median value of $2.0''$. These values are included in Table 3.4. We then converted these angular offsets to physical offsets using the host redshifts and our assumed cosmological model (§3.1). The physical offsets range from 2.0 to 11.9 kpc, with a median value of 3.4 kpc. For comparison, we determine the median of the distribution of galactic globular clusters presented by **?**, which is 7.7 kpc. Finally, we used the half-light radii r_e (see §3.3.1) of the hosts to determine the host-normalized offsets $\delta R/r_e$. The median host-normalized offset for this sample is $2.1r_e$. This is larger than the median expected offset if FRBs traced the locations of stars in their disks and fell within the half-light radius of the host galaxy (i.e., $1r_e$).

To determine the uncertainty on the cumulative distributions, we again utilize the

Table 3.4: θ refers to the angular offset of the FRB from the center of the host galaxy. δR is this offset in physical units. $\delta R/r_e$ is the host normalized offset. $\tilde{R}_{min}$ is the offset of the FRB from the closest spiral arm of the host galaxy. $\mathrm{F_F}$ is fractional flux.

FRB	θ	δR	$\delta R/r_{\mathrm{e}}$	$\tilde{R}_{min}$	$\tilde{R}_{min}$	F_F
	(arcsec)	(kpc)		(arcsec)	(kpc)	
20180924B	0.72 ± 0.17	3.47 ± 0.83	8.09 ± 1.93	0.49 ± 0.07	2.36 ± 0.34	0.55 ± 0.26
20191001A	0.94 ± 0.18	3.63 ± 0.69	2.09 ± 0.40	0.32 ± 0.12	1.21 ± 0.46	0.64 ± 0.11
20210807D	5.00 ± 0.40	11.91 ± 0.95	4.32 ± 0.34	0.07 ± 0.07	0.16 ± 0.16	0.47 ± 0.24
20211127I	2.18 ± 0.40	2.07 ± 0.38	0.74 ± 0.13	0.55 ± 0.28	0.53 ± 0.27	0.24 ± 0.10
20211212A	2.04 ± 0.72	2.84 ± 1.00	1.20 ± 0.42	0.08 ± 0.09	0.11 ± 0.12	0.67 ± 0.18
Median	2.04 ± 0.72	3.47 ± 0.83	2.09 ± 0.40	0.32 ± 0.12	0.53 ± 0.27	0.55 ± 0.26

method of Heintz et al. (2020) as described in §3.3.4. In Figure 3.5, the left panel shows the physical offset CDF for the combined sample, and the right panel shows the host-normalized CDF for the combined sample of FRBs. The gray shaded region depicts the uncertainty for each distribution.

Again, we utilize the KS test, with a $P_{KS}< 0.05$ requirement in order to reject the null hypothesis. We test against CC-SNe Schulze et al. (2020)), SGRBs and LGRBs Fong et al. (2010); Fong and Berger (2013); Blanchard et al. (2016)), Ca-rich transients (Lunnan et al., 2017; De et al., 2020), Super-luminous Supernovae (SLSNe; Lunnan et al. (2015); Schulze et al. (2020)) and Type Ia supernovae (Uddin et al., 2020). We also test against a distribution of magnetars as modeled by Safarzadeh et al. (2020). The resulting P_{KS}values are shown in the legend of Figure 3.5.

We find that, with the resulting P_{KS} values, the KS-test rejects all transient samples except CC-SNe for projected offsets. In the case of host-normalized offsets, only Ca-rich transients are rejected.

3.4.2 Offset from Spiral Arms

To investigate the location of FRBs relative to the spiral arms of their host galaxies, we determined the minimum distance from the FRB to the closest projected spiral arm in the host galaxy. This spiral arm offset is referred to as $\tilde{R}_{min}$.

To estimate $\widetilde{R}_{min}$, we first convolve the GALIGHT residual image (the original image minus the GALIGHT model; see §3.3.1) using a smoothing kernel of 5 pixels. We then mask all values below a threshold of 0.6 — chosen after experimentation — to isolate pixels not associated with spiral arms. Custom masks were then created for each host to mask sources clearly not associated with the spiral arms of the host (e.g. nearby galaxies, or field stars in projection). All unmasked pixels were taken as part of the host galaxy spiral arm structure. We then calculated

the minimum, 2D Gaussian weighted offset between the FRB and the nearest unmasked pixel. This methodology mirrors that of galacto-centric offset calculation. These $\widetilde{R}_{min}$ values are reported in Table 3.4. We show an illustrative image of this analysis in Figure 3.6, where we define 0.25σ contours as the edges of the spirals.

The $\widetilde{R}_{min}$ values range from $0.07''$ to $0.55''$ with a median value of $0.42''$ or physical minimum separations of 0.11 to 2.36 kpc with a median value of 0.53 kpc. Two of the five FRBs (20210807D and 20211212A) have an $\widetilde{R}_{min}$ value consistent with zero at 95% confidence.

3.5 Discussion

3.5.1 Using AO to Image FRB Host Galaxies

This dataset presents the first ground-based AO sample of FRB host galaxies. This demonstrates our ability to match space-based depth and resolution with ground-based resources in the near-IR. Given the increasing sample of precisely localized FRBs, it will be critical to include ground-based observations to complement more expensive, space-based surveys.

While ground-based observations are currently limited to IR wavelengths, these do provide a detailed look at the distributions of stellar mass in these hosts, morphologies, and the connections between bursts and older stellar populations. The 5σ magnitude limits, indicating the deepest objects detectable in these images, are listed in Table 3.3. In comparison with the limiting magnitude calculations obtained with HST by Mannings et al. (2021), we have achieved a similar depth using GeMS/GSAOI with a fraction of the integration time (between 500 and 2000 seconds) in comparison to almost 3000 seconds with HST, thanks to the light gathering power of an 8 metre telescope. With HST, as presented by Mannings et al. (2021), the spatial resolution is $\sim 0.2''$, while our GeMS/GSAOI images had a delivered image resolution of $\sim 0.06''$.

3.5.2 Spiral Structure in FRB Hosts

Four out of five hosts in the GeMS/GSAOI sample that were successfully imaged show clear spiral arm structure, even though these galaxies were not pre-selected based on known spiral arm morphology. These FRBs are all non-repeaters. The host galaxies are at a range of inclination angles from 33° (FRB 20211127I) to 59° (FRB20210807D).

Using GALIGHT, we determined the half-light radii of these five host galaxies and produced residual images which further highlight the spiral and low surface-brightness structures in these hosts. Echoing the results of Mannings et al. (2021), we show that most of the bursts which occur in spiral hosts, also occur on or near the spiral structures. This proximity to regions of relatively concentrated stellar mass is also illustrated by the $\Sigma_{\mathrm{M}*}$(FRB) (see Figure 3.3) which shows more than half of the FRBs in the GeMS/GSAOI sample occurring in a region of elevated stellar mass density. This is in stark contrast to SGRBs, for example, as they occur at high offsets and are therefore separated from the stellar mass in their hosts (e.g., **?**).

Using the residual images, we determine the minimum distance of each FRB to the closest spiral arm in the host galaxy (designated $\widetilde{R}_{min}$). The $\widetilde{R}_{min}$ values range from 0.11 to 2.36 kpc with a median value of 0.53 kpc. The FRBs are significantly closer to spiral arms of their host compared to the center of their host galaxy, with a median galacto-centric offset being 3.47 kpc. The FRBs tend to be on or near a spiral arm but not coincident with the brightest portions of the spiral arm. We discuss the light at the location of the FRB in more detail in §3.5.3.

Abdeen et al. (2022) find evidence supporting the existence of age gradients in spiral arms, as predicted by density wave theory (Lin et al., 1969). Stars between 0-10 Myr tend to closely map the spiral arms of the host galaxy, trailing the arm slightly (see Figures 3 and 4 of Abdeen et al. (2022)). Magnetars are a compelling theoretical source of FRBs due to their

compact size and extreme magnetizations. Notably, they are included in this younger population of stars. Therefore, if a majority of FRBs are associated with young magnetars, we would expect these to occur on or slightly trailing a spiral arm. FRBs 20210807D and 20211212A, within their respective uncertainties, are potentially coincident with a spiral arm of their host. FRBs 20191001A and 20211127I could potentially be leading one spiral arm or trailing another arm.

Aramyan et al. (2016) and Karapetyan (2022) map the locations of extremely well-localized Type II and Type Ia SNe, respectively, relative to the spiral arms of their host galaxies. The authors created radial light profiles from the center of the galaxy extending through the transient's location. They were able to precisely determine the location of each SN within the spiral arm of the respective host galaxy. Aramyan et al. (2016) finds that each SN in their sample is within the inner and outer bounds of a spiral arm, which are defined by a zero threshold in the residual galaxy image. This residual image is found by subtracting a bulge+disc model from the original image, similar to what we have done in this study. However, there are variations according to each type of SNe. For example, SNe Ibc occur closer to the leading edges of the arms than do SNe II. Karapetyan (2022) finds that the "normal" Type Ia SNe (defined by the light-curve decline rate) span a range of distances from the spiral arm peaks; occurring within the edges of the spiral arms as well as in inter-arm regions. In the future, with a move towards i) consistent milli-arcsecond scale localizations and ii) larger sample sizes due to CHIME Outriggers, CRACO on ASKAP, and DSA-110, we hope to expand the study of spiral arm offsets in FRBs to obtain more precise measurements of the location of FRBs relative to the substructure of the spiral arms of their hosts.

3.5.3 FRB Galacto-centric Offsets and Light locations

We calculated the projected offset of the FRBs from their host centers. We combined this GeMS/GSAOI sample of FRBs with the FRBs from Mannings et al. (2021) to create Figure

3.5 with a larger sample of FRBs (10 FRBs). At high statistical significance, five out of six transient classes included (SGRBs, LGRBs, Ca-rich transients, and SLSNe) are rejected as coming from the same underlying population as FRBs. We aer unable to reject this ull hypothesis with respect to CC-SNe and Type Ia. Heintz et al. (2020) find that CC-SNe are confidently not rejected.

We use the effective radius from GALIGHT to calculate the host-normalized projected offset of each FRB. Through a KS test shown in the right panel of Figure 3.5, Ca-rich transients are rejected as coming from the same underlying population as FRBs, while SGRBs, LGRBs, and CC-SNe are not rejected. Similarly, Heintz et al. (2020) does not reject CC-SNe.

In terms of fractional flux, FRBs are distinctly different from LGRBs, which tend to occur in brighter regions of their host galaxies (e.g. Fruchter et al., 2006). The locations of FRBs with respect to their host's brightness is also distinct from SGRBs (e.g. Fong et al., 2010). FRBs, however, are not distinguished from CC-SNe and Type Ia-SNe in terms of fractional flux.

As shown in Figures 3.4 and 3.5, the hypothesis that FRBs and CC-SNe are from the same underlying population is not rejected based on projected offset, host normalized offset, or fractional flux. Our findings on the local environment scale are consistent with the findings of Bochenek et al. (2021) which investigated global host properties. Bochenek et al. (2021) compared a sample of FRB host galaxies with the galaxies of CC-SNe, LGRBs, and SLSNe-I. LGRBs and SLSNe-I were rejected as coming from the same underlying population as FRBs, while CC-SNe were not rejected. The Milky Way magnetar population is dominated by magnetars born in CC-SNe (Bochenek et al., 2021). Thus if magnetars are the dominant FRB progenitor, and the Milky Way magnetar population is representative of the magnetar population overall, then FRB host galaxies should be consistent with the host galaxies of CC-SNe (Bochenek et al., 2021). However, while this connection appears plausible for the sample of FRBs presented in this paper, we cannot assume the Milky Way magnetar population is representative of all FRB

progenitors. There are several exceptions to the typical spiral host galaxy, such as the FRB from a globular cluster (e.g. Bhardwaj et al., 2021), FRBs in dwarf galaxies (e.g. Bhandari et al., 2023), and various FRBs that are not coincident with star-forming regions in their host galaxies (e.g. Dong et al., 2023), which is where we might expect more massive progenitors to be located. Additionally, in these tests we assume that the FRBs in this sample all have the same physical origin, which is not necessarily the case. The possible magnetar connection — or more clearly, CC-SNe connection — seems relevant for this sample of FRBs specifically, but broad characteristics of FRB host galaxies overall might point towards a multitude of pathways. The possibility for multiple pathways is supported by the ability to explain some of the exceptions listed above (FRB in a globular cluster, elliptical hosts, etc.) with a Type Ia related source or progenitor. In order to differentiate between possible connections to these different transient classes, we must at least double the sample size.

The confidence in these *individual* measurements is largely limited by the FRB localization precision. The pixel scale of GSAOI in particular is approximately $0.02''$ per pixel. Not until we reach a precision of 10s of mas localizations will the measurements then be limited by image resolution. Even still, future studies that leverage the higher-precision localizations will be able to glean a great deal of information about FRB local environments with existing high-resolution imaging resources and upcoming ELTs (Bannister et al., 2019).

3.6 Conclusions

In this paper, we use high-resolution images from GeMS/GSAOI to perform a detailed study of the environments of five FRBs. Using these data, we make measurements of galactocentric offset (§3.4), fractional flux (§3.3.4), stellar mass surface density (§3.3.2), and offset from spiral arms (§4.3.3). We also demonstrate the feasibility of creating samples of high-resolution

imaging of FRB hosts using AO-supported ground-based resources.

From each of these measures, we found that FRBs are located at moderate offsets (median host-normalized offset of 2.09 $r_{\rm e}$), compared to other transient classes such as LGRBs and Ca-rich transients. These bursts also appear on or close to the spiral structure in their hosts, with a median distance of 0.53 kpc.

As for the light at the FRB location, the IR fractional flux demonstrated that the combined samples of FRBs trace the distribution of stellar mass, similar to CC-SNe. We also examined the FRB location in terms of stellar mass surface density, finding 4/5 FRB sites to be elevated in this quantity compared to the global value. In combination, these findings point towards a possible similarity between FRB local environments and those of CC-SNe. This is a finding supported by the conclusions of Bochenek et al. (2021), which finds similarities between the global properties of FRBs hosts and CC-SNe hosts. However, we must take into account the inability to reject an underlying connection between FRBs and Type Ia SNe. The local environment and host characteristics should be explored with respect to Type Ia supernovae, in general, and different Type Ia progenitors, specifically (as explored by Karapetyan (2022)).

With many well-localized FRB detections looming on the horizon due to upgraded experiments and new instruments coming online, we will be able to better characterize the properties of FRB environments relative to their host galaxies and other transient classes. Doubling the number of FRB detections with localizations comparable to those presented here will already provide greater opportunity for discernment. With a 5x or 10x increase in sample size, along with milli-arcsecond precision localizations, it seems we will be able to make strong conclusions about FRB local environments and origins. Additionally, the increasing sensitivities of instruments will facilitate studies at higher redshifts. It is necessary that we utilize all resources available to prepare for and attend to the large number of incoming FRB detections and precise localizations. In combination with possibleJames Webb Space Telescope (JWST),

HST, Extremely Large Telescope (ELT), and archival data, adaptive optics will prove to be an effective tool.

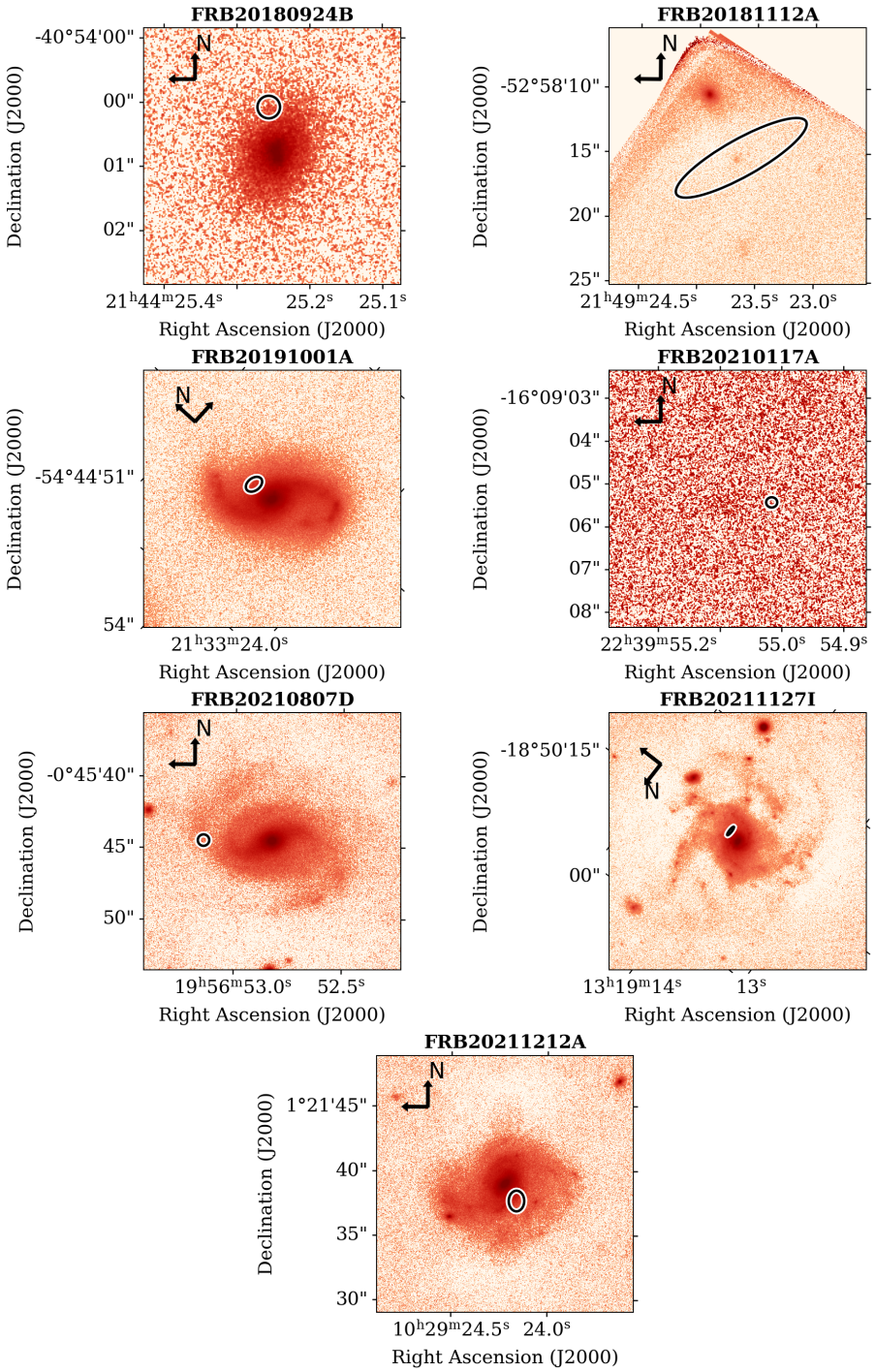

Figure 3.1: GeMS/GSAOI imaging of the seven host galaxies in our sample in the K_s filter. The black dashed ellipse in each image represents the 68% confidence level FRB localization region. The black arrows indicate North and East.

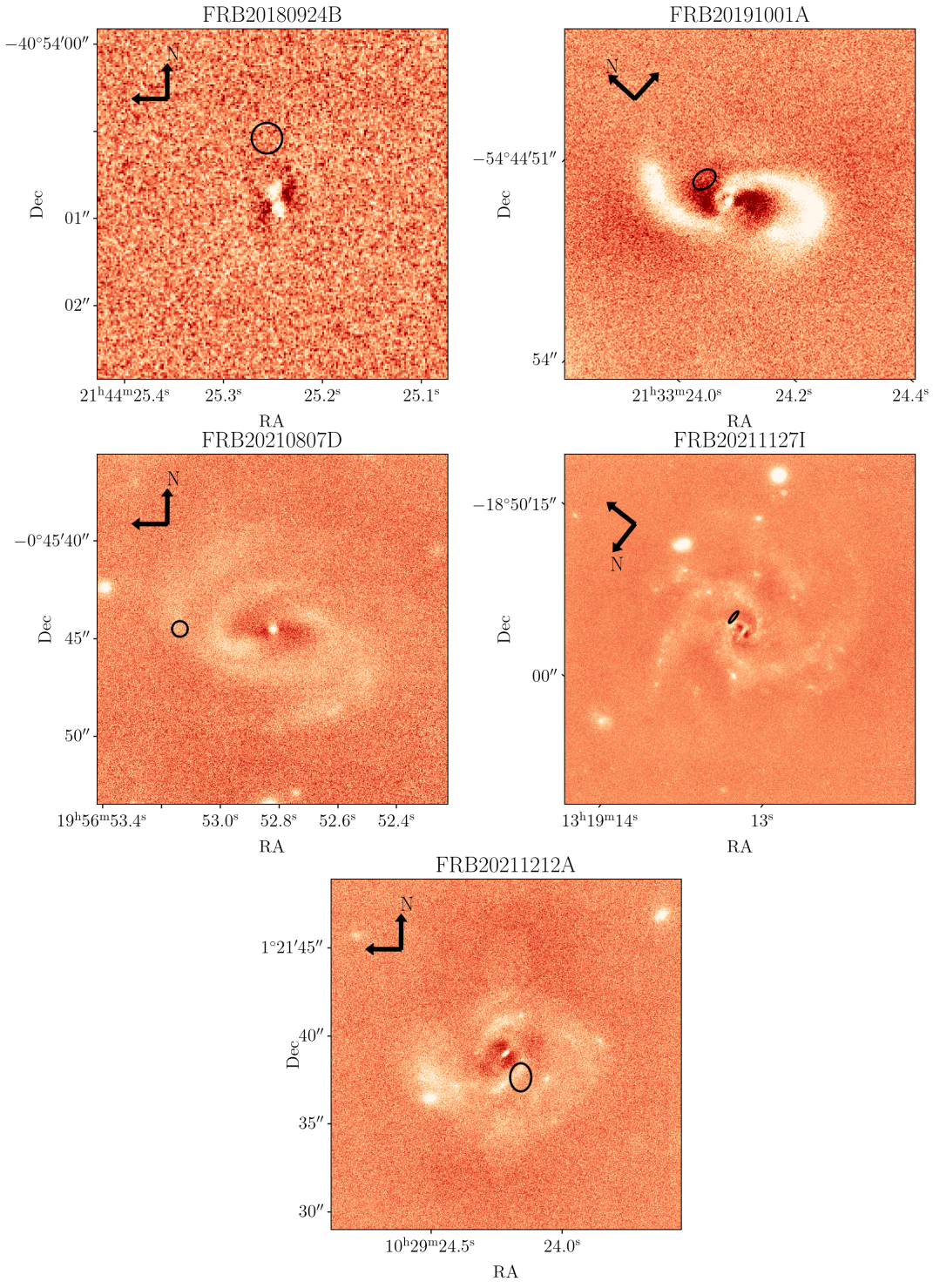

Figure 3.2: Residual images produced by subtracting the GALIGHT model from the original images for the objects with host detections. The black ellipse in each image represents the FRB localization region. North and East are indicated by the black arrows in the top left. Light regions show a flux excess, while dark regions show a flux deficit.

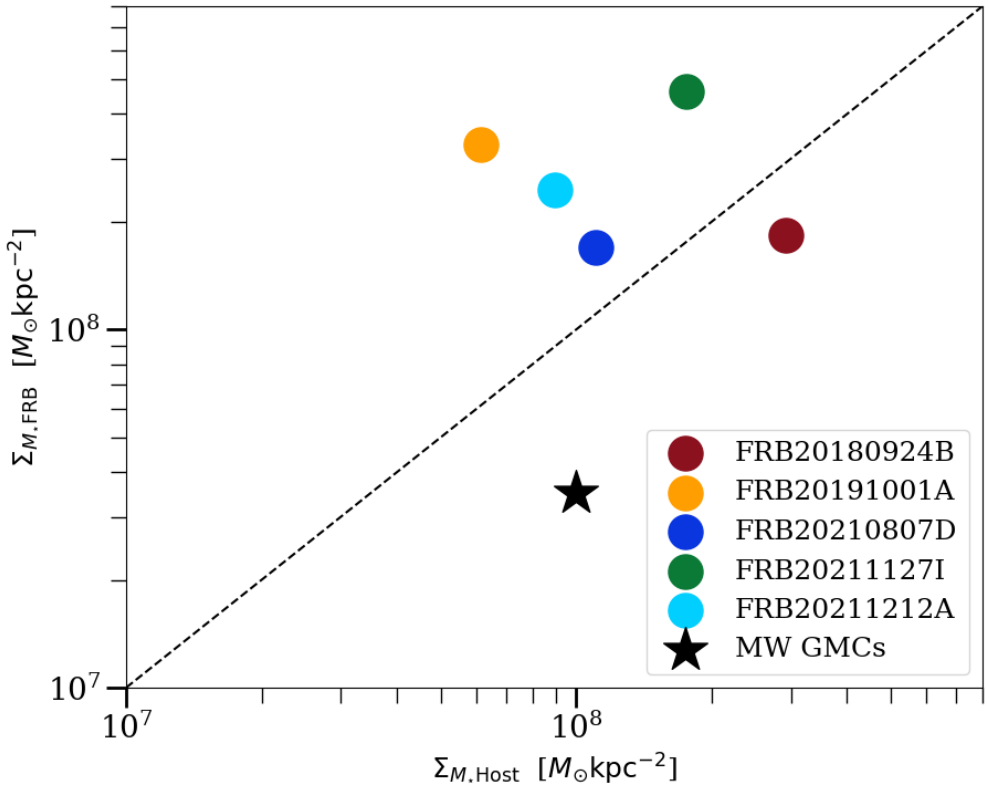

Figure 3.3: The average stellar mass surface density at the burst site vs. average stellar mass surface density of the host. The dashed line shows the 1:1 relation. The error bars for each point are significantly smaller than the marker size. For context, we have also plotted giant molecular clouds (GMCs; black star) within the Milky Way. We note that the FRBs preferentially occur in regions of higher local surface density than the Milky Way GMCs.

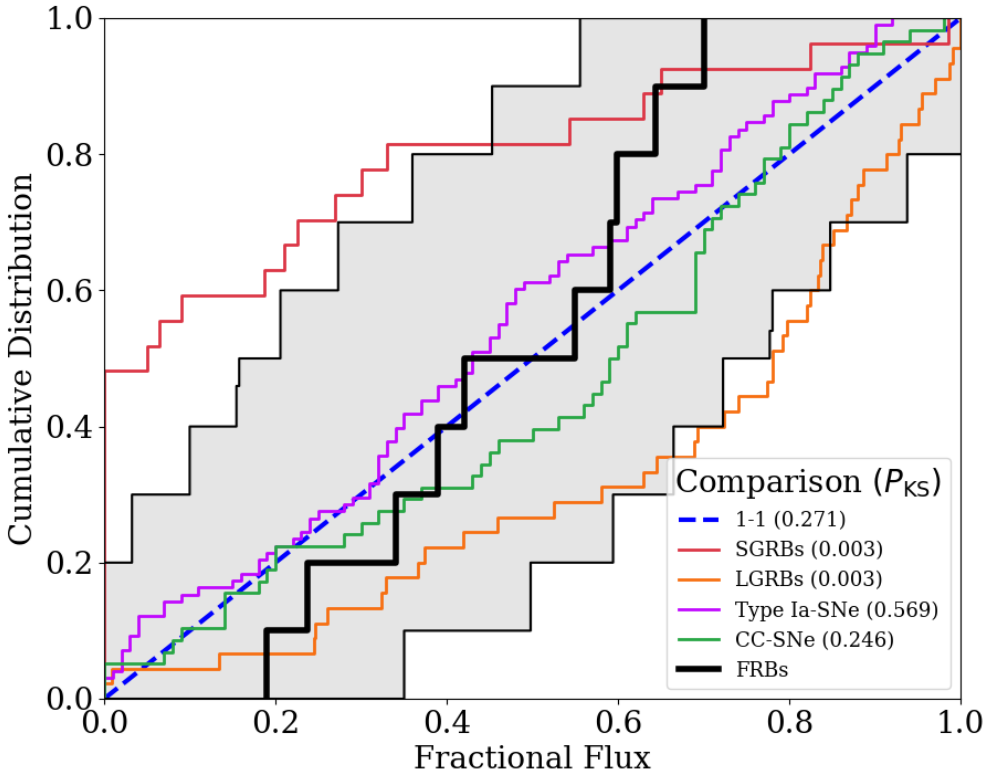

Figure 3.4: Cumulative distribution of the fractional flux of the combined FRB sample (10 FRBs): the five FRBs in the sample that had hosts detected in our K_s adaptive optics imaging, in addition to the FRBs from Mannings et al. (2021) that were imaged with F160W [1385.77-1700.31 nm]. The gray-shaded region is a bootstrap estimate of the RMS of the distribution, which accounts for both uncertainties in individual measurements and statistical uncertainties due to the sample size. We compare this distribution to those of SGRBs (red; Fong et al. (2010); Fong and Berger (2013)), LGRBs (orange; Blanchard et al. (2016)), Type-Ia SNe (purple; Wang et al. (2013)), CC-SNe (green; Lunnan et al. (2015)), and a 1-1 line shown in blue. The SGRB and LGRB samples are rejected by the KS-test, implying they are not from the same underlying population as FRBs.

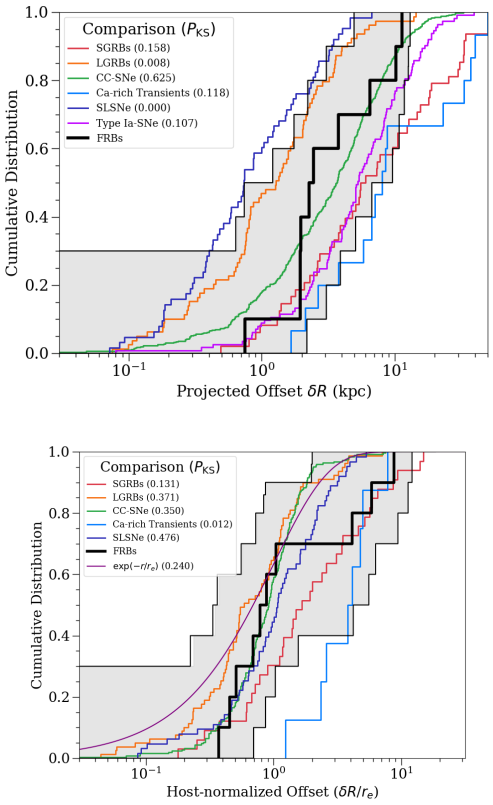

Figure 3.5: *Left*: Cumulative distribution of the offsets of the combined FRB sample (10 FRBs). We plot other transient classes for comparison including SGRBs (red; Fong et al. (2010); Fong and Berger (2013)), LGRBs (orange; Blanchard et al. (2016)), Ca-rich transients (light blue; Lunnan et al. (2017); De et al. (2020)), CC-SNe (green; Schulze et al. (2020)), SLSNe (dark blue; Lunnan et al. (2015); Schulze et al. (2020); Hsu et al. (2023)), and Type-Ia SNe (purple; Uddin et al. (2020)). *Right*: Same as left but using host-normalized offset.

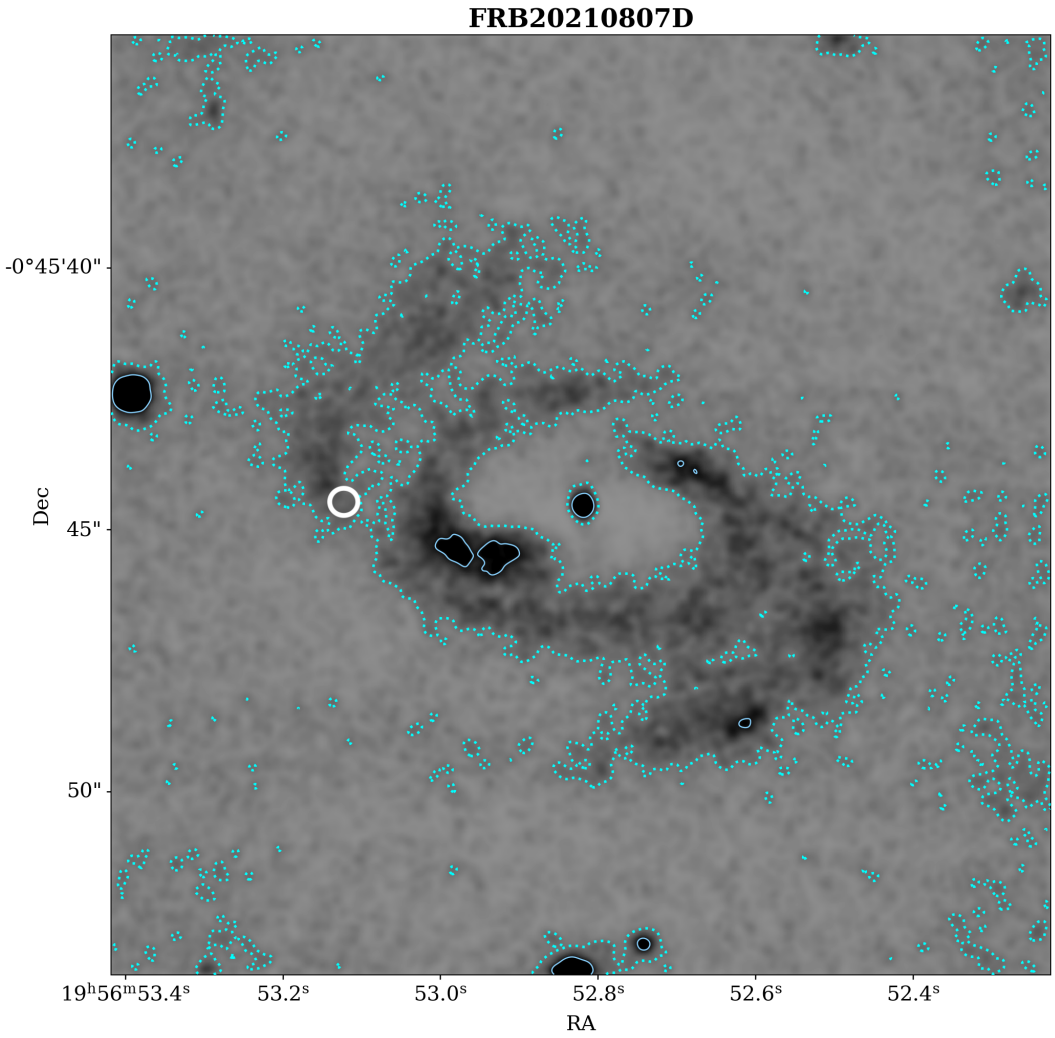

Figure 3.6: Example contour plot showing the extent of the spiral structure in the host of FRB 20210807D. The $\tilde{R}_{min}$ measure, computes the distance between the FRB localizaton (shown in white) and the nearest unmasked pixel that is determined to be part of the spiral arm. The contours highlight the 0.25σ and 1σ levels. The $\tilde{R}_{min}$ measured for this burst is $0.07''$.

Chapter 4

Connections between the Local Environment and Burst Characteristics

4.1 Introduction

After consistently finding super-luminous supernovae (SLSNe) in low-metallicity hosts (e.g. Leloudas et al., 2015), it became clear that this was no coincidence. Nicholl et al. (2017a) discuss the effects that such low-metallicity conditions would have on the spectral and luminosity characteristics of SLSNe, and develop scenarios that require low metal abundances and millisecond magnetars to reproduce observations. The combination of light curve information, spectral classifications, host characteristics, and local measures provide the context necessary to advance explanations of this mysterious type of supernova.

While studies that focus on host galaxy and local environment properties alone can be very illuminating with respect to the possible origins of FRBs, it is now apparent that burst characteristics must be considered within this analysis as well. The field has shifted from a picture of FRBs that relates closely to the origins of transients such as SLSNe (in the case of

FRB 20121102A, e.g. Marcote et al., 2017) to studies that now show overlap between the host characteristics of FRB hosts and the hosts of Type Ia supernovae (Horowicz and Margalit, 2025).

This ambiguity can be lightened by approaching local environment studies with the added dimension of burst properties. By better understanding how a particular environment may affect burst characteristics — and how to identify these imprints — we can get closer to resolving the blurry image of FRB origins.

In this paper we aim to holistically characterize FRBs through comparisons of burst characteristics such as dispersion measure (DM), rotation measure (RM), scattering time (τ), fluence, and intrinsic burst width to local measures such as stellar mas surface density ($\Sigma_{\rm M*}$), fractional flux ($\rm F_F$), and the distance from spiral arms ($\widetilde{R}_{min}$). The paper is structured as follows: in §4.2 we discuss sample selection and the data used in this study; in §4.3 we discuss measurements of light concentration, stellar mass surface density and the minimum distance to spiral arms; in §4.4 we look at local measures and burst characteristics together; finally, in §4.5 we discuss the implications of our results.

4.2 FRB Data and Sample Selection

4.2.1 Host Images and Burst Information

For this analysis, we require an image resolution that approaches or surpasses the burst localization precisions. Therefore, we utilize previously published Hubble Space Telescope Wide Field Camera 3 (HST/WFC3) NIR images (Bassa et al., 2017; Chittidi et al., 2021; Tendulkar et al., 2020; Mannings et al., 2021). These data were taken under programs 15878 (PI: Prochaska), 16080 (PI: Mannings), 4890 (PI: Tendulkar) and 16072 (PI: Tendulkar). We also make use of K-short images taken with the Gemini Multi-conjugate Adaptive Optics System (GeMS)/Gemini South Adaptive Optics Imager (GSAOI) as presented by Woodland et al. (2024) These data were

collected as part of the programs GS-2021A-147C-2, GS-2021B-C-3, and GS-2022A-C-2. Finally, we include Very Large Telescope (VLT) HAWK-I infrared (K-short) images taken in conjunction with the data presented by Shannon et al. (2024). This is the first time the VLT images are being used for local environment studies, so, in order to be included, they were required to pass the following criteria:

- Available K_s image
- Localization area is less than 20% of the circular host area (within 1 effective radius)

Details on image processing for all the included images can be found in their respective publications (HST: Bassa et al. (2017); Chittidi et al. (2021); Tendulkar et al. (2020); Mannings et al. (2021); GSAOI: Woodland et al. (2024); VLT: Shannon et al. (2024)).

Since some of the hosts were included in multiple programs, we ranked images according to the priority of use. Our highest priority images were those from HST, where GSAOI images followed, and VLT images were the lowest priority.

For each FRB we collate information published on rotation measures (RMs), dispersion measures (DMs), and scattering times (τ). As some of the bursts are detected at different frequencies, we use 1 GHz scattering times for the analysis presented here. All relevant burst characteristics and associated references can be found in Table 4.1.

4.2.2 `GALFIT` and Galaxy Profile Fitting

Our analysis also requires the use of galaxy profile fitting as we study, for example, the relationships of bursts to spiral structure. We use `GALFIT` products that will be published in cite Gordon et. al, in prep, including smooth profile parameters produced by `GALFIT` along with host residuals. Similar profile fitting was previously performed for hosts with HST and GSAOI images Mannings et al. (2021); Woodland et al. (2024), but for the purpose of uniformity, all

Table 4.1: References: 1. Tendulkar et al. (2017), 2. Marcote et al. (2017), 3. Marcote et al. (2020), 4. Bannister et al. (2019), 5. Bhandari et al. (2020b), 6. Day et al. (2020), 7. Day et al. (2021), 8. Macquart et al. (2020), 9. Heintz et al. (2020), 10. Bhandari et al. (2020a), 11. Shannon et al. (2024), 12. Kumar et al. (2022), 13. Gordon et al. (2023)

FRB	RM	DM	τ	$\tau_{1\,\mathrm{GHz}}$	Fluence	Refs.
	$(\mathrm{rad\,m^{-2}})$	$(\mathrm{pc\,cm^{-3}})$	(ms)	(ms)	(Jy ms)	
FRB20121102A	102700.00 ± 100.00	558.10 ± 1.00	0.024	0.024	1.2	1,2
FRB20180916B	-114.60 ± 0.60	348.76 ± 0.10	0.003	0.003	2.53	3
FRB20180924B	18.00 ± 2.00	362.16 ± 0.01	0.590	1.560	16.0	4,5,6,7
FRB20190102C	-106.30 ± 1.00	364.55 ± 0.00	0.027	0.090	14.0	5,6,7
FRB20190608B	351.00 ± 2.00	340.05 ± 0.60	3.830	8.500	26.0	5,6,7
FRB20190611B	20.00 ± 4.00	332.63 ± 0.04	0.044	0.030	10.0	6,7,8
FRB20190711A	0.00 ± 2.00	587.90 ± 1.00	0.008	0.011	34.0	6,7,8
FRB20190714A	—	504.13 ± 0.10	0.422	0.830	12.0	7,9
FRB20191001A	50.50 ± 0.90	507.00 ± 0.07	4.520	1.780	143.0	5,7,10,11
FRB20201124A	-613.00 ± 2.00	411.00 ± 1.00	11.100	− − −	—	12
FRB20210807D	—	251.30 ± 1.00	—	—	113.0	11,13
FRB20211127I	−67.50	234.97 ± 1.00	0.012	0.020	31.0	11,13
FRB20211212A	54.00	209.00 ± 1.00	1.800	8.000	36.0	11,13
FRB20220725A	−26.00	290.40 ± 0.30	2.290	1.950	72.0	11
FRB20221106A	445.00	343.80 ± 0.80	0.182	0.250	80.0	11
FRB20231226A	428.90	329.90 ± 0.10	0.170	0.250	78.0	11
FRB20240201A	1275.00	374.50 ± 0.20	0.780	0.460	47.0	11
FRB20240210A	−325.00	283.73 ± 0.05	0.100	0.590	26.0	11

such fitting was completed again — including VLT images — for the detailed offset analysis shown in Gordon et. al, in prep.

4.3 FRB Association with Light and Structure in Hosts

4.3.1 Stellar Mass Surface Density

We compute the stellar mass surface density for each of the FRBs in our sample. This is a measure of the stellar mass ($M_\odot$) per square kilo-parsec — here we present a weighted average over the FRB localization area with methodology described by Mannings et al. (2021) and Woodland et al. (2024).

The average stellar mass surface density (Σ_{M*}) of the Milky Way is $\approx 10^8\,M_\odot\,kpc^{-2}$ (shown with the blue dotted line in Figure 4.1). The median of the FRB sample is shown with the black vertical line, and the average Σ_{M*} of the Orion A star-forming region in the Milky Way is shown by the green dashed line. Approximately 75% of FRBs are in regions with Σ_{M*} less than the Milky Way average, and 100% of the locations show Σ_{M*} lower than that of a Milky Way star-forming region.

It should be noted, however, that FRB localizations (and image resolution for hosts with $z > 0.1$) smooth over pc-scale structures and associated variations in stellar mass concentrations. We extrapolated the stellar mass surface density of a Milky Way star-forming region from pc- to kpc-scales, therefore this value likely overestimates the stellar mass surface density over a scale similar to that of FRB localizations.

4.3.2 Fractional Flux

Another means of characterizing the light at the FRB location is by computing the fractional flux. This method characterizes the brightness of a pixel by taking the ratio of the

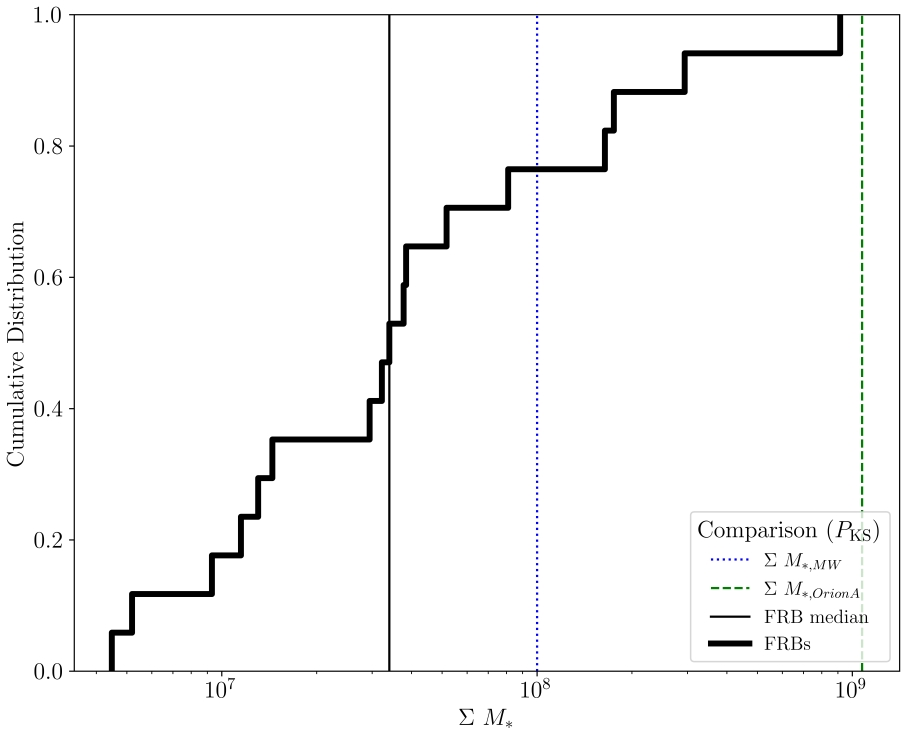

Figure 4.1: Stellar mass surface density cumulative distribution for FRBs shown with the median in black. Green vertical line: stellar mas surface density for the Orion A star-forming cloud in the Milky Way. Blue vertical line: Average stellar mass surface density in the Milky Way. The median of the distribution falls below the average value for the Milky Way. The distribution in its entirety falls below the estimate for Orion A.

total sum of flux in pixels fainter than a given pixel and the total flux in the all of the host's pixels. The equation given below shows how we implement this.

$$F_F = \frac{\Sigma_i(F_i < limit)}{\Sigma F} \tag{4.1}$$

Fractional flux has proven to be a powerful tool in characterizing and differentiating the environments of various transient events including supernovae, LGRBs, and SGRBs (e.g. Fruchter et al., 2006; Fong and Berger, 2013). Previous works (Chittidi et al., 2021; Mannings et al., 2021; Woodland et al., 2024) have explored fractional flux measurements associated with FRB localizations in high-resolution, NIR and NUV images of hosts. We complete similar analysis here, and increase the sample to include FRBs with VLT HAWK-I images. Following the methods of these papers, we compare the fractional fluxes of FRB locations to those of other transient populations.

The environments of events such as SGRBs and LGRBs are relatively well characterized and distinct, with SGRBs occurring in the faint outskirts of galaxies and LGRBs occurring in dense, bright inner regions of their hosts. We compare our sample to SGRBs, LGRBs, Type Ia supernovae, and Core-collapse supernovae. With KS-testing we test the null hypothesis that the transient samples come from the same underlying population. We require $P_{KS} < 0.05$ to reject this hypothesis, and therefore are only able to reject the SGRB and LGRB samples (as seen in Figure 4.2).

We are unable to reject CC-SNe and Type Ia-SNe. These results are consistent with findings published by Mannings et al. (2021) and Woodland et al. (2024). This relationship between FRBs and the two classes of SNe is explored further in a following section (§4.3.3) where we measure the minimum distance between the FRB location and the nearest spiral arm.

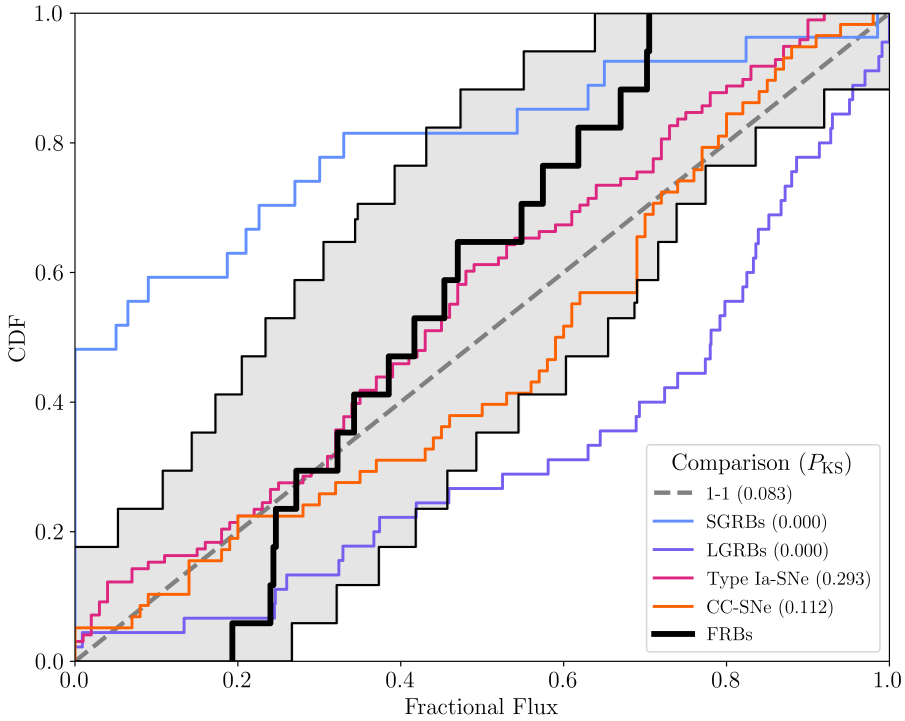

Figure 4.2: IR fractional flux cumulative distributions for FRBs and other transient classes. The FRB distribution is shown in black with the error region shaded gray. We compare to fractional flux distributions for CC-SNe (orange; Lunnan et al. (2015)), Type-Ia-SNe (pink; Wang et al. (2013)), LGRBs (purple; Blanchard et al. (2016)), and SGRBs (blue; Fong et al. (2010); Fong and Berger (2013)). With KS-testing we are able to reject the null hypothesis that SGRBs-FRBs and LGRBs-FRBs originate from the same underlying population for fractional flux (the relative brightness of local environment).

Table 4.2

FRB	$F_{F,IR}$	$\Sigma_{M_*\mathrm{FRB}}$
		$(10^8 \mathrm{M}_\odot \mathrm{kpc}^{-2})$
FRB20121102A	0.70 ± 0.07	0.130 ± 0.002
FRB20180916B	0.32 ± 0.07	0.115 ± 0.000
FRB20180924B	0.24 ± 0.11	0.810 ± 0.010
FRB20190102C	0.39 ± 0.25	0.093 ± 0.002
FRB20190608B	0.19 ± 0.06	0.340 ± 0.001
FRB20190711A	0.55 ± 0.27	0.045 ± 0.004
FRB20190714A	0.34 ± 0.23	1.752 ± 0.018
FRB20201124A	0.45 ± 0.03	9.149 ± 0.776
FRB20210807D	0.47 ± 0.24	1.641 ± 0.005
FRB20211127I	0.24 ± 0.10	0.377 ± 0.000
FRB20211212A	0.67 ± 0.18	2.940 ± 0.000
FRB20220725A	0.62 ± 0.09	0.294 ± 0.000
FRB20221106A	0.71 ± 0.02	0.384 ± 0.000
FRB20231226A	0.57 ± 0.21	0.052 ± 0.000
FRB20240201A	0.42 ± 0.13	0.145 ± 0.000
FRB20240210A	0.27 ± 0.12	0.516 ± 0.000

4.3.3 $\widetilde{R}_{min}$ Calculations

Here, we explore the minimum distance between the location of the FRB and the spiral arm structure in its host, which we shall refer to as $\widetilde{R}_{min}$. This analysis includes 15 FRBs where the host's spiral structure is apparent (identifiable above a 1-sigma level) in the residual images produced with `GALFIT`. This measurement can provide information on the delay times associated with the events, and therefore helping differentiate between particular progenitor classes. Within the residual images, we isolate pixels that are either 1-, 2-, or $3-\sigma$ above the sigma-clipped mean (depending on the S/N of the image) as the "spiral pixel", with bright, non-spiral pixels masked (e.g. foreground stars). We then calculated a weighted average of $\widetilde{R}_{min}$over the FRB localization region. The results for the FRB host sample are shown in Figure 4.3.

To further characterize the resulting FRB distribution, we compare to various models

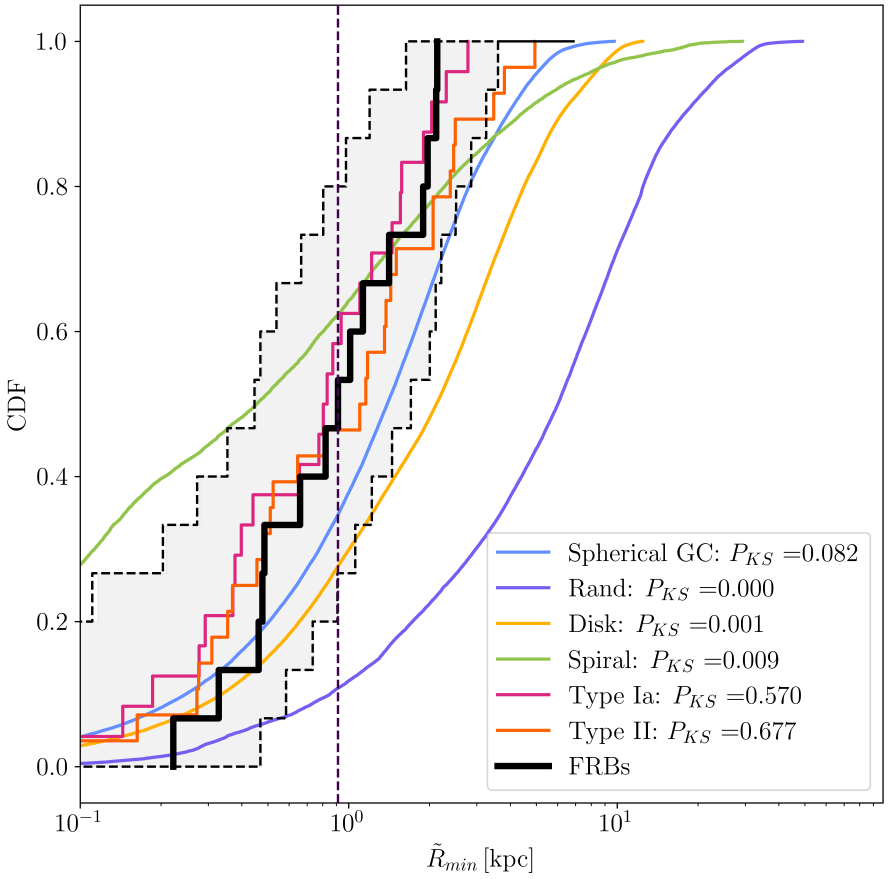

Figure 4.3: Minimum distance from a spiral arm (or distance to nearest spiral arm; $\widetilde{R}_{min}$) cumulative distributions. FRBs (black) are shown with associated error shown with gray shaded region. Also shown are distributions for a spiral model(color), disk model (color), Type-Ia SNe (pink; Bartunov et al. (1994)), Type-II SNe (orange; Bartunov et al. (1994)), a spherical globular cluster model (blue), and a random distribution (purple). KS-testing rejects the null hypothesis that FRBs-Spherical GCs and FRBs-Random samples are drawn from the same underlying distribution. We cannot reject the null hypothesis for the spiral, SNe, or disk distributions.

Table 4.3

FRB	r_e	i	PA
	(kpc)	(deg)	(deg)
FRB20121102A	2.05	70.73	76.24
FRB20180916B	6.00	46.04	−63.40
FRB20180924B	2.82	45.36	34.29
FRB20190102C	5.00	57.33	−10.54
FRB20190608B	7.37	5.44	−15.69
FRB20190611B	2.15	25.84	57.62
FRB20190711A	2.48	49.46	79.43
FRB20190714A	3.85	64.16	−12.38
FRB20191001A	6.67	47.74	19.53
FRB20201124A	1.99	50.93	−3.64
FRB20210807D	6.56	58.90	71.71
FRB20211127I	2.67	32.30	1.06
FRB20211212A	3.29	51.07	−78.24
FRB20220725A	6.44	52.61	−59.69
FRB20221106A	5.62	53.34	17.31
FRB20231226A	5.34	48.62	12.75
FRB20240201A	2.73	79.69	60.62
FRB20240210A	3.78	51.24	63.29

including: a Sérsic disk model based on Sérsic indices and effective radii produced by `GALFIT`; a spherical globular cluster distribution based on a modified Sérsic profile parameterization given by and used by Lim et al. (2024); a random distribution of points across the isolated galaxy image; and a spiral distribution.

4.3.3.1 Model Details

To create the disk models we produce two 1-D Sérsic models, along the x- and y-axes as determined by the effective radius, PA and inclination (see Table 4.3) of the respective host. We then use the Sérsic profiles as probability distributions along each axis to draw a random sample of points (also varying the quadrants from which we draw the points). We can then compute the minimum distance to a spiral arm for each of the randomly generated points.

We follow a similar structure for the spherical globular cluster distribution, as Lim et al. (2024) utilized a modified Sérsic profile to describe the distribution around a given galaxy. The radius of this distribution is determined by a Galaxy Mass-GC Radius relationship defined as

$$R_{e,gc} = R_p \left(\frac{M_*}{M_p}\right)^{\alpha} \left[\frac{1}{2}\left\{1 + \left(\frac{M_*}{M_p}\right)^{\delta}\right\}\right]^{(\beta-\alpha)/\delta}$$

(4.2)

Since we assume this distribution is spherical overall, we only require one profile and sample from this to produce random positions — again, ensuring that we randomly vary the quadrant that the points are sampled from.

To determine the model spiral distribution, we increase the radial extent of spirals identified within the images by 3 pixels for each host. Ideally, we would like to use a physical threshold for this dilation, but limits on image resolution for higher redshift sources do not allow for pc-scale image dilation. The threshold chosen has an average physical scale of $\sim 0.5\,\mathrm{kpc}$ This method works under the assumption that our previous determinations of which pixels are part of the spiral arms may not capture the lowest surface brightness extents of spiral arms where lower-mass stars may have drifted.

4.3.3.2 Comparisons to Models and Other Transients

Somewhat similar analyses have been done in the works of Aramyan et al. (2016) and Karapetyan (2022), however, these authors calculate distances of supernovae relative to arm brightness profiles — and their peaks — normalized to arm width. Here, we make use of measurements from Bartunov et al. (1994) which present measures of Type Ia and II supernova

distances (minimum distance to a spiral arm; $\widetilde{R}_{min}$) that are more similar to what we have done in this study.

The resulting CDFs show a clear distinction between the random and globular cluster models and the FRB distribution. This distinction is further supported by the results of the KS test which reject the null hypothesis that the globular cluster, random, and FRB samples are drawn from the same population. We are unable to reject the null hypothesis for the disk, spiral, and (Type Ia and core-collapse) supernovae distributions (Bartunov et al., 1994). However, the median of the FRB distribution does intersect the spherical GC distribution, the implications of which we discuss in more detail in §4.5.

4.4 Environment and Burst characteristics

As the number of ultra-precise (mas-scale) localizations of FRBs continues to grow, the ability to make robust connections between burst and local environment characteristics will grow in tandem. Here, we explore some of these possible connections with our sample of FRBs.

Many of the measurements we include here — such as $\Sigma_{\mathrm{M}*}$, $\mathrm{F_F}$, and $\widetilde{R}_{min}$ — are measured on kpc- or 10^2 pc-scales. This means that we are more sensitive to correlations with the effects that larger-scale fluctuations or properties may have on the burst properties than the most local effects.

We are particularly interested in questioning the possibility of a fundamental connection between FRBs and massive stars.

We look at the relationships between Faraday Rotation, Dispersion measure, fluence, and local measurements. If FRBs are indeed embedded in complex media as suggested by Pastor-Marazuela et al. (2025), we may expect to see imprints of this medium in relationships between local environment and burst characteristics. We have already seen that very high

rotation measures such as that for FRB 20121102 have been detected, and, along with other burst characteristics, point towards origins within a very complex magneto-ionic environment Michilli et al. (2018).

We looked for any such correlations between each of our burst characteristics and each of the local measures. We find one possible correlation of note which we discuss in §4.4.1. Otherwise, rotation measure, dispersion measure, and fluence show no significant correlations with the measurements we have taken in this study.

4.4.1 FRB Scattering

Current assumptions about the locations of scattering screens that produce broadening observed in FRBs place screens within the host, whether in the galaxy's ISM or in the immediate circum-burst environment — with some contribution from the Milky Way (Ocker et al., 2021). We assume that contributions due to intervening halos are negligible, as FRBs are unlikely to intersect the halos with a sufficiently low impact parameter for contributions to be non-negligible (Ocker et al., 2021; Pastor-Marazuela et al., 2025).

4.4.1.1 Scattering and Stellar Mass Surface Density

If scattering is indeed dominated by the host, we may expect to see some correlation between tau and local measures, such as Σ_{M*}, which can trace stellar mass. If, however, effects are dominated by pc- to AU-scale effects, we may not expect to see any such correlations. In Figure 4.4 we show the scattering time τ as a function of Σ_{M*} — specifically the expected tau at 1 GHz ($\tau_{1\,\mathrm{GHz}}$). Furthermore, since Σ_{M*} is a measure intrinsic to the host galaxy, we multiply the measured τ values by a factor of $(1+z)^3/3$ so that we can derive the intrinsic scattering time (which is used for comparison with Σ_{M*} and other local measures).

We find a positive correlation with a Pearson $r = 0.506$, however, the p-value ($p = 0.093$)

does not allow us to reject the null hypothesis that the correlation coefficient is zero. With a larger sample size, we can further constrain this relationship and produce results with greater statistical significance.

To rule out the possibility that galaxy-scale, supernova-driven turbulence is related to FRB scattering, we looked at the correlation between $\tau_{1\,GHz}$ and star-formation rates (current and over the last 100 Myr) and found no correlation. We also look at scattering as a function of $\widetilde{R}_{min}$ and find no correlation between the two.

4.5 Discussion

4.5.1 FRB Delay Times and Physical Locations

4.5.1.1 Binaries, Mergers, Supernovae, Oh My!

As noted by Sharma et al. (2024), the expected drift for a CC-SNe progenitor with a typical stellar velocity of $10\,\mathrm{km\,s^{-1}}$ and a lifetime of 75 Myr, is approximately 750 pc. If we consider, as Sharma et al. (2024) did, the case of a high-metallicity system where a massive-star-binary merger is more likely — and the delay from birth to SNe can be prolonged — you may expect a drift of $0.5 - 2$ kpc. Our measures of $\widetilde{R}_{min}$ span this range, with a median distance of 0.917 kpc where the median lifetime could be approximated to ~ 90 Myr.

However, the recent work by Horowicz and Margalit (2025) has effectively ruled out the metallicity-dependence that underpins this particular merger-remnant theory. Zapartas et al. (2019) discuss the role of metallicity in producing a Type II SN from a main sequence + main sequence merger scenario. In this particular case, there is a metallicity dependence where higher-metallicity stars are more likely to transfer mass to a companion star through Roche Lobe Overflow (RLOF).

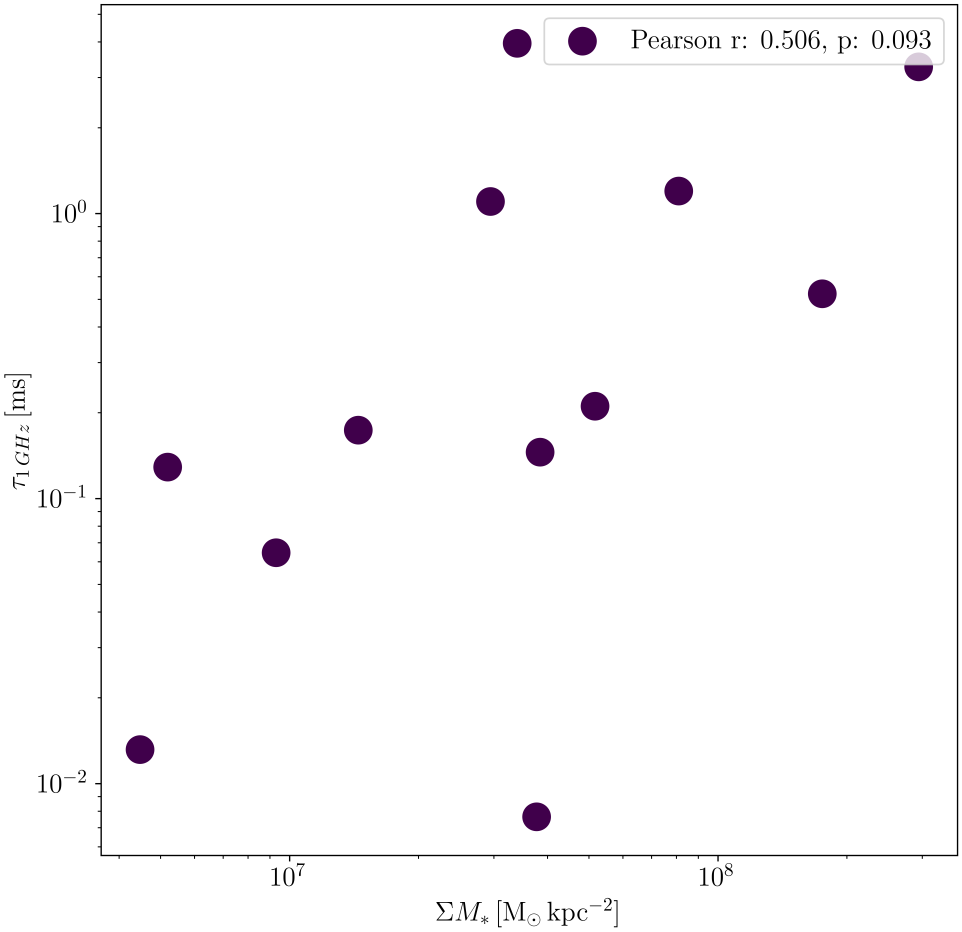

Figure 4.4: Scatter plot of scattering time τ as a function of Σ_{M*}. We see a slight positive correlation with a Pearson $r = 0.506$. However, the correlation is not statistically significant with a p-value of 0.093, where we require a p-value ≤ 0.05 to reject the null hypothesis.

There are other binary merger scenarios that have a very weak metallicity dependence, such as main sequence + post-main sequence mergers that can also lead to type II supernovae (at a rate of 14%; Zapartas et al. (2019)). A similar discussion of the effects of binary interaction on supernovae and their delay times is found by Zapartas et al. (2017). Here, they explore how binary interactions can produce "late" CC-SNe or "prompt" Ia-SNe. They find an extended distribution of delay times (post-starbust) that matches the range of implied delayed times found by the calculation of $\widetilde{R}_{min}$ $(50 - 200$ Myr). The binary systems they discuss include many intermediate-mass stars, where the range of masses of the primary star is 4-10 $M_{\odot}$, and the mass range for the secondary is 2-8 $M_{\odot}$. Alone, the stars may not meet the mass criteria for a prompt CC-SNe, but through mass transfer these thresholds can be met. One scenario outlined by Zapartas et al. (2017) is the reverse merger of a Carbon-Oxygen White Dwarf (COWD) and a post-main sequence star that is crossing the Hertzsprung Gap (core-hydrogen burning has ceased). Such a merger (or common-envelope phase) could produce either a Core-collapse explosion of the COWD engulfed in its secondary companion, or a thermonuclear explosion that occurs inside of a hydrogen envelope. The result of such an explosion could be a neutron star. Matsumoto et al. (2025) and Dessart (2018) show that a magnetar could be produced by hydrogen-rich (Type II) supernova and subsequently power its luminous, and long-lasting light curves.

The statistical analysis of FRB host galaxy properties presented by Horowicz and Margalit (2025), shows that FRBs are inconsistent with tracing star-formation or stellar mass, alone. Instead, they seem to trace a linear combination of stellar mass and star formation — similar to what is seen for the hosts of Type 1a supernovae. As we have seen at least three FRBs localized to quiescent or elliptical galaxies (e.g. Eftekhari et al., 2025; Gordon et al., 2023), some fraction of FRBs must originate in hosts that are not actively forming stars. The study by Horowicz and Margalit (2025) show that mixed multi-variate models weighted by star-formation and stellar mass, produced distributions that were indistinguishable from FRB uni-variate

distributions of stellar mass and star formation rate. Through the scenarios outlined by Zapartas et al. (2017) we can say that massive stars are not a requirement for various types of supernovae that could potentially produce a neutron star. With this possibility of including intermediate mass stars and low-mass stars (delayed Type II-SNe resulting from a merger, Accretion Induced Collapse, or WD-WD mergers) perhaps FRB progenitors could indeed trace both stellar mass and star-formation in overall host galaxy properties.

As a final point, we see that the FRBs in this sample trace the offsets and light locations of Ia-SNe occurring in spiral galaxies (as we will discuss further in § 4.5.1.3.Type Ia supernovae are 10 times more likely to occur in a star-forming galaxy than a passive one (Sullivan et al., 2006), and while the number of FRBs found in passive and elliptical galaxies is growing, it remains a rarity. Referring again to the analysis by **?**, the authors find that Ia-SNe occur in both arm and inter-arm regions, and this is mirrored in the range of $\widetilde{R}_{min}$ that we measure here and analysis in Gordon et. al, in prep (see more in §4.5.1.2.)

4.5.1.2 Overall Spatial Distributions: Do FRBs Care About the Disk?

Gordon et. al, in prep, compares the spatial positions of FRBs to models including GC ellipsoidal, GC spherical, residual, and smooth distributions. They find that FRBs, on average, prefer the smooth distributions of light in their hosts. In some cases, they find strong preferences for the residual or GC Spherical models as well, but to a much lower degree. The associations to the residual structure is, however, dependent on localization precision. They also find that the host-normalized offset distributions (with only a few more FRBs) could be used to differentiate GC and disk FRBs.

As we calculate the minimum distances between FRBs and spiral arms, we also need to characterize the placement (or inclination) of the bursts relative to the plane of the disk. To do this, we compute the angle between the galaxy's semi-major axis vector and the FRB offset

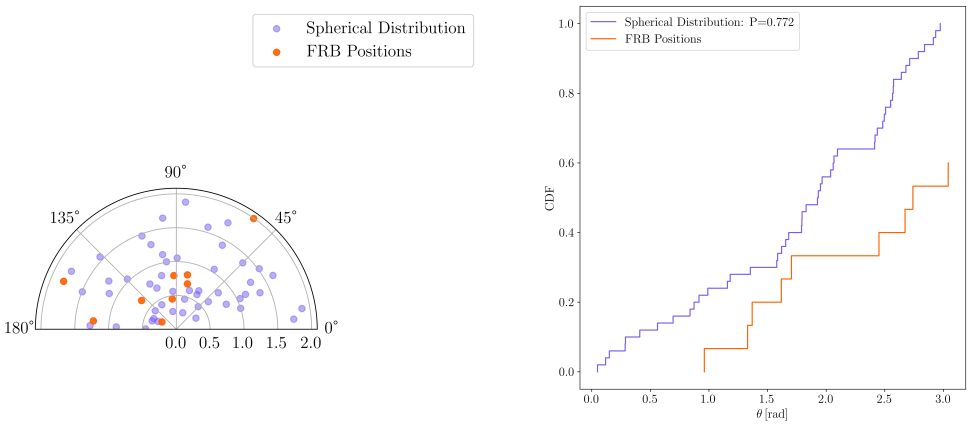

Figure 4.5: *Left:* Angular and radial distribution of FRB positions (orange) relative to the semi-major axis of the host galaxy. This shows the angle between the FRB offset vector and the semi-major axis. Angles towards 90 mean the offset is elevated well above the disk, where angles near 0 or 180 mean that the FRB lies within the plane of the disk. The radial direction is the ratio r/a. Many of FRBs are at offsets within $1.5a$. A spherical distribution of points is shown in purple. *Right:* The cumulative distributions of both the FRB and Spherical distributions. A KS-test cannot reject the null hypothesis that they are drawn from the same underlying population. We limit this analysis to hosts with $i > 40$.

vector with

$$cos\theta = \frac{\vec{a} \cdot \vec{r}}{|a||r|} \tag{4.3}$$

where a is the semi-major axis and r is the FRB offset vector. We also limit this analysis to FRB hosts with inclination angles $i > 50$.

We find that the cumulative FRB and spherical distributions cannot be distinguished (with $P_{KS} > 0.05$). Figure 4.5 shows the elevations of the FRBs and the ratio of r/a. Where

a disk-concentrated distributions might exist around $\theta = 0$, the FRB and spherical points are randomly distributed over the first two quadrants. To randomly generate the spherical distribution, we set flat priors (uniform distributions) for both θ and r/a. The limits of these distributions were set by the minimum and maximum values of the FRB distribution. The difference in radial distributions should be noted, as the FRBs seem to prefer, in general, $r/a < 1.5$. However, upon further inspection of the images, we found that the angle between a and r is not always indicative of the true azimuthal angle between the disk and the FRB position. For inclinations between 50-60, the FRB position is consistently projected onto the disk even with $\theta \approx 90$. Further analysis should also include a mock sample of positions from the host disks in order to make a better comparison.

4.5.1.3 Light and Mass Concentration

The median fractional flux of the FRB locations is 0.42, with the median of the Type Ia distribution also falling around 0.4. The Type II distribution, in contrast, falls around 0.6. These differences in the brightness of Type Ia and Type II supernovae are sensible considering the difference in progenitor masses and lifetimes. According to the results of Aramyan et al. (2016), the spatial distribution of Type Ia supernovae spans larger distances from the brightness peak and star-forming shock fronts of the natal spiral than the distribution of CC SNe which have a narrower distribution around this brightness peak. The fractional flux values for the supernovae classes are reasonable in this context.

FRBs not appear in the brightest regions of their hosts, nor do they have offsets from spiral structure < 0.5 kpc. It should also be reiterated that their stellar mass surface densities are estimated to be lower than a star-forming region such as Orion A with a majority falling below the mean stellar mass surface density for the Milky Way. Deeper investigation reveals that more than half of the sample shows stellar mass surface densities that are depressed relative

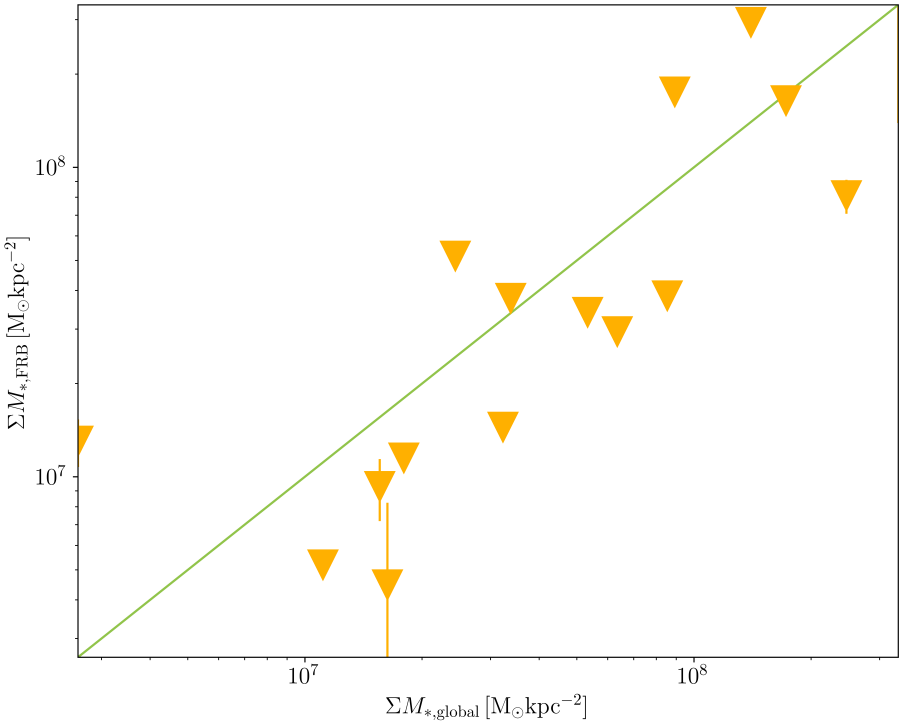

Figure 4.6: Global vs Local $\Sigma_{\mathrm{M}*}$for the FRB locations. The 1:1 line (light green) shows where the global and local values are equal to one another. Points above this line show elevated local values, and points below this line show depressed local values — relative to the average host value. Many of the FRBs in this sample show local $\Sigma_{\mathrm{M}*}$lower than the average global value. We show 10σ error bars, but in most cases the error bars are smaller than the points.

to their global values (Figure 4.6). But some of the

All of the measures of light at the FRB location point towards an FRB source that experiences a sizable drift from its initial location. While FRBs may have a slight preference for star-forming galaxies, it is unclear if they trace star-formation within their host galaxies. A larger sample of NUV images would be incredibly illuminating in this regard.

4.5.2 Burst Characteristics

4.5.2.1 Interpretations of Scattering and Local Measures

Scattering shows a possible (though, weak) correlation with $\Sigma_{\mathrm{M}*}$. In Glowacki et. al, in prep, the authors find strong correlations between mass-weighted age, gas phase metallicity, and scattering.

Scattering is seen to have positive correlations with the mass-weighted ages and gas-phase metallicities of the hosts. The slight correlation with $\Sigma_{\mathrm{M}*}$that we find here may point to a dependence of scattering on the metallicity of the gas surrounding the FRB source, with denser regions containing more enriched materials deposited by massive star deaths. This can also lead to the enrichment of stars pre-supernova, as the stars accrete material from the ISM. Perhaps this enrichment has an effect on the expansion of a supernova remnant into the surrounding material in the subsequent shock and ISM interactions.

4.5.2.2 Fluence and $\widetilde{R}_{min}$

Because of the connection between distance to nearest spiral arm and fade time of Ia's found by **?**, we look at the relationship between fluence and $\widetilde{R}_{min}$ among this sample of FRBs. The positive correlation between fade time and distance to the spiral arm, pointed authors towards an explanation that implicated sub-Chandrasekhar mass explosions which match delay

times that place progenitors in the inter-arm regions. They also make this connection through the fast delay times that inter-arm explosions exhibit, suggesting an older progenitor in these regions. We, too, look for a connection between the energetics of a FRB and its location relative star-formation, but we find none.

4.5.3 FRBs in complex media

Pastor-Marazuela et al. (2025) put forward the idea that FRBs mirror characteristics of young neutron stars embedded in complex media, as they show high scattering timescales and rotation measures — implying a turbulent, magnetized circum-burst environment. This complex media could be a dense star-forming region or more local complex media such as a supernova remnant, and signatures of this show up through polarization effects dispersion measures, and and other bust characteristics. In this study, we do not find that FRBs are occurring in regions with high stellar mass density, as we find significant offsets of up to 3 kpc from spiral arms in some cases. Since we do not use NUV images to directly probe their relationship to recent star-formation, we are unable to more directly address this aspect of the assertions made by Pastor-Marazuela et al. (2025). If, however, FRBs are primarily the result of binary interactions, the complexity of the surrounding material may reflect this. We see studies such as Piro and Gaensler (2018) and Margalit and Metzger (2018) that account FRB emission and properties with the properties of the immediate, circum-burst environment. Essentially, "complex media" does not have to include star-forming regions and we see that reflected here.

4.6 Conclusions

We find that FRB locations may tend to favor that of Type Ia supernovae, supporting the possible association made by Horowicz and Margalit (2025). This, however, does not preclude

the possibility that FRBs also come from CC-SNe, as we have seen that binary progenitor pathways could result in the delay times that we have seen here. We also look at the properties of light and density of stellar mass at the FRB positions and find that they do not occur in the brightest regions of their galaxies, nor do the majority occur in regions of elevated stellar mass surface density. With respect to burst characteristics, we find no strong correlations between burst characteristics and local measures, but a possible correlation between scattering and stellar mass surface density is intriguing. Greater numbers of studies with burst characteristics and high-resolution imaging will prove to be very informative in understanding progenitors, their environments, and even disentangling line-of-sight contributions to scattering, DM, and RM.

Chapter 5

Fast Radio Burst Rotation Measures as Probes of Extragalactic Magnetic Fields

As stated, Fast Radio Bursts (FRBs) are milli-second duration pulses of radio emission, arising predominantly from extragalactic sources (e.g. Cordes and Chatterjee, 2019). The first burst discovered, subsequently named the Lorimer burst (Lorimer et al., 2007), revealed a new radio transient class with unprecedented power to probe cosmological questions of matter distribution, universal expansion, and (inter-)galactic magnetism due to their dispersion and rotation measures (DMs, RMs; e.g. Gaensler, 2009; Macquart et al., 2010; Akahori and Ryu, 2011; Macquart et al., 2015; Akahori et al., 2016). Since the discovery of FRBs, their dispersion measure has already been used to search for answers to long standing questions. Works such as Macquart et al. (2020) and Simha et al. (2020) offer a nearly complete baryon census—finding baryons where they were once nearly impossible to detect. Galactic halos and the intergalactic medium (IGM) are now being backlit by the flashlights that are FRBs, illuminating the once "missing" matter.

FRBs also have potential to probe another influential property of the universe – magnetic

fields (e.g. Piro and Gaensler, 2018; Hackstein et al., 2019). Many questions such as the origins of magnetic fields, their effects on the evolution of galaxies, and the process of their amplification over cosmological time have been explored extensively with theoretical treatments (e.g. Springel, 2010; Pakmor et al., 2011; Rodrigues et al., 2018). Observational constraints, however, are currently scant and are critically needed to constrain the physical processes at work.

There are a number of ways to measure the effects of magnetism in galactic and extragalactic systems, and each method is sensitive to a different magnetic field component (see Beck (2015) for a list of magnetic field components and observational methods). The Zeeman effect can be observed in the emission line spectra of galaxies, indicating a regular field along the line of sight. One can also measure the polarized intensity and linear polarization angle of QSOs and other persistent radio sources, or evaluate signatures from synchrotron radiation which are associated with the magnetic field component that is perpendicular to the line of sight.

In this study we use the Faraday rotation measures (RMs) —which quantify the effect of magnetized plasma on linearly polarized radiation— of FRBs to probe the component of the magnetic field which is parallel to the line of sight ($B_{\parallel}$). This measure can elucidate the magneto-ionic environment surrounding the FRB. As the signal also interacts with the inter-stellar and circum-galactic media of the FRB host, we can make measurements of the fields in these broader regions as well.

Constraining these field components helps determine what processes are implicated in the production and amplification of magnetic fields—whether tied to the progenitor object itself and its immediate environment (e.g. Piro and Gaensler, 2018) or evolution on galactic and cosmic scales (e.g. Hackstein et al., 2019). Comparison of the observed quantities to those predicted by simulations, can be an invaluable test of our understanding of the relationship between magnetic fields and galaxy evolution (e.g. Rodrigues et al., 2018). We can also test FRB progenitor models and how burst properties would be affected.

In this paper we make use of the Auriga simulations (Grand et al., 2017), a set of high resolution cosmological zoom-in simulations of Milky Way-like galaxies that reproduce many important properties of their observed counterparts. In particular they include a self-consistent model of magnetic field amplification and evolution over cosmic time that produces realistic magnetic field strengths at $z = 0$ (Pakmor et al., 2017, 2018, 2020). We use the simulations to connect the FRB observations to conditions in their local and global environments of their host galaxies.

We also explore the possible connections between the RMs of a set of FRBs and local characteristics determined by, e.g., Heintz et al. (2020), Bhandari et al. (2020b), and Mannings et al. (2021). These works demonstrate that FRBs originate primarily in star-forming galaxies with stellar masses ranging from $M_* \sim 10^8 - 10^{11} M_\odot$. These data also reveal the location of the FRBs within their hosts and constrain local measures such as the star formation density which may correlate with magnetized plasma.

This paper is organized as follows. We describe rotation measure in detail in section 5.0.1. In section 5.1, we outline the selection criteria for our sample (§5.1.1), provide a description of rotation measure data (§5.1.2), detail the host observations for each burst (§5.1.3), and describe host properties (§5.1.4). In section 5.2, we discuss the observational analysis and results. We begin by detailing the methods for estimating host contributions to RM and DM ($\mathrm{RM_{host}}$ and $\mathrm{DM_{host}}$), including the extragalactic contribution to the rotation measure(§5.2.1), the Milky Way contribution to RM (§5.2.1.1), the correlation between rotation measure and redshift (§ 5.2.1.2), and estimates of $\mathrm{DM_{host}}$(§5.2.2). We then investigate correlations between and host galaxy characteristics in §5.2.3, and, in Section 5.2.4, we make estimates of magnetic field magnitudes of the galaxies hosting the FRBs. We then discuss the modeling framework for and results for a magneto-hydrodynamic model of Milky Way-like galaxies (§5.3 and §5.3.2) with which we simulate rotation and dispersion measure measurements and compare against observed values

(§5.3.3 and §5.3.4). We finish with a final summary and discussion of implications in §5.4.

5.0.1 Polarization and Faraday Effect

If the oscillations of an electromagnetic field have a preferred orientation, then this radiation is polarized. The polarization of an electromagnetic (EM) wave is determined by the orientation of the electric field component. In general, the polarization of an EM wave is elliptical, i.e. the electric field vector traces an ellipse perpendicular to the propagation direction during transit. Elliptically polarized light can be expressed as a linear combination of two orthogonal linear polarization states or two circular polarization states (Griffiths, 2013). One requires only three independent parameters to describe the polarization state of an EM wave.

Polarization of radio waves, however, are most often described using the Stokes I, Q, U, and V parameters, where I refers to the total intensity, Q and U linear polarization, and V circular polarization. These parameters can be combined to represent polarization in the form of the Stokes vector

$$\vec{S} = \begin{pmatrix} I \\ Q \\ U \\ V \end{pmatrix} \tag{5.1}$$

Estimating Q, U, and V from raw data depends on the specific configuration of the instrument used to detect and measure the polarization signals. As we are including FRBs from multiple experiments across multiple telescopes, descriptions of their methods and parameter formulations can be found in their respective studies (Michilli et al., 2018; Day et al., 2020; Mckinven et al., 2021; Kumar et al., 2022).

The linear polarization angle ψ is expressed as

$$\psi = \frac{1}{2} \arctan \frac{U}{Q} \quad . \tag{5.2}$$

ψ is, in general, a function of frequency and time, $\psi(\nu, t)$, and for FRBs it has been observed to evolve over the duration of the burst (e.g. Day et al., 2020; Michilli et al., 2018).

As monochromatic light propagates through plasma which has a magnetic field component along the direction of propagation, its linear polarization angle is rotated. The degree of rotation is proportional to the inverse square of the frequency and the proportionality constant depends on the properties of the intervening magnetized medium. While the net rotation at any wavelength or frequency cannot be determined, for a multi-frequency radio signal like an FRB, the rotation measure (RM) encodes the properties of the intervening medium and is measured from the variation of the linear polarization angle with wavelength squared:

$$\mathrm{RM} = \frac{d\psi}{d\lambda^2} \quad . \tag{5.3}$$

For a pulse of radiation emitted at redshift z that traverses to Earth, we may express

$$\mathrm{RM} = C_R \int_z^0 \frac{n_e(z) B_\parallel(z)}{(1+z)^2} \frac{dl(z)}{dz} dz \, \mathrm{rad\,m^{-2}} \tag{5.4}$$

where C_R is a set of physical constants including the inverse square of the electron mass m_e^{-2}, electron charge cubed e^3, and the inverse of the speed of light to the fourth power c^{-4}. n_e is the electron density, $\mathrm{B}_\parallel$ is the magnitude of the line of sight magnetic field, and the integral is over the length of the sightline dl with n_e $\mathrm{B}_\parallel$ and dl as functions of z. RM can be positive or negative depending on the direction of the magnetic field component. In other words, RM is the average parallel magnetic field strength along the line of sight weighted by n_e. For FRBs, this includes contributions from the Milky Way, cosmic magnetic fields and the magnetic fields within its host galaxy.

However, it is assumed the field undergoes numerous reversals along the line of sight that minimize the IGM contribution to the RM relative to the host and Milky Way contributions. Our assumptions about the structure of the magnetic field means that our interpretations of RM and derived quantities become model dependent. Nonetheless, there exist measurements of RM in cosmic filaments (RM_f) such as those presented by Carretti et al. (2022), which provides estimates around $\mathrm{RM_f} = 0.71 \pm 0.07\,\mathrm{rad\,m^{-2}}$. They then infer a magnetic field magnitude in the filaments to be $B_f \approx 32$nG. This value being a tenth of an RM unit (and assuming the value in cosmic voids is even lower due to a lack of ionized material in these regions) motivates an expectation for minimal RM contribution from the IGM. Specific to FRBs, upper limits on the CGM and IGM contributions to FRB Rotation measures, can be found in the publications by Ravi et al. (2016); Prochaska et al. (2019a) and O'Sullivan et al. (2020).

Maps of the Milky Way's magnetic field and Faraday rotation have been developed using measurements of extragalactic polarized sources, as discussed in Section 5.2.1.1. Once this contribution is subtracted, we can isolate the other components in an effort to better understand magnetic field generation and amplification in the universe, as well as the magneto-ionic environments of FRB progenitors.

5.1 FRB Data and Sample Selection

5.1.1 Selection Criteria

Presently, there are over 600 FRBs in the published literature and of these ~ 20 with published RM values. These form the parent sample from which we construct a subset for our analysis. Our scientific foci are to:

- Study correlations between local host properties and the inferred host contribution to the

RM.

- Estimate magnetic fields in FRB hosts.
- Make comparisons to cosmological zoom-in simulations that study the relationship between galaxy evolution and magnetic fields.

These scientific goals helped define the following selection criteria that each FRB must satisfy:

1. A precisely measured RM value.
2. A kpc-scale FRB localization precision.
3. A high probability association to a host galaxy.
4. A spectroscopic redshift measurement for the host galaxy.
5. Host galaxy imaging and subsequent derived host properties. such as stellar mass, star-formation rate, etc.
6. Considered and added to the sample by January 2022.

The first criterion is fundamental to the analysis. The second addresses the fact that RMs are sensitive to turbulent small-scale magnetic fields as well as large-scale ordered fields. Requiring kpc-scale localizations allows an exploration of correlations between local measures such as the star-formation rate surface density and RM. In the following analysis, we require the net localization uncertainty (statistical and systematic error) be less than 5 kpc at the redshift of the host galaxy.

Regarding the third criterion, we adopt the Probabilistic Association of Transients to Hosts (PATH; Aggarwal et al., 2021) formalism and demand that the FRB posterior probability

$P(O|x)$ exceeds 95%. In general, this criterion is redundant with the second as a highly precise localization will generally yield a secure association provided sufficiently deep imaging (Eftekhari et al., 2020). The fifth and sixth criteria allow us to search for correlations between the host galaxy properties and RM.

After applying these selection criteria to the full set of published sources, we recover 9 FRBs satisfying the full set. These are listed in Table **??**.

5.1.2 Rotation Measures and Other Burst Properties

The 9 FRBs defining our sample are drawn primarily from two FRB surveys. The first is the Commensal Real-time ASKAP Fast Transients (CRAFT) survey using the Australian Square Kilometre Array Pathfinder (ASKAP) telescope Macquart et al. (2010). The CRAFT collaboration discovered and observed six of the FRB events presented in this paper, on the date in accordance with the TNS name of the event: 20180924B (Bannister et al., 2019), 20190102C, 20190608B, 20190711A (Day et al., 2020), 20191001A (Bhandari et al., 2020a), and 20201124A (Kumar et al., 2022). 20190711A and 20201124A are repeating bursts whose rotation measure may change with time; the quoted rotation measures are taken from the publications in which these data are presented which are the first detected burst and an average over all detected bursts, respectively.

Two of the bursts in this sample were detected and characterized by the Canadian Hydrogen Intensity Mapping Experiment (CHIME)/FRB Experiment (FRBs 20180916B, 20200120E). The rotation measure for FRB 20180916B—located in a nearby spiral galaxy (Tendulkar et al., 2020)—is presented by the CHIME collaboration with 7 other new (at the time) repeating FRBs (CHIME/FRB Collaboration et al., 2019). The RM for this burst was derived from baseband data collected on FRB 20181226A, a subsequent repetition of FRB 20180916B. FRB 20200120E is localized to a Globular Cluster located in the halo of M81

and is presented by Bhardwaj et al. (2021).

Lastly, we include the source commonly referred to as R1: FRB20121102A. The rotation measure for FRB 20121102A was first presented by Michilli et al. (2018), where they detailed the extreme magneto-ionic environment in which the burst progenitor must be embedded, in order to produce such a high rotation measure, $\mathrm{RM_{FRB}} \sim 10^5\,\mathrm{rad\,m^{-2}}$. Since this is a repeating burst we take the average quoted by Michilli et al. (2018) as our value.

Five out of the 9 FRBs in this sample repeat, leaving four apparently non-repeating bursts. The sample has a median $|\mathrm{RM_{FRB}}| = 56\,\mathrm{rad\,m^{-2}}$ with a range $9\,\mathrm{rad\,m^{-2}} < |\mathrm{RM_{FRB}}| < 10^5\,\mathrm{rad\,m^{-2}}$ (see Table **??**).

Repeating bursts can show variability and evolution over the individual burst envelope and with time over subsequent burst repetitions (e.g. Michilli et al., 2018). All of the repeating bursts in the sample show at least slight variability in their RMs from burst to burst. These variations are insignificant in comparison to the FRB source to FRB source variation in RM and do not impact any of the analysis presented here.

5.1.3 Host Observations

Nearly all of the observations of the host galaxies for our RM sample have been published previously. Here, we briefly review the primary datasets.

Regarding imaging, where available we have leveraged high-spatial resolution data obtained with the Hubble Space Telescope (*HST*). Six of the hosts in the sample were observed by *HST* and its Wide-field Camera 3 (WFC3) in UVIS and IR images (F300X and F160W filters, respectively) taken as part of GO programs 15878 (PI: Prochaska) and 16080 (PI: Mannings).

These programs targeted galaxies for which FRB events have been detected and localized by the CRAFT survey. These images were previously published by Chittidi et al. (2021) and Mannings et al. (2021). Information for FRBs 20180924B, 20190102C, 20190608B, 20190711A,

Table 5.1: FRB is the TNS name of the fast radio burst; those with a dagger are known to repeat. $\mathrm{RA_{FRB}}$,$\mathrm{Dec_{FRB}}$ are the coordinates of the FRB. $\mathrm{RA_{Host}}$,$\mathrm{Dec_{Host}}$ are the coordinates of the host galaxy. M_* is the stellar mass of the host galaxy. SFR is the star formation rate of the host galaxy, with typical uncertainty of 30% (systematic). r_e is the effective radius of the host galaxy.

FRB	$\mathrm{RA_{FRB}}$	$\mathrm{Dec_{FRB}}$	$\mathrm{RA_{Host}}$	$\mathrm{Dec_{Host}}$	M_*	(SFR)	r_e
					$(10^9 M_\odot)$	$(M_\odot \mathrm{yr}^{-1})$	(kpc)
20121102A†	82.9946	33.1479	82.9945	33.1479	0.143 ± 0.066	0.13	2.05 ± 0.11
20180916B†	29.5031	65.7168	29.5012	65.7147	2.15 ± 0.33	0.06	6.009 ± 0.012
20180924B	326.1052	−40.9000	326.1052	−40.9002	13.2 ± 5.1	0.88	2.82 ± 0.53
20190102C	322.4157	−79.4757	322.4149	−79.4757	4.7 ± 5.4	0.86	5.01 ± 0.15
20190608B	334.0199	−7.8982	334.0204	−7.8989	11.6 ± 2.8	0.69	7.373 ± 0.059
20190711A†	329.4192	−80.3580	329.4192	−80.3581	0.81 ± 0.29	0.42	2.48 ± 0.13
20191001A	323.3513	−54.7477	323.3518	−54.7485	46 ± 19	8.07	5.550 ± 0.029
20200120E†	149.4778	68.8189	148.8882	69.0653	72 ± 17	0.89	12.50 ± 0.40
20201124A†	77.0146	26.0607	77.0145	26.0605	2.80 ± 0.50	2.10	1.988 ± 0.037

and 20191001A was drawn from this dataset.

We also include *HST* images from GO program 14890 (PI: Tendulkar) which observed the host of FRB 20121102A (Bassa et al., 2017). These observations include images taken in the F110W and F160W IR filters (equivalent to J and H bands, respectively), and a narrow-band H-α image with the F763M filter. Detailed descriptions of image processing and reduction can be found in the publications from Bassa et al. (2017) and Mannings et al. (2021).

The high spatial-resolution imaging is complemented by multi-band, ground-based images from public surveys and directed follow-up campaigns. We refer the reader to Heintz et al. (2020) and Bhandari et al. (2020b,a, 2022) for details and note the data are all taken from the FRB repository on GitHub (Prochaska et al., 2019).

5.1.4 Host Properties

Central to our study is an exploration of the properties of the galaxies hosting the FRBs, both global and local measures. We use the quantities derived from previous studies throughout this work: star-formation rates (global and local to the FRB, SFR and $\Sigma_{\rm SFR}$), effective radii (r_e), stellar mass (global M_* and local $\Sigma_{\rm M*}$ to the FRB), and offsets. These are tabulated in Tables **??** (local properties) and 5.1 (global galaxy properties).

Figure 5.1 shows the locations of the FRBs within their host galaxies relative to the host galaxy centroid and in units of r_e. We have de-projected the offsets along the major and minor axes using fits to each host with the `GALFIT` (Peng et al., 2010) software package. Most of which are reported by Mannings et al. (2021), with the remaining two fits being presented here (FRBs 20200120E and 20201124A).

We observe that most of the bursts are located within $\approx 1.5r_e$ from the centers of their hosts, with one burst residing further out in its host's disk at $\approx 3r_e$. Furthermore, Mannings et al. (2021) characterizes the FRB locations in that sample as occurring at moderate offsets on

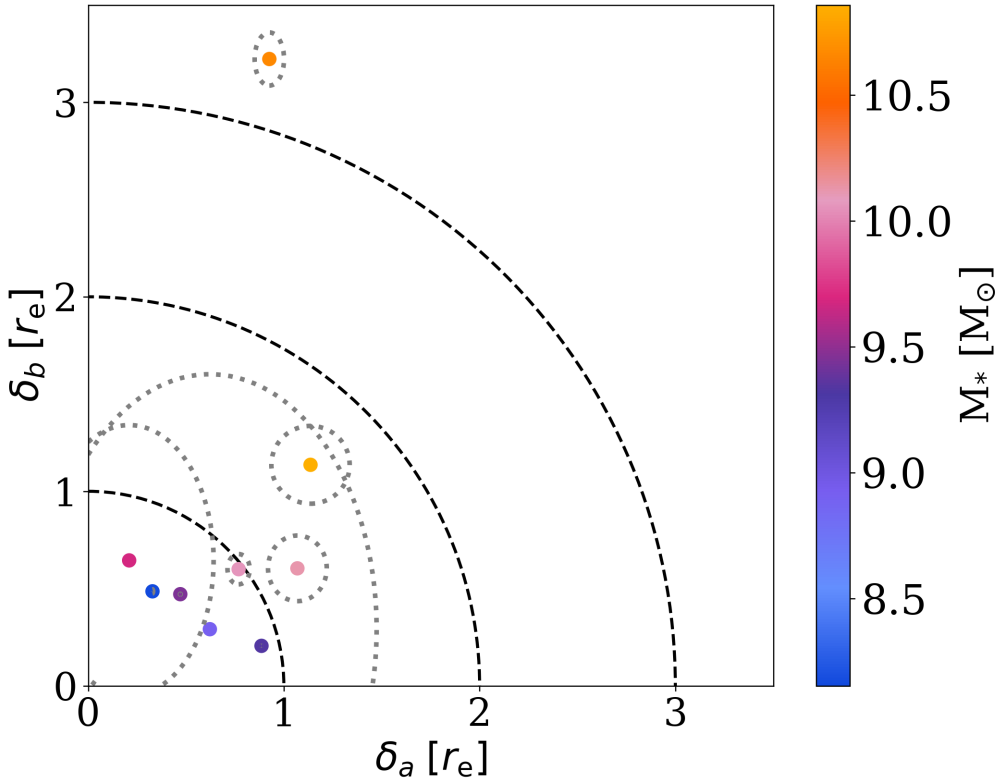

Figure 5.1: Locations of the FRB sample relative to their host galaxy centroids along the major (δ_a) and minor (δ_b) axes in units of r_e, defined by the half-light radius determined by GALFIT. The gray dotted ellipses around each of the points show the FRB localization error relative to the size of the host (several are smaller than the symbols). In the case of FRB 20190711A, the FRB localization is almost 2 times the effective radius of the host, resulting in a fairly large ellipse around the central point. FRB 20191001A is highly offset along the minor axis ($\delta b \approx 3$), but less-so along the major axis ($\delta a \approx 1$). See images from Mannings et al. (2021). The points cluster at $\delta_a, \delta_b < 1.5 r_e$. Therefore, the bursts are predominantly within the inner disks of the galaxies but rarely (if ever) from the nucleus itself (i.e. $<< r_e$).

or near spiral arm structure. Bhardwaj et al. (2021) shows that FRB 20201001E likely originated in a globular cluster in the outskirts of M81. In contrast, FRB 20121102A occurs very near a central star-forming region in its host. Therefore, as regards the ISM contribution to the RM, one expects variation as the bursts occur in relatively diverse environments although the majority are located on or near spiral structure.

We also characterize the host galaxies in the sample according to their overall properties. In Figure 5.2, we compare the global properties of the host galaxies in the sample against measurements of field galaxies at similar redshift. In the bottom panel, we show a color-magnitude diagram where hosts in the "Blue" region are early-type galaxies with young stellar populations and active star-formation, while those in the "Red" region are late-type hosts with very low star-formation and older stellar populations. The majority of these FRB hosts are star-forming and lie either in the so-called blue-cloud of galaxies or the green valley, as supported by what is shown in the upper panel (the star-formation rate vs stellar mass diagram) where most of the hosts reside in the "star-forming" region of the plot. The two notable exceptions are FRB 20200120E and FRB 20180916B which have hosts with non-zero SFR but lie below the SFR main-sequence, The figure indicates that the galaxies studied here have properties typical of a $z \sim 0.2$ population with a preference for star-forming and more luminous/massive galaxies. For the full parent population of FRB host galaxies, however, Safarzadeh et al. (2020) demonstrated that the hosts are less massive (and have lower SFR) than a sample weighted by SFR. The points are colored by the extra-galactic RM ($\mathrm{RM_{EG}}$; see eq.5.5), but there is no apparent correlation between the host properties and $\mathrm{RM_{EG}}$.

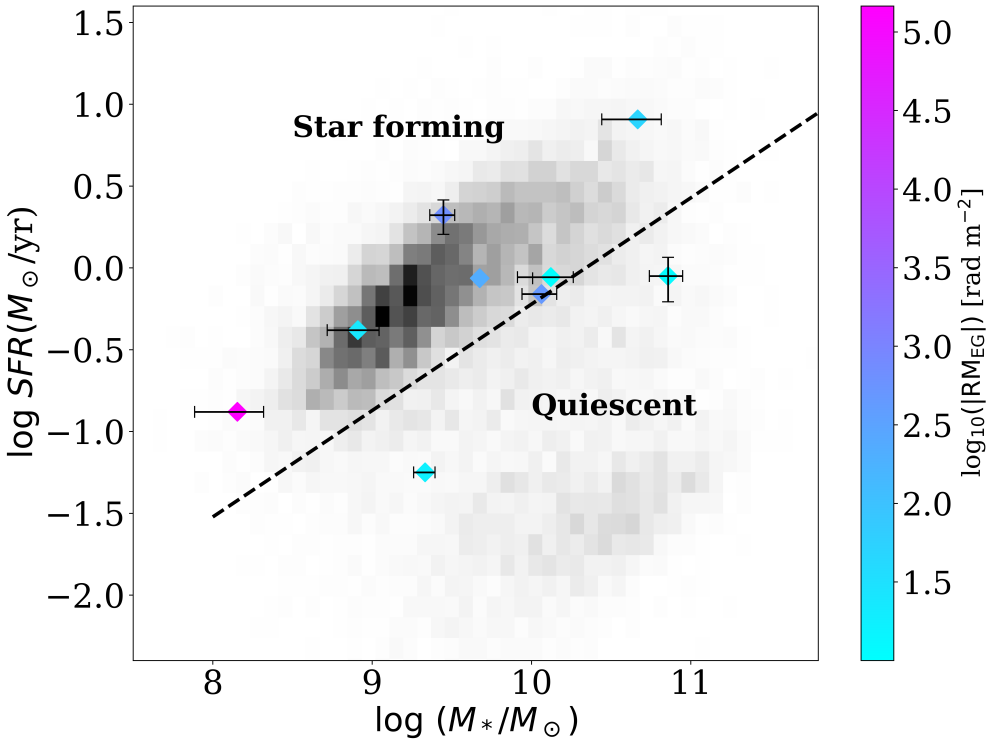

Figure 5.2: Diamond points (colored by $\log_{10}|\mathrm{RM_{EG}}|$; the RM component excluding Milky Way contribution; see § 5.2.1.1) present the global measures of stellar mass (M_*) and star-formation rate (SFR) for the host galaxies of our RM sample. The dashed line divides quiescent and star-forming hosts, and the 2D histogram describes the distribution for field galaxies from the PRIMUS survey (Moustakas et al., 2013). The majority of hosts lie in the star-forming region of the diagram with two in the quiescent region.

5.2 Observational Analysis and Results

In this section we analyze the RM measurements to search for correlations with the host galaxy properties and to estimate the underlying magnetic fields within the hosts. We begin by introducing approaches to isolate the RM and DM contributions from the host.

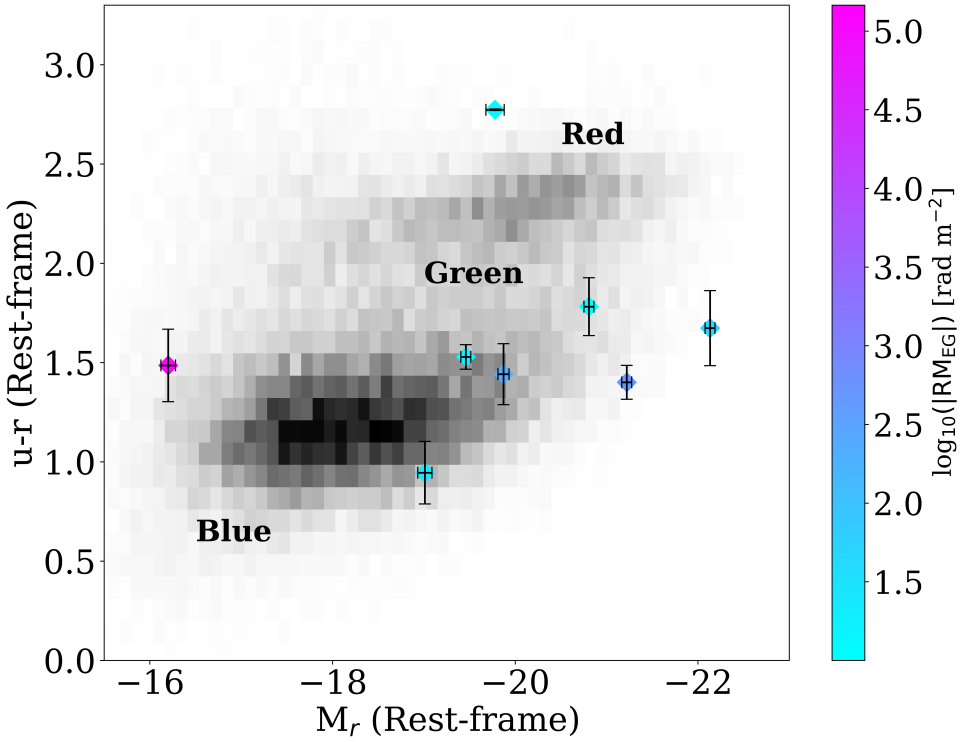

Figure 5.3: Color-magnitude diagram with points and histogram as above. The labels "Blue", "Green", and "Red" specify in turn: blue galaxies thought to be currently star-forming with younger stellar populations, green hosts transitioning out of star-formation, and "red and dead" galaxies where star-formation has ceased and older stellar populations dominate the host. The majority of our sample populate the blue cloud or green valley indicative of moderate star-formation.

The host and burst characteristics for FRB 20121102A are anomalous in comparison to the rest of the sample, as the host is a star-forming dwarf with a persistent radio source, and the burst's $\mathrm{RM_{FRB}}$ is orders of magnitude higher than other bursts in this sample. Much attention has been given to FRB 20121102A with respect to its high $\mathrm{RM_{FRB}}$, in an attempt to determine what connection this value has to possible progenitor channels and local magnetic field properties.

It should be noted that the $\mathrm{RM_{FRB}}$ of 20121102A is not completely unique with the detection of FRB 20190520B (Zhao and Wang, 2021; Niu et al., 2022) whose $\mathrm{DM_{FRB}}$ and $\mathrm{RM_{FRB}}$ are both much higher than what has been observed with other bursts. The $\mathrm{RM_{FRB}}$ varies substantially, but reaches a maximum $> 1.3 \times 10^4$ rad m^{-2} (Anna-Thomas et al., 2023), and the progenitor argued to be embedded in a combined magnetar wind nebula and supernova remnant (Zhao and Wang, 2021). We include FRB 20121102A in our analysis despite its extreme RM, but, where relevant, we comment on results without its inclusion.

5.2.1 Constraining the Contribution to $\mathrm{RM_{FRB}}$ from the IGM

In this subsection, we search for any trend of $\mathrm{RM_{EG}}$with redshift akin to the Macquart Relation for the dispersion measure.

In this case we do not expect a trend with redshift since there is no expected preferred direction of magnetic fields on cosmic scales. The random orientation of these intergalactic fields, and probable dominance of the turbulent field components, leads to field reversals along what can be considered to be a random walk— where the mean field is $\langle B \rangle \sim 0$, while $\sigma_B^2 \ggg 0$. Therefore, integrated along the line of sight, $\mathrm{B_{\parallel}}$ approaches zero on average (§5.0.1). We first, however, describe our approach to removing an estimated contribution to $\mathrm{RM_{FRB}}$ from our Galaxy.

5.2.1.1 Milky Way Rotation Measure ($\mathrm{RM_{MW}}$)

Each of the $\mathrm{RM_{FRB}}$ measurements include a contribution from the path through our galaxy. This includes both the interstellar medium and any halo component.

The Faraday map presented by Oppermann, N. et al. (2012) uses surveys of polarized extragalactic radio sources to determine rotation measures within and outside of the Galactic plane.

This model's methodology and theoretical framework is used as a basis for the production and improvement of the HE20 model (Hutschenreuter and Enßlin, 2020; Hutschenreuter et al., 2022)—a Faraday sky model that uses the correlation between Galactic Faraday rotation and Galactic free-free emission to increase the accuracy of previously developed maps (Hutschenreuter and Enßlin, 2020). They also incorporate a new all-sky data set, which has a higher density of sources near the galactic plane and other under-resolved areas of the sky (such as the southern sky). These improvements increase the resolution of the resulting maps by a factor of two over previous studies (Hutschenreuter et al., 2022).

Therefore, we use the HE20 model of $\mathrm{RM_{MW}}$ to account for the Milky Way's contribution to $\mathrm{RM_{FRB}}$ to thereby isolate the extragalactic RM contribution:

$$\mathrm{RM_{EG}} = \mathrm{RM_{FRB}} - \mathrm{RM_{MW}} \tag{5.5}$$

Last, we note that maps such as these are limited in their spatial resolution in regards to particular lines of sight through the Milky Way. However, the HE20 model uses a total of 55,190 sources (primarily from the LOFAR Two-metre Sky Survey and NRAO VLA Sky Survey RM catalogs), resulting in improvements in resolution and uncertainties. The uncertainties mostly range from $80\,\mathrm{rad\,m^{-2}}$ in the plane of the galaxy to $\sim\ 0\,\mathrm{rad\,m^{-2}}$ as we move to lines of sight further from the disk. There are few regions in the Galactic plane (specifically towards Galactic

center) where the uncertainties reach $\simeq 300$ rad m^{-2}(Hutschenreuter et al., 2022), but none of our FRBs have LOS near $|l| \sim 0°$.

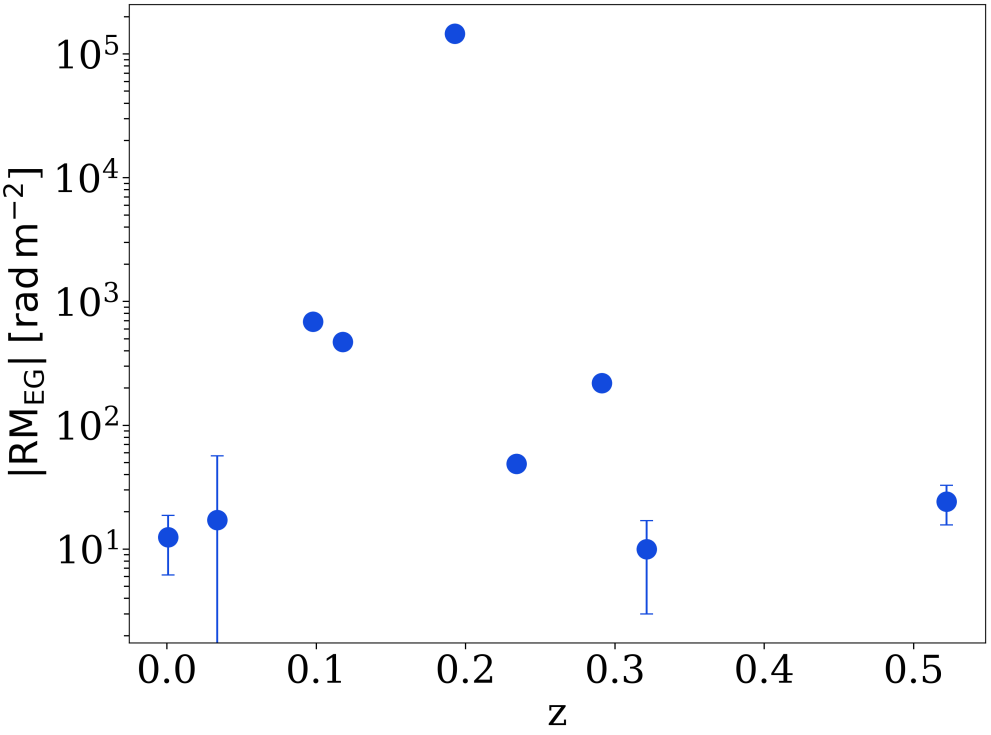

Figure 5.4: Amplitude of the extragalactic rotation measure ($|\mathrm{RM_{EG}}|$) as a function of redshift (z) for the full set of FRBs in this sample. Error bars are shown, where some errors are smaller than the points. There is no significant correlation between the two, in sharp contrast to the burst DM which shows a clear dependence on redshift (evidenced in the Macquart Relation; Macquart et al., 2020; James et al., 2022). This indicates no strong influence from intergalactic magnetic fields and that the local environment (host and immediate burst environment) dominates $|\mathrm{RM_{EG}}|$. The extremum of the $|\mathrm{RM_{EG}}|$ distribution is FRB 20121102A which is expected to reflect a highly magnetized environment in which the burst resides.

5.2.1.2 Correlating $\mathrm{RM_{EG}}$ with z

Figure 5.4 plots the absolute value of the extragalactic $\mathrm{RM_{EG}}$ for each sightline against the FRB redshift. There is no discernible trend between these two quantities. Both parameter (slope of the best-fit line) and non-parametric (Spearman) tests reveal no significant correlation. This stands in stark contrast to the strong correlation observed between DM and redshift (the Macquart relation), which arises from the highly ionized cosmic web (Macquart et al., 2020). The absence of any apparent correlation in Figure 5.4 implies the IGM makes little contribution to the overall RM, primarily due to reversals in the magnetic field over cosmic scales. This is consistent with upper limits for the contribution of intervening galaxy halos (Lan and Prochaska, 2020).

For the remainder of the paper, we assert that the cosmic contribution to $\mathrm{RM_{FRB}}$ ($\mathrm{RM_{cosmic}}$) is negligible. Therefore $\mathrm{RM_{FRB}}$ is dominated by only two components along the sightline, our Galaxy and the FRB host. In turn, this implies $\mathrm{RM_{EG}}$ is dominated by the host contribution and given equation 5.5 we have,

$$\mathrm{RM_{host}} \approx (\mathrm{RM_{FRB}} - \mathrm{RM_{MW}})\,(1+z)^2 \quad , \tag{5.6}$$

which explicitly applies a factor of $(1+z)^2$ to correct to the host rest-frame. In what follows, we test equation 5.6 and then derive estimates for the magnetic field strength of the FRB host galaxies based on its evaluation.

5.2.2 Estimating the Host Dispersion Measure ($\mathrm{DM_{host}}$)

In section 5.2.1.2, we argued that the extragalactic RM ($\mathrm{RM_{EG}}$) estimates for the FRBs arise from ionized and magnetized gas within their host galaxies. Adopting this expectation, we may leverage observations of the galaxies and the local environments of the FRBs to provide

Table 5.2: Daggers denote repeating FRBs. $\mathrm{DM}_{\mathrm{host}}^{\mathrm{Macquart}}$ for FRBs 20180924B, 20190102C, and 20200120E are all below 30. For the calculation of $\mathrm{B}_{\parallel}$ we set a minimum DM of 30 $\mathrm{pc\,cm^{-3}}$, but report the derived values here. Those left blank do not have the necessary measurements to calculate $\mathrm{DM}_{\mathrm{host}}$ using the particular method.

FRB	$\mathrm{RM}_{\mathrm{host}}$	$\mathrm{RM}_{\mathrm{MW}}$	$\mathrm{DM}_{\mathrm{host}}^{\mathrm{H}\alpha}$	$\mathrm{DM}_{\mathrm{host}}^{\mathrm{UV}}$	$\mathrm{DM}_{\mathrm{host}}^{\mathrm{Macquart}}$	$\lvert\mathrm{B}_{\parallel}\rvert$
	$(\mathrm{rad\,m^{-2}})$	$(\mathrm{rad\,m^{-2}})$	$(\mathrm{pc\,cm^{-3}})$	$(\mathrm{pc\,cm^{-3}})$	$(\mathrm{pc\,cm^{-3}})$	$(\mu\mathrm{G})$
20121102A†	146127 ± 137	-18 ± 37	183	3519	231 ± 99	777 ± 366
20180916B†	-17 ± 40	-99 ± 39	167		113 ± 48	0.19 ± 0.43
20180924B	10.0 ± 7.0	16.3 ± 5.0	311	< 117	-3 ± 205	0.4 ± 2.8
20190102C	-219.5 ± 8.7	26.6 ± 7.7	177	< 202	17 ± 163	9 ± 54
20190608B	472 ± 15	-24 ± 13	135	154	181 ± 28	3.2 ± 1.1
20190711A†	-24.2 ± 8.5	19.4 ± 6.5		< 173	34 ± 333	0.9 ± 9.2
20191001A	48.8 ± 5.2	23.5 ± 4.3	512	< 116	272 ± 126	0.22 ± 0.11
20200120E†	-12.4 ± 6.3	-17.4 ± 5.8			7 ± 4	0.51 ± 0.26
20201124A†	-686 ± 26	-44 ± 24	810		181 ± 2	4.7 ± 1.2

further insight into the underlying magnetic field. In particular, we aim to provide an order-of-magnitude estimate for the magnetic field strength. Following standard treatment for sightlines through the Galactic ISM (e.g. Arshakian et al., 2009; Beck et al., 2019), one requires an estimate for the dispersion measure of the gas giving rise to $\mathrm{RM_{host}}$to calculate $|\mathrm{B}_{\parallel}|$. We will also use this DM estimate to guide the models of $\mathrm{RM_{host}}$ presented in Section 5.3.

We will make the further assumption that $\mathrm{RM_{host}}$ is dominated by gas within the host galaxy ISM and/or the local environment of the FRB. Specifically, we ignore any RM contribution from the diffuse and ionized gas of the host halo. This is due to the lower anticipated density of halo gas, as supported by galaxy formation theory and simulations (see § 5.3). Therefore, we wish to estimate the dispersion measure of the host foreground to the FRB. We define this quantity as $\mathrm{DM_{host,ISM}}$ and assume that $\mathrm{DM_{host}} \approx \mathrm{DM_{host,ISM}}$.

We consider several approaches to estimate $\mathrm{DM_{host,ISM}}$, each of which bears significant uncertainty. One approach follows Reynolds (1977) (further developed by Tendulkar et al. (2017)) who introduced a method to relate the emission measure EM ($\propto n_e^2$) to the sightline DM ($\propto n_e$) allowing for a parameterization of the unknown clumping of the gas. For EM, we consider two observed fluxes of radiation from gas towards the FRB.

The first EM is the observed surface brightness of Hydrogen recombination radiation (e.g. Hα). In its favor, the majority of FRB host galaxies have one or more optical, nebular Hydrogen recombination lines measured from optical spectroscopy (e.g. Bhandari et al., 2022). On the negative side, most of these were obtained from long-slit observations centered on the host galaxy and not necessarily including the FRB location. Furthermore, the typical atmospheric seeing of $\sim 1''$ and the generally small angular sizes of the galaxies (with exceptions) yield only a characteristic surface brightness from the host galaxy ISM. Table 5.2 lists a set of estimates of $\mathrm{DM_{host}^{H\alpha}}$ based on published, integrated Hα flux measurements[1], the angular sizes of the galaxies,

[1]Or Hβ converted to Hα using standard nebular flux ratios.

and corrected for dust extinction. These range from one to many hundreds $\mathrm{pc\,cm^{-3}}$.

For the subset of FRBs with hosts observed at high spatial resolution, we may better constrain the emission measure at the FRB location. Six of the 9 FRBs have extant Hubble Space Telescope (HST) observations at $\approx 0.1''$ FWHM resolution (Mannings et al., 2021). These are primarily broadband images at UV and near-IR wavelengths. The UV emission is dominated by radiation from massive stars which also drive the nebular Hydrogen emission and the two are strongly correlated (e.g. Calzetti, 2001). For those with UV, we use the standard scaling between near-UV luminosity and Hα luminosity (Kennicutt, 1998a) to estimate the Hα surface brightness from the UV observations. We then calculate the emission measure and relate this to a dispersion measure estimate. Table 5.2 lists the $\mathrm{DM_{host}^{UV}}$ estimates for these six galaxies.

Last, we consider a complementary approach to estimating $\mathrm{DM_{host,ISM}}$ using the Macquart Relation which relates the cosmic dispersion measure $\mathrm{DM_{cosmic}}$ with redshift (Macquart et al., 2020). We refer to this estimation as $\mathrm{DM_{host}^{Macquart}}$. The method is to subtract from the observed total dispersion measure $\mathrm{DM_{FRB}}$ estimates for the Galactic ISM and halo ($\mathrm{DM_{ISM}}$, $\mathrm{DM_{halo}}$) and the cosmic web ($\mathrm{DM_{cosmic}}$):

$$\mathrm{DM_{host}^{Macquart}} = \mathrm{DM_{FRB}} - \mathrm{DM_{ISM}} - \mathrm{DM_{halo}} - \mathrm{DM_{cosmic}} \tag{5.7}$$

We use the NE2001 model (Cordes and Lazio, 2003) of the Galactic ISM to evaluate $\mathrm{DM_{ISM}}$ for each FRB sightline and assume the Milky Way halo contributes $\mathrm{DM_{halo}} = 40\mathrm{pc\,cm^{-3}}$ (e.g. Prochaska and Zheng, 2019). From the host galaxy redshift, we calculate the average $\langle \mathrm{DM_{cosmic}} \rangle$ (Macquart et al., 2020). This yields the $\mathrm{DM_{host}^{Macquart}}$ values listed in Table 5.2 which have also been corrected to the rest frame of the host (i.e. we applied a factor of $1+z$). Formally, these include gas from both the ISM and halo of the host galaxy and current work suggests the host halo term may contribute several tens $\mathrm{pc\,cm^{-3}}$ (Prochaska and Zheng, 2019). We also note

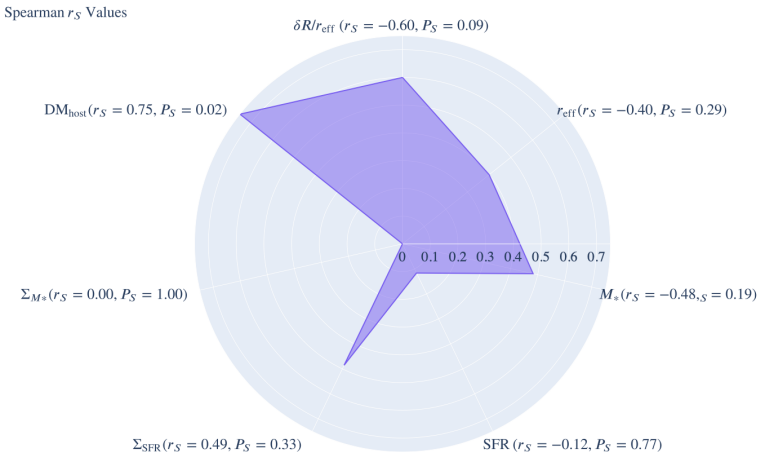

Figure 5.5: A radar plot showing Spearman r_S values as tests for the correlation between absolute rotation measure (|RM|) and a range of galaxy-scale and local environment related measures. The radial values represent show the absolute value of the stated r_S values, and the associated significance measures are shown as well. A negative r_S represents anti-correlation. The only correlation meeting our significance criterion $(P_S < 0.05)$ is that with $\mathrm{DM_{host}}$. This positive correlation can naturally arise from the fact that both quantities are sensitive to the electron density in the host ISM.

that structure in the cosmic web lends to an asymmetric scatter about $\langle \mathrm{DM_{cosmic}} \rangle$ and the median $\mathrm{DM_{cosmic}}$ value is predicted to be several tens $\mathrm{pc\,cm^{-3}}$ lower than the mean. These two corrections offset against one another, and we therefore proceed with equation 5.7 for our $\mathrm{DM_{host}^{Macquart}}$ estimates acknowledging that these bear $\sim 30 \mathrm{pc\,cm^{-3}}$ uncertainty.

Inspecting the values of $\mathrm{DM_{host,ISM}}$ listed in Table 5.2, one notes each approach exhibits a distinct distribution. The $\mathrm{DM_{host}^{H\alpha}}$ estimations span the largest range and exhibit the largest values. Indeed, many exceed $\mathrm{DM_{host}^{Macquart}}$ and even the total $\mathrm{DM_{FRB}}$ of the sightline. The dust-corrected $\mathrm{DM_{host}^{UV}}$ distribution are primarily upper limits of one hundred to a few hundreds $\mathrm{pc\,cm^{-3}}$ and are generally consistent with $\mathrm{DM_{host}^{Macquart}}$. We proceed with analysis that adopts $\mathrm{DM_{host}^{Macquart}}$ for the host dispersion measure, however of the values calculated for $\mathrm{DM_{host}^{Macquart}}$are ~ 1 or negative. Therefore we impose a minimum value of 30 $\mathrm{pc\,cm^{-3}}$ based on the minimum value of our own Galactic ISM (NE2001), noting that all of the galaxies exhibit signatures of star-formation and must harbor a non-negligible ISM. This minimum value also accounts for uncertainty in the methodology. For completeness, the values presented in Table 5.2 show the calculated values for $\mathrm{DM_{host}^{Macquart}}$including those which are below this minimum. However, the minimum threshold is implemented in all subsequent analysis.

5.2.3 Correlating Host Characteristics with Rotation Measure

We now test for correlations between global and local characteristics of the host galaxies and RM isolated to the host galaxy (i.e. with the Galactic component subtracted using equation 5.6; $\mathrm{RM_{host}}$). To the extent that $\mathrm{RM_{host}}$ traces gas beyond the local environment, we may identify correlations with the host galaxy properties. For example, one may expect FRBs found in regions of elevated star-formation to exhibit a higher rotation measure. Magnetic fields get wrapped up into forming stars, but the fields can also be amplified by ionizing radiation and turbulence from violent star formation, cloud collapse, and massive star death.

Specifically, we consider global measures of the star-formation rate (SFR), stellar mass (M_*), and galacto-centric offset (relative to the galaxy effective radius, $\delta R/r_e$). We also consider local measures of the SFR and M_* surface densities ($\Sigma_{\rm SFR}$, $\Sigma_{\rm M*}$; Table **??**) and our estimate of $\rm DM_{host}$ which would include both local and ISM contributions.

We perform Spearman tests - computing Spearman correlation coefficients r_S - with the null hypothesis that there is no correlation between rotation measure and a given measurement. We select the Spearman test because there is no assumption of Gaussian distributions for the variables. We perform the analysis in log-log space (as opposed to linear space) as the power-law relationships appear linear, and many of these values span several orders of magnitude. Last, we set a threshold of the Spearman probability for a significant correlation at $P_S < 0.05$ (i.e. requiring 95% significance).

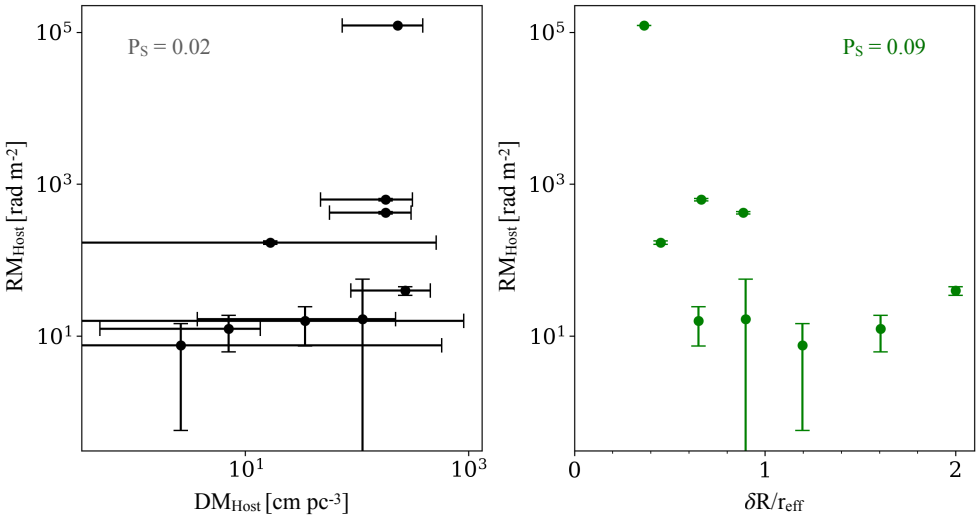

Figure 5.6: $\rm RM_{host}$as functions of $\rm DM_{host}$(*left, black*) and $\delta R/r_e$(*right, green*), with associated $P_S$values. We can see a positive correlation by eye between $\rm RM_{host}$and $\rm DM_{host}$, however, a correlation between $\rm RM_{host}$and $\delta R/r_e$is not as apparent.

The absolute values of the resultant r_S values are shown in Figure 5.5. Although

there are a number of parameters for which $|r_s| > 0.5$, the condition for significance is only satisfied for one quantity: $\mathrm{DM_{host}}$. A positive correlation between $\mathrm{DM_{host}}$ and $\mathrm{RM_{host}}$ is in line with expectation because both quantities depend on the electron density of the host ISM. The correlation also lends further support to the assertion that $\mathrm{RM_{EG}}$ is dominated by $\mathrm{RM_{host}}$.

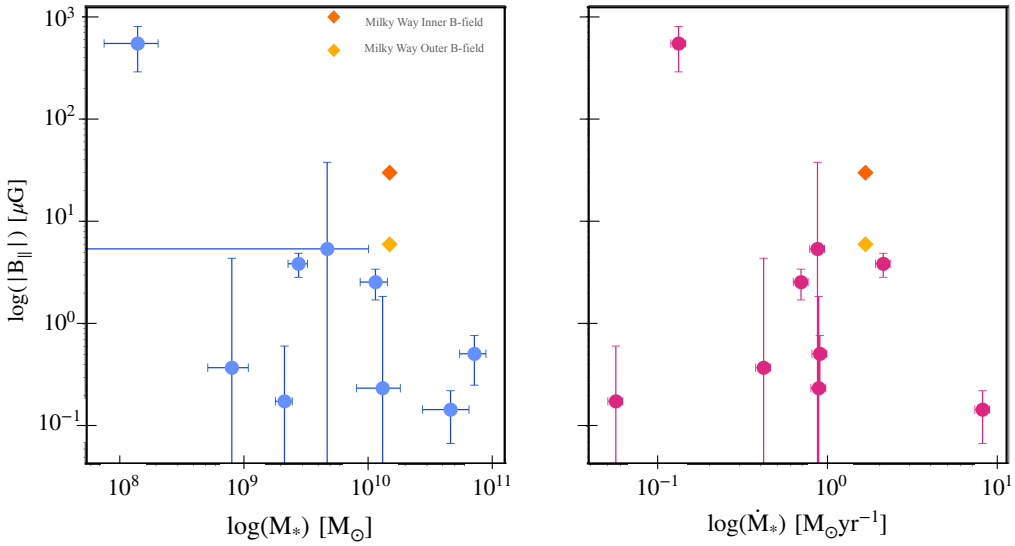

Figure 5.7: Comparison of the magnitude of the $\mathrm{B_{\parallel}}$ component of the magnetic field to stellar mass (right panel) and star-formation rates (left panel). We also show values determined for the Milky Way (Wielebinski and Beck, 2005), for the bulge/inner field in *yellow* and the disk/outer field in *orange*, using values for mass and star-formation rate found in Fragione and Loeb (2017) and Licquia and Newman (2015), respectively. We find no apparent correlations between these global galactic characteristics and magnetic field measurements in this sample of FRB hosts.

The next strongest correlation is an anti-correlation between $\mathrm{RM_{host}}$ and $\delta R/r_e$, although with $P_S > 0.05$. This trend follows observed and simulated inverse relationships between $|\mathrm{B}_\parallel|$ and radius (e.g. Wielebinski and Beck, 2005; Pakmor et al., 2017). We await future observations to confirm (or refute) such a trend in FRB observations.

As our sample is limited a sample size of 9 FRBs, such tests should be repeated with greater confidence with a larger sample size. One also notes that the significance of these analyses is reduced by a trials-factor penalty incurred when testing for multiple correlations.

5.2.4 B-field Estimation

As stated by Arshakian et al. (2009), rotation measures of polarized background sources can be used to reconstruct a host or intervening galaxy's magnetic field topology. FRB signals have since been shown to be one such source. FRBs and their rotation measures can reveal the orientation and magnitude of ordered magnetic fields, making them a powerful tool. Here we look at the power of FRB sightlines to provide insight on the fields of the galaxies that host well-localized bursts.

As defined, RM is the sightline integral of the parallel component of the magnetic field weighted by the electron density. Therefore the ratio of RM to DM (the unweighted n_e integral) yields an estimate of the magnetic field, after accounting for differences in the prefactors (e.g. Akahori et al., 2016; Pandhi et al., 2022):

$$\begin{aligned} \langle B_\parallel \rangle &\approx \frac{\mathrm{C_D RM}}{\mathrm{C_R DM}} \\ &= 12.3 \left(\frac{\mathrm{RM}}{10\,\mathrm{rad\,m^{-2}}} \right) \left(\frac{\mathrm{DM}}{10^3\,\mathrm{pc\,cm^{-3}}} \right)^{-1} \mathrm{nG} \end{aligned} \tag{5.8}$$

with $\mathrm{C_D}$ and $\mathrm{C_R}$ constants equal to 1000 and 811.9, respectively. Akahori et al. (2016) propose (with some improvements to equation 5.8) that many measurements of $\mathrm{RM_{FRB}}$ and $\mathrm{DM_{FRB}}$ can

provide the data necessary to probe inter-galactic magnetic fields (IGMFs). This estimation also assumes a constant magnetic field and that there is no correlation between $n_e$and $B_{\parallel}$, whereas it is possible the magnetic field strength will likely decrease exponentially with radius and height in the disk (similar to n_e). These effects should be less than an order of magnitude making the given ratio sufficient for estimating the magnitude of the magnetic fields in our sample's host galaxies. Furthermore, we adopt values of $\mathrm{RM_{host}}$ and $\mathrm{DM_{host}}$ to isolate the magnetic field estimation to within the host galaxy.

Considering the turbulence and ionization due to active star-formation and the deaths of massive stars, one may suspect a relationship between star-formation rate and the magnitude of magnetic fields in the host. We also investigate the relationship between stellar mass and magnetic field strength. Rodrigues et al. (2018) find —for galaxies at $z = 0$— a slight positive correlation between galaxy mass and magnetic field, but note that this correlation is broken by a number of lower-mass hosts with much higher magnetic field strengths. In Figure 5.7, we do not see a clear trend with strength $|B_{\parallel}|$ as a function of mass nor star-formation rate, in contrast to the predictions of Rodrigues et al. (2018). FRB 20121102A exhibits the highest rotation measure of all the bursts, but resides in the lowest-mass host. This is indicative of the highly magnetized environment that the burst progenitor lives within (Michilli et al., 2018).

In most cases, the magnetic field strengths estimated are lower than values quoted for the Milky Way ($\approx 6\mu G$ in the outer reaches of the galaxy and $30\mu G$ in the inner region towards the bulge). These Galactic values are dominated by the small-scale random fields which contrasts the regular fields along the line of sight that dominate RM. Comparing these two sets of measurements allows us to make distinctions between the strengths of various field components. We note that the values we have determined are largely consistent with $\simeq \mu G$ field magnitudes, which is broadly accepted as the general magnitude of large-scale regular fields measured in galactic disks (Beck et al., 2019).

5.3 Modeling Galactic Magnetic Fields

5.3.1 Auriga Model

To gain a better understanding of the physical mechanisms that can influence the magnetic fields in the host galaxies of our observed FRBs, we compare them to similar galaxies in the Auriga simulations.

The Auriga simulations are a set of cosmological magneto-hydrodynamical zoom-in simulations of Milky Way-like galaxies (Grand et al., 2017). They model magnetic fields in the approximation of ideal magnetohydrodynamics (MHD) using a second order finite volume scheme (Pakmor et al., 2011; Pakmor and Springel, 2013) in the Arepo code (Springel, 2010; Pakmor et al., 2016; Weinberger et al., 2020). The magnetic field is initialised at $z = 127$ as a uniform magnetic seed field with a strength of 1.6×10^{-10} physical G. The simulation then evolves the magnetic field self-consistently until $z = 0$.

When the galaxies first form, the magnetic field is quickly amplified via a turbulent small-scale dynamo and saturates before $z = 4$ with a magnetic energy density that reaches $\sim 10\%$ of the turbulent energy density and erases any information about the seed field in the galaxy (Pakmor et al., 2014). After the galaxies form a disk at $z < 2$ the differential rotation in the disk leads to a second phase of magnetic field amplification that ends when the magnetic energy density reaches equipartition with the turbulent energy density (Pakmor et al., 2017). The magnetic field properties, synthetic Faraday rotation maps, and the magnetic field in the circum-galactic medium of the Auriga galaxies has been shown to be consistent with observations (Pakmor et al., 2016, 2018, 2020).

The Auriga simulations focus on a Lagrangian high-resolution region with a typical radius of 1 Mpc/h around the central Milky Way-mass galaxies. This high-resolution region contains a large number of smaller galaxies without contamination from low-resolution dark

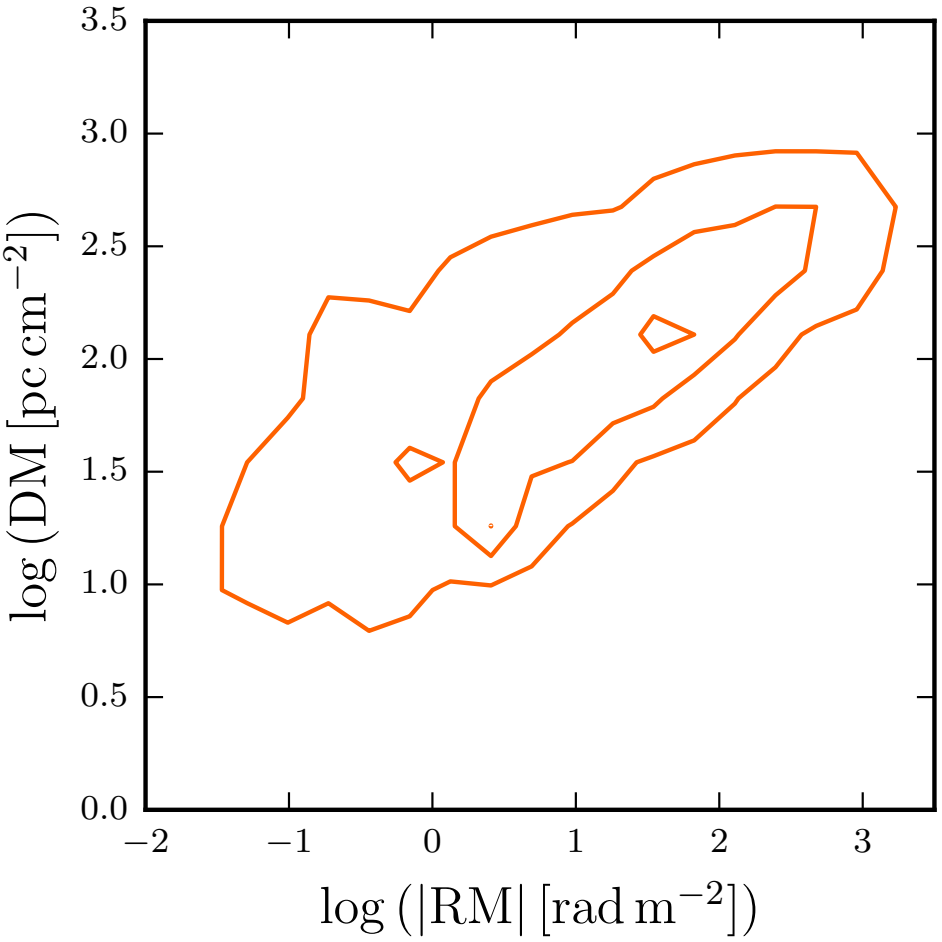

Figure 5.8: Correlation between RM and DM values for lines of sight from matched host galaxies in Auriga. We show 10%, 50%, and 90% contours of the distribution. Although there is non-negligible scatter, the RM and DM are strongly correlated in the simulations.

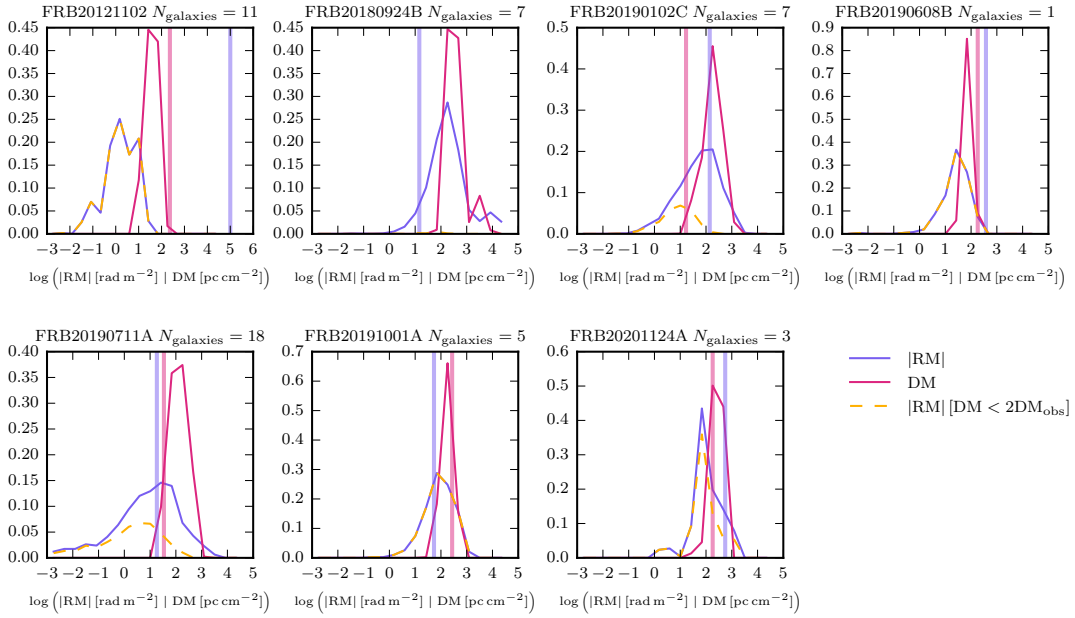

Figure 5.9: RM and DM distributions for lines of sight from matched host galaxies in Auriga. The name of the matched FRB host and the number of matching Auriga galaxies found are listed above each panel. Shown are histograms of the DM values (solid red lines) and absolute RM values (solid purple lines) along each line of sight. The vertical red and purple lines indicate the observed or derived $\mathrm{RM_{host}}$ and $\mathrm{DM_{host}^{Macquart}}$ values. We also show histograms of absolute RM values that include only lines of sight with a consistent DM value (dashed yellow lines; absent in panels where no consistent DM was found). The RM distributions predicted from the Auriga galaxies are generally in good agreement with the observed values, with the glaring exception of FRB20121102A whose RM value is far away from any lines of sight we find in Auriga. The modeled RM PDF for FRB20190608B is also noticeably lower than the observed value. The derived $\mathrm{DM_{host}^{Macquart}}$ value for FRB20180924B is negative, therefore there is no vertical line shown here.

Table 5.3: Daggers denote repeating FRBs. The data included here are taken from the Auriga simulations. No matches were found for FRBs 20180916B and 20200120E, thus they have been left blank.

FRB	RM Median	DM Median	RM95%Interval	DM95%Interval
	($\mathrm{rad\,m^{-2}}$)	($\mathrm{pc\,cm^{-3}}$)	($\mathrm{rad\,m^{-2}}$)	($\mathrm{pc\,cm^{-3}}$)
20121102A†	2.02	2.02	[0.04,18.56]	[0.04,18.56]
20180916B†				
20180924B	146.22	57.31	[6.01,12598.00]	[4.20,117.59]
20190102C	53.55	7.24	[0.63,1055.81]	[0.28,69.17]
20190608B	25.84	25.84	[1.80,120.41]	[1.80,120.41]
20190711A†	8.58	1.66	[0.00,745.50]	[0.00,97.79]
20191001A	77.71	77.71	[3.40,635.87]	[3.40,635.87]
20200120E†				
20201124A†	86.13	67.51	[2.83,837.41]	[2.04,789.91]

matter particles that we also include in our sample here. We focus our analysis on the six high-resolution simulations of the Auriga project with a baryonic mass resolution of $\approx 7-8\times10^3\,\mathrm{M_\odot}$. These are supplemented by yet unpublished simulations with the same mass resolution, centered on lower mass galaxies ($M_{\mathrm{halo}} = 10^{10} - 10^{11.5}$ $\mathrm{M_\odot}$) for which the high-resolution regions also extend to about 5 times the virial radius around each central galaxy.

5.3.2 Host and sightline selection

We first find galaxies in our simulation suite with stellar mass, star formation rate, and effective radius consistent with the host galaxies of our FRB sample. We calculate the stellar mass of a simulated galaxy by including all stars within three times its stellar half mass radius. Its star formation rate is averaged over the last 100 Myr using newly formed stars within the same radius. We use the stellar half mass radius as a proxy for the effective radius. We include all galaxies (both central and satellite galaxies) that match the FRB sample to within twice the

observational error. For the effective radius, however, we add a 10 percent error in quadrature to the observational error, because in some cases the derived errors were so small that no match could be found. With this selection procedure, we found one or more matching galaxies for 7 out of the 9 observed host galaxies.

We tilt each of the galaxies into the observed inclination and then integrate the RM and DM values for 256 different lines of sight. The starting point of each line of sight is the position of a random star particle with an age younger than 200 Myr. The frequent incidence of FRBs one or near spiral arms, could indicate the association of FRBs with relatively young stellar populations. From the starting point we integrate each line of sight until it reaches an observer at a distance of 100 kpc. We checked that increasing the integration distance does not change our results.

The local electron density for the integration along the line of sight is computed exactly as described by Pakmor et al. (2018), in particular assuming that only the volume-filling warm phase of the ISM contributes and that this phase is fully ionised. The magnetic field is taken directly from the simulation.

5.3.3 Correlation between DM and RM

We show the correlation between RM and DM for all sightlines we computed from the Auriga galaxies in Figure 5.8. RM and DM are clearly strongly correlated, as expected. However, there is significant scatter, i.e. for a fixed DM value the RM value can vary by two orders of magnitude. Nevertheless, the scatter is small on the scale of the overall variation of five orders of magnitudes in DM and eight orders of magnitude in RM.

Motivated by the strong correlation between DM and RM we not only compare the RM distributions of all lines of sight of matched FRB host galaxies, but also compare to a subsample of lines of sight that show consistent DM values.

5.3.4 DM and RM of matched Auriga galaxies

We show the distribution of RM (purple lines) and DM (red lines) values for 256 lines of sights each of all galaxies in our sample consistent with the properties of the FRB host galaxies in Figure 5.9. We also show the measured values as vertical lines of the same color.

Strikingly, the shape of the distributions of synthetic DM and RM values match for most FRBs. The RM and DM distributions overlap with the values inferred for the FRB host galaxies from our observations with the exception of FRB20201124A. Median values and 95% confidence intervals are shown in Table 5.3.

We also show the RM distributions restricted to lines of sights that have a DM value consistent with the observed host galaxy DM ($\mathrm{DM_{sim}} <$
$max\left(100\,\mathrm{pc\,cm^{-3}}, 2 \times \mathrm{DM_{host}^{Macquart}}\right)$, shown by the dashed, yellow curves). For most FRBs this restricted RM distribution is essentially the same as the full RM distribution. For FRB20190102C, FRB20201124A, and FRB20190711A this restriction reduces the high RM tail of the distribution. Interestingly, in all three cases the host RM estimated from observations lies on this tail that is reduced significantly by the restriction on DM. We also note (as seen in Figure 5.9) the noticeable difference between the modeled PDF and observed $\mathrm{RM_{host}}$for FRB20190608B. Though, again the value lands on the tail of the distribution. This could point to an non-negligible contribution of the local environment to the observed RM, as was discussed by Chittidi et al. (2021). The authors point out the high RM in comparison to other bursts such as FRB 20180916, implying a magnetised local environment.

A larger sample is necessary to determine whether or not these variations are truly due to local effects.

An extreme exception is FRB20121102A. We do not find any lines of sight that have an RM value even remotely comparable to the large observed value. In contrast, the DM value

is barely consistent with our synthetic lines of sight. This indicates that the magnetic field dominating the RM of FRB20121102A is part of its local stellar environment that is not included in our simulations. Michilli et al. (2018) discusses this highly magnetized local environment.

Note also, that it is likely increased scatter broadening of the FRB signal would bias against FRBs being detected with high host DM contribution.

5.4 Discussion

This sample represents the largest collection of FRB rotation measures presented with accompanying high-precision localizations and follow-up imaging of the associated hosts. A majority of the hosts in this sample are massive, star-forming galaxies at $z < 0.5$, with a few exceptions at lower mass or SFR.

To explore the relationships between FRB rotation measures and host characteristics, we first isolated the extragalactic contribution to the rotation measure ($\mathrm{RM_{EG}}$). We used the Galactic Faraday rotation map developed by Hutschenreuter et al. (2022) and found no correlation between $\mathrm{RM_{EG}}$and z. This is consistent with measurements of the IGMF found in the publication by Carretti et al. (2022) which follows from an expected random nature and much lower strength of the fields in the IGM.

We therefore disregarded IGMF contributions and assert that $\mathrm{DM_{EG}}$ is dominated by the rotation measure of the host galaxy $\mathrm{DM_{host}}$. We find a strong correlation between $\mathrm{RM_{host}}$ and $\mathrm{DM_{host}}$, which supports this assertion and provides encouraging confidence that FRBs probe the magnetic fields of their host galaxies. This correlation is expected if the magnetic field has a significant ordered component that only varies weakly along the line of sight. Then both quantities depend similarly on the integrated density of the ionized medium along the line of sight through the host galaxy. This is consistent with our observational and theoretical picture

of magnetic fields in massive disk galaxies (Beck, 2015; Pakmor et al., 2017).

There is evidence for an anti-correlation between host-normalized galacto-centric offset and $\mathrm{RM_{host}}$ but at less than 95% confidence. A larger dataset is required to test whether FRBs reveal this relationship, though observed and modeled field strengths have been seen to show some radial dependence.

We considered several methods to isolate the host contribution to the dispersion measure $\mathrm{DM_{host}}$ relating the emission measure to dispersion measure (Reynolds, 1977) and applying the Macquart relation (Macquart et al., 2020) to estimate $\mathrm{DM_{host}}$. We then use the relation between dispersion and rotation measures described in papers such as Akahori et al. (2016) & Pandhi et al. (2022) to make an estimate of $\mathrm{B_{\parallel}}$ for each of our host galaxies.

With this method we find magnetic field strength estimates for our sample of the order of $\sim 1\mu G$. The estimate, however, disregards field reversals of the magnetic field along the line of sight as well as differences in the exponential scaling of the magnetic field strength and electron densities with radius and height in the disk. Therefore, although the values are lower than values quoted for the Milky Way (see Figure 5.7), they are better seen as lower limits and are fully consistent with general expectations for galactic magnetic field strengths (Beck, 2015). The uncertainty in our determinations of $\mathrm{DM_{host}^{Macquart}}$could have some effect on the derived $\mathrm{B_{\parallel}}$, but would not cause a notable increase.

Four (possibly 5) of the hosts in this sample exhibit spiral structure, and the bursts originate on or near the spiral arms. According to Beck (2015), the strongest ordered fields are found in inter-arm regions due to shear caused by differential rotation and a large scale dynamo that operates preferentially in the inter-arm regions. Because of the preferred location of FRBs on/near spiral arms, it is possible that our field strengths are referring to medium-scale ($\sim 1\,\mathrm{kpc}$) regular fields that are affected by turbulence in the spiral arms. Figure 5.10 shows where our measurements lie with respect to lines of constant $\mathrm{B_{\parallel}}$ of varying magnitudes (with the values we

derived shown in Table 5.2). These values align well with the average strengths of large-scale regular fields (on scales of 5-10 kpc Beck et al., 2019), where the large scale rotation sets the strength and structure of the magnetic field.

Using forward modelling of cosmological simulations instead, we also find that observed $\mathrm{RM_{host}}$ and therefore $\mathrm{B_{\parallel}}$, are consistent with the Auriga simulations (see Figure 5.9). There is the notable exception of FRB 20121102A, which we know is embedded in a highly magnetized environment. The predicted RMs for this FRB were not able to approach the observed value, as any contribution from local environments was not included. This provides some hope that with a sufficient number of FRBs with polarization data and $\sim mas$ localizations, we will be able to disentangle the ISM and local environment contributions to the RM, and provide constraints on each.

Limiting the simulated sightline-selection to those more consistent with the observed DM for each burst reduces the tail towards high RM values of the predicted RM distribution for three of the galaxies. Although the distribution is still consistent with the observed values, the majority of predicted RM values fall below the observed ones. This could imply a non-negligible contribution from the local stellar environment of the FRB.

Combining FRB RM signals with measures of synchrotron polarization and estimates using galactic Zeeman effect measurements — which characterize the ISM magnetic field — may also help to disentangle the magnetic field contributions within the host galaxy.

Finally, we find insignificant correlations with extant properties such as r_e, SFR, $\Sigma_{\mathrm{M}*}$, M_*, shown in Figure 5.5. With larger, upcoming surveys, these relationships can be explored in more detail with higher statistical power. There is also no apparent relationship between FRB repetition and the host and environmental characteristics we have explored in this paper. There also seems to be little differentiation in the sample presented by Gordon et al. (2023) where they explore the overall characteristics and star-formation histories of FRB hosts. This is in contrast

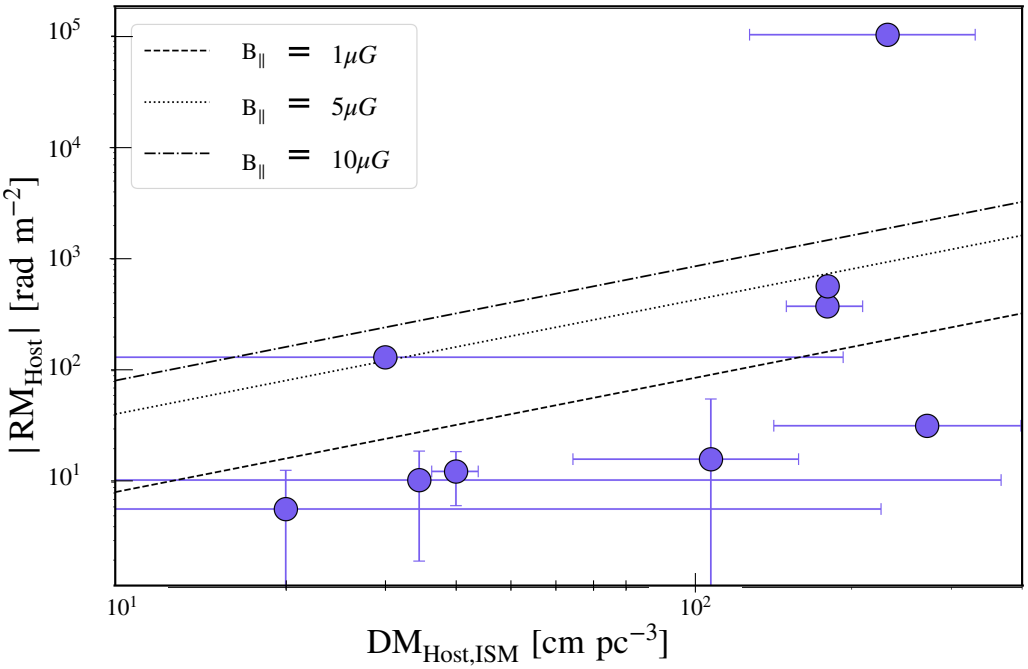

Figure 5.10: RM_{host} and $DM_{host,ISM}$ with lines of constant magnetic field strength (1 μG, dashed; 5 μG, dotted; 10 μG, dash-dotted). We calculate the value of $B_{\parallel}$ for each of the FRBs using Equation 5.8. The majority of the values are less than 5 μG, with many even falling below 1 μG. There is one outlier, with a field magnitude far exceeding 10 μG. These values are relatively consistent with μG fields, but are at the lower end of the range of 1-15 μG.

to papers such as Pleunis et al. (2021) which point out that there are some marked differences in burst characteristics (such as bandwidth and duration) of repeating and non-repeating FRBs.

We plan to repeat and expand this study with a larger sample of more precisely localized bursts with accompanying high-resolution imaging and spectroscopy. More data would not only aid in the narrowing of possible progenitors, we can also learn about galactic magnetism and its effects on galaxy formation and evolution. With the onset of large-scale surveys such as CRAFT with the upcoming CRACO upgrade, the number of FRBs that meet these criteria will vastly increase ($\sim$ 3 FRBs per day!), and help to determine what, on average, the local environments of FRBs look like in terms of stellar populations, magnetism and more, and investigate (inter-)galactic magnetism over cosmological time!

Chapter 6

Conclusions: To FRB Origins and Beyond

Since the discovery of the first FRB 18 years ago (Lorimer et al., 2007), FRB science has evolved from serendipitous detections to dedicated discovery experiments, yielding an exponentially-increasing number of detections. At this point in time, over 100 events have been successfully associated with host galaxies, thereby enabling the measurement of redshifts global host properties, and some local environment properties (Tendulkar et al., 2017; Heintz et al., 2020; Bhandari et al., 2022; Gordon et al., 2023; Ibik et al., 2024). As the observations grow richer, a fundamental question remains: *what are the progenitor(s) of FRBs?* While over 50 explanations have been advanced to explain the properties of FRBs (Platts et al., 2019), the prevailing view associates them with magnetars, strongly supported by the localization of the CHIME FRB 20200428A to the known *Galactic* magnetar SGR 1935+2154 (Bochenek et al., 2020).

In this thesis I explore what the local environment characteristics of FRBs can tell us about their origins, and find that, in many cases, they share characteristics with both CC- and

Ia-SNe — somehow spanning a large mass range of stellar progenitors. Through examination of the light, density of stellar mass, density of star formation, and distances to spiral structure we find that, perhaps, a scenario invoking binary interactions would produce progenitors that match the characteristics that we have determined. While we don't find very strong correlations between local measures and burst characteristics, there is still broad phase space to be explored and methods to be tried. Beyond this point, more detailed statistical studies of the relationships between local measures and burst properties should be undertaken to truly flesh out the spectrum of possibilities.

As FRB detection experiments expand with programs such as CRACO, CHIME Outriggers, and DSA-2000 on the horizon, the numbers of FRBs with ultra-precise localizations will reach into the thousands! Progenitor studies will have incredible statistical power, and a complete picture of the FRB (and FRB host galaxy) population will come into focus.

Cosmologically, follow-up observations of FRB environments have now only provided a direct detection of the missing baryons (Macquart et al., 2020; Simha et al., 2020), but also the first constraints on the circumgalactic medium (CGM) of $z < 1$ galaxies including a unique measure of the gas density and CGM magnetic field (Prochaska et al., 2019b). We have also demonstrated the power of FRBs to probe the magnetic fields of their host galaxies. The combination of burst rotation and dispersion measures allow FRBs to be test-cases for ground-breaking magneto-hydrodynamic simulations that seek to understand the many axes of galaxy evolution (e.g. magnetic fields and the circumgalactic medium). Looking forward, large samples of FRBs with RMs and DMs could be used to understand cosmological magnetic fields, circumgalactic and halo magnetic fields, and even the magnetic field of our own Milky Way!

The mystery of FRBs continues, but the horizon that awaits us is full of creativity, excitement, and discovery.

Bibliography

T. M. C. Abbott, M. Adamów, M. Aguena, S. Allam, A. Amon, J. Annis, S. Avila, D. Bacon, M. Banerji, K. Bechtol, M. R. Becker, G. M. Bernstein, E. Bertin, S. Bhargava, S. L. Bridle, D. Brooks, D. L. Burke, A. Carnero Rosell, M. Carrasco Kind, J. Carretero, F. J. Castander, R. Cawthon, C. Chang, A. Choi, C. Conselice, M. Costanzi, M. Crocce, L. N. da Costa, T. M. Davis, J. De Vicente, J. DeRose, S. Desai, H. T. Diehl, J. P. Dietrich, A. Drlica-Wagner, K. Eckert, J. Elvin-Poole, S. Everett, A. E. Evrard, I. Ferrero, A. Ferté, B. Flaugher, P. Fosalba, D. Friedel, J. Frieman, J. García-Bellido, E. Gaztanaga, L. Gelman, D. W. Gerdes, T. Giannantonio, M. S. S. Gill, D. Gruen, R. A. Gruendl, J. Gschwend, G. Gutierrez, W. G. Hartley, S. R. Hinton, D. L. Hollowood, K. Honscheid, D. Huterer, D. J. James, T. Jeltema, M. D. Johnson, S. Kent, R. Kron, K. Kuehn, N. Kuropatkin, O. Lahav, T. S. Li, C. Lidman, H. Lin, N. MacCrann, M. A. G. Maia, T. A. Manning, J. D. Maloney, M. March, J. L. Marshall, P. Martini, P. Melchior, F. Menanteau, R. Miquel, R. Morgan, J. Myles, E. Neilsen, R. L. C. Ogando, A. Palmese, F. Paz-Chinchón, D. Petravick, A. Pieres, A. A. Plazas, C. Pond, M. Rodriguez-Monroy, A. K. Romer, A. Roodman, E. S. Rykoff, M. Sako, E. Sanchez, B. Santiago, V. Scarpine, S. Serrano, I. Sevilla-Noarbe, J. A. Smith, M. Smith, M. Soares-Santos, E. Suchyta, M. E. C. Swanson, G. Tarle, D. Thomas, C. To, P. E. Tremblay, M. A. Troxel, D. L. Tucker, D. J. Turner, T. N. Varga, A. R. Walker, R. H. Wechsler, J. Weller, W. Wester, R. D. Wilkinson, B. Yanny, Y. Zhang, R. Nikutta, M. Fitzpatrick, A. Jacques, A. Scott,

K. Olsen, L. Huang, D. Herrera, S. Juneau, D. Nidever, B. A. Weaver, C. Adean, V. Correia, M. de Freitas, F. N. Freitas, C. Singulani, G. Vila-Verde, and Linea Science Server. The Dark Energy Survey Data Release 2. , 255(2):20, Aug. 2021. doi: 10.3847/1538-4365/ac00b3.

S. Abdeen, B. L. Davis, R. Eufrasio, D. Kennefick, J. Kennefick, R. Miller, D. Shields, E. B. Monson, C. Bassett, and H. O'Mara. Evidence in favour of density wave theory through age gradients observed in star formation history maps and spatially resolved stellar clusters. , 512 (1):366–377, May 2022. doi: 10.1093/mnras/stac459.

K. Aggarwal, T. Budavári, A. T. Deller, T. Eftekhari, C. W. James, J. X. Prochaska, and S. P. Tendulkar. Probabilistic Association of Transients to their Hosts (PATH). , 911(2):95, Apr. 2021. doi: 10.3847/1538-4357/abe8d2.

T. Akahori and D. Ryu. Faraday Rotation Measure due to the Intergalactic Magnetic Field. II. The Cosmological Contribution. , 738(2):134, Sept. 2011. doi: 10.1088/0004-637X/738/2/134.

T. Akahori, D. Ryu, and B. M. Gaensler. Fast Radio Bursts as Probes of Magnetic Fields in the Intergalactic Medium. , 824(2):105, June 2016. doi: 10.3847/0004-637X/824/2/105.

J. Anderson. Supplemental Dither Patterns for WFC3/IR. Space Telescope WFC Instrument Science Report, Aug. 2016.

J. Anderson, J. MacKenty, S. Baggett, and K. Noeske. The Efficacy of Post-Flashing for Mitigating CTE-Losses in WFC3/UVIS Images. Technical report, Baltimore, MD: STScI, Aug. 2012.

R. Anna-Thomas, L. Connor, S. Dai, Y. Feng, S. Burke-Spolaor, P. Beniamini, Y.-P. Yang, Y.-K. Zhang, K. Aggarwal, C. J. Law, D. Li, C. Niu, S. Chatterjee, M. Cruces, R. Duan, M. D. Filipovic, G. Hobbs, R. S. Lynch, C. Miao, J. Niu, S. K. Ocker, C.-W. Tsai, P. Wang, M. Xue, J.-M. Yao, W. Yu, B. Zhang, L. Zhang, S. Zhu, and W. Zhu. Magnetic field reversal in the

turbulent environment around a repeating fast radio burst. *Science*, 380(6645):599–603, May 2023. doi: 10.1126/science.abo6526.

L. S. Aramyan, A. A. Hakobyan, A. R. Petrosian, V. de Lapparent, E. Bertin, G. A. Mamon, D. Kunth, T. A. Nazaryan, V. Adibekyan, and M. Turatto. Supernovae and their host galaxies - IV. The distribution of supernovae relative to spiral arms. , 459(3):3130–3143, July 2016. doi: 10.1093/mnras/stw873.

T. Arshakian, R. Stepanov, R. Beck, M. Krause, D. Sokoloff, and P. Frick. Exploring the magnetic fields in local and distant galaxies. In *Wide Field Astronomy & Technology for the Square Kilometre Array*, page 13, Jan. 2009.

F. M. Audcent-Ross, G. R. Meurer, J. R. Audcent, S. D. Ryder, O. I. Wong, J. Phan, A. Williamson, and J. H. Kim. The radial distribution of supernovae compared to star formation tracers. , 492(1):848–862, Feb. 2020. doi: 10.1093/mnras/stz3282.

R. J. Avila, W. Hack, M. Cara, D. Borncamp, J. Mack, L. Smith, and L. Ubeda. DrizzlePac 2.0 - Introducing New Features. In A. R. Taylor and E. Rosolowsky, editors, *Astronomical Data Analysis Software an Systems XXIV (ADASS XXIV)*, volume 495 of *Astronomical Society of the Pacific Conference Series*, page 281, Sept. 2015.

K. W. Bannister, R. M. Shannon, J. P. Macquart, C. Flynn, P. G. Edwards, M. O'Neill, S. Osłowski, M. Bailes, B. Zackay, N. Clarke, L. R. D'Addario, R. Dodson, P. J. Hall, A. Jameson, D. Jones, R. Navarro, J. T. Trinh, J. Allison, C. S. Anderson, M. Bell, A. P. Chippendale, J. D. Collier, G. Heald, I. Heywood, A. W. Hotan, K. Lee-Waddell, J. P. Madrid, J. Marvil, D. McConnell, A. Popping, M. A. Voronkov, M. T. Whiting, G. R. Allen, D. C. J. Bock, D. P. Brodrick, F. Cooray, D. R. DeBoer, P. J. Diamond, R. Ekers, R. G. Gough, G. A. Hampson, L. Harvey-Smith, S. G. Hay, D. B. Hayman, C. A. Jackson, S. Johnston,

B. S. Koribalski, N. M. McClure-Griffiths, P. Mirtschin, A. Ng, R. P. Norris, S. E. Pearce, C. J. Phillips, D. N. Roxby, E. R. Troup, and T. Westmeier. The Detection of an Extremely Bright Fast Radio Burst in a Phased Array Feed Survey. , 841(1):L12, May 2017. doi: 10.3847/2041-8213/aa71ff.

K. W. Bannister, A. T. Deller, C. Phillips, J. P. Macquart, J. X. Prochaska, N. Tejos, S. D. Ryder, E. M. Sadler, R. M. Shannon, S. Simha, C. K. Day, M. McQuinn, F. O. North-Hickey, S. Bhandari, W. R. Arcus, V. N. Bennert, J. Burchett, M. Bouwhuis, R. Dodson, R. D. Ekers, W. Farah, C. Flynn, C. W. James, M. Kerr, E. Lenc, E. K. Mahony, J. O'Meara, S. Osłowski, H. Qiu, T. Treu, V. U, T. J. Bateman, D. C. J. Bock, R. J. Bolton, A. Brown, J. D. Bunton, A. P. Chippendale, F. R. Cooray, T. Cornwell, N. Gupta, D. B. Hayman, M. Kesteven, B. S. Koribalski, A. MacLeod, N. M. McClure-Griffiths, S. Neuhold, R. P. Norris, M. A. Pilawa, R. Y. Qiao, J. Reynolds, D. N. Roxby, T. W. Shimwell, M. A. Voronkov, and C. D. Wilson. A single fast radio burst localized to a massive galaxy at cosmological distance. *Science*, 365 (6453):565–570, Aug. 2019. doi: 10.1126/science.aaw5903.

O. S. Bartunov, D. Y. Tsvetkov, and I. V. Filimonova. Distribution of Supernovae Relative to Spiral Arms and H II Regions. , 106:1276, Dec. 1994. doi: 10.1086/133505.

C. G. Bassa, S. P. Tendulkar, E. A. K. Adams, N. Maddox, S. Bogdanov, G. C. Bower, S. Burke-Spolaor, B. J. Butler, S. Chatterjee, J. M. Cordes, J. W. T. Hessels, V. M. Kaspi, C. J. Law, B. Marcote, Z. Paragi, S. M. Ransom, P. Scholz, L. G. Spitler, and H. J. van Langevelde. FRB 121102 Is Coincident with a Star-forming Region in Its Host Galaxy. , 843(1):L8, July 2017. doi: 10.3847/2041-8213/aa7a0c.

R. Beck. Magnetic fields in spiral galaxies. , 24:4, Dec. 2015. doi: 10.1007/s00159-015-0084-4.

R. Beck, L. Chamandy, E. Elson, and E. G. Blackman. Synthesizing Observations and Theory

to Understand Galactic Magnetic Fields: Progress and Challenges. *Galaxies*, 8(1):4, Dec. 2019. doi: 10.3390/galaxies8010004.

E. Bertin and S. Arnouts. SExtractor: Software for source extraction. , 117:393–404, June 1996.

S. Bhandari, K. W. Bannister, E. Lenc, H. Cho, R. Ekers, C. K. Day, A. T. Deller, C. Flynn, C. W. James, J.-P. Macquart, E. K. Mahony, L. Marnoch, V. A. Moss, C. Phillips, J. X. Prochaska, H. Qiu, S. D. Ryder, R. M. Shannon, N. Tejos, and O. I. Wong. Limits on Precursor and Afterglow Radio Emission from a Fast Radio Burst in a Star-forming Galaxy. , 901(2): L20, Oct. 2020a. doi: 10.3847/2041-8213/abb462.

S. Bhandari, E. M. Sadler, J. X. Prochaska, S. Simha, S. D. Ryder, L. Marnoch, K. W. Bannister, J.-P. Macquart, C. Flynn, R. M. Shannon, N. Tejos, F. Corro-Guerra, C. K. Day, A. T. Deller, R. Ekers, S. Lopez, E. K. Mahony, C. Nuñez, and C. Phillips. The Host Galaxies and Progenitors of Fast Radio Bursts Localized with the Australian Square Kilometre Array Pathfinder. , 895(2):L37, June 2020b. doi: 10.3847/2041-8213/ab672e.

S. Bhandari, K. E. Heintz, K. Aggarwal, L. Marnoch, C. K. Day, J. Sydnor, S. Burke-Spolaor, C. J. Law, J. Xavier Prochaska, N. Tejos, K. W. Bannister, B. J. Butler, A. T. Deller, R. D. Ekers, C. Flynn, W.-f. Fong, C. W. James, T. J. W. Lazio, R. Luo, E. K. Mahony, S. D. Ryder, E. M. Sadler, R. M. Shannon, J. Han, K. Lee, and B. Zhang. Characterizing the Fast Radio Burst Host Galaxy Population and its Connection to Transients in the Local and Extragalactic Universe. , 163(2):69, Feb. 2022. doi: 10.3847/1538-3881/ac3aec.

S. Bhandari, A. C. Gordon, D. R. Scott, L. Marnoch, N. Sridhar, P. Kumar, C. W. James, H. Qiu, K. W. Bannister, A. T. Deller, T. Eftekhari, W.-f. Fong, M. Glowacki, J. X. Prochaska, S. D. Ryder, R. M. Shannon, and S. Simha. A Nonrepeating Fast Radio Burst in a Dwarf Host Galaxy. , 948(1):67, May 2023. doi: 10.3847/1538-4357/acc178.

M. Bhardwaj, B. M. Gaensler, V. M. Kaspi, T. L. Landecker, R. Mckinven, D. Michilli, Z. Pleunis, S. P. Tendulkar, B. C. Andersen, P. J. Boyle, T. Cassanelli, P. Chawla, A. Cook, M. Dobbs, E. Fonseca, J. Kaczmarek, C. Leung, K. Masui, M. Mnchmeyer, C. Ng, M. Rafiei-Ravandi, P. Scholz, K. Shin, K. M. Smith, I. H. Stairs, and A. V. Zwaniga. A Nearby Repeating Fast Radio Burst in the Direction of M81. , 910(2):L18, Apr. 2021. doi: 10.3847/2041-8213/abeaa6.

P. K. Blanchard, E. Berger, and W.-f. Fong. The Offset and Host Light Distributions of Long Gamma-Ray Bursts: A New View From HST Observations of Swift Bursts. , 817(2):144, Feb. 2016. doi: 10.3847/0004-637X/817/2/144.

C. D. Bochenek, V. Ravi, K. V. Belov, G. Hallinan, J. Kocz, S. R. Kulkarni, and D. L. McKenna. A fast radio burst associated with a Galactic magnetar. , 587(7832):59–62, Nov. 2020. doi: 10.1038/s41586-020-2872-x.

C. D. Bochenek, V. Ravi, and D. Dong. Localized Fast Radio Bursts Are Consistent with Magnetar Progenitors Formed in Core-collapse Supernovae. , 907(2):L31, Feb. 2021. doi: 10.3847/2041-8213/abd634.

L. Bradley, B. Sipőcz, T. Robitaille, E. Tollerud, Z. Vinícius, C. Deil, K. Barbary, T. J. Wilson, I. Busko, H. M. Günther, M. Cara, S. Conseil, A. Bostroem, M. Droettboom, E. M. Bray, L. A. Bratholm, P. L. Lim, G. Barentsen, M. Craig, S. Pascual, G. Perren, J. Greco, A. Donath, M. de Val-Borro, W. Kerzendorf, Y. P. Bach, B. A. Weaver, F. D'Eugenio, H. Souchereau, and L. Ferreira. astropy/photutils: 1.0.0, Sept. 2020. URL `https://doi.org/10.5281/zenodo.4044744`.

D. Calzetti. The Dust Opacity of Star-forming Galaxies. , 113(790):1449–1485, Dec 2001. doi: 10.1086/324269.

E. Carretti, V. Vacca, S. P. O'Sullivan, G. H. Heald, C. Horellou, H. J. A. Röttgering, A. M. M.

Scaife, T. W. Shimwell, A. Shulevski, C. Stuardi, and T. Vernstrom. Magnetic field strength in cosmic web filaments. , 512(1):945–959, May 2022. doi: 10.1093/mnras/stac384.

K. C. Chambers, E. A. Magnier, N. Metcalfe, H. A. Flewelling, M. E. Huber, C. Z. Waters, L. Denneau, P. W. Draper, D. Farrow, D. P. Finkbeiner, C. Holmberg, J. Koppenhoefer, P. A. Price, A. Rest, R. P. Saglia, E. F. Schlafly, S. J. Smartt, W. Sweeney, R. J. Wainscoat, W. S. Burgett, S. Chastel, T. Grav, J. N. Heasley, K. W. Hodapp, R. Jedicke, N. Kaiser, R. P. Kudritzki, G. A. Luppino, R. H. Lupton, D. G. Monet, J. S. Morgan, P. M. Onaka, B. Shiao, C. W. Stubbs, J. L. Tonry, R. White, E. Bañados, E. F. Bell, R. Bender, E. J. Bernard, M. Boegner, F. Boffi, M. T. Botticella, A. Calamida, S. Casertano, W. P. Chen, X. Chen, S. Cole, N. Deacon, C. Frenk, A. Fitzsimmons, S. Gezari, V. Gibbs, C. Goessl, T. Goggia, R. Gourgue, B. Goldman, P. Grant, E. K. Grebel, N. C. Hambly, G. Hasinger, A. F. Heavens, T. M. Heckman, R. Henderson, T. Henning, M. Holman, U. Hopp, W. H. Ip, S. Isani, M. Jackson, C. D. Keyes, A. M. Koekemoer, R. Kotak, D. Le, D. Liska, K. S. Long, J. R. Lucey, M. Liu, N. F. Martin, G. Masci, B. McLean, E. Mindel, P. Misra, E. Morganson, D. N. A. Murphy, A. Obaika, G. Narayan, M. A. Nieto-Santisteban, P. Norberg, J. A. Peacock, E. A. Pier, M. Postman, N. Primak, C. Rae, A. Rai, A. Riess, A. Riffeser, H. W. Rix, S. Röser, R. Russel, L. Rutz, E. Schilbach, A. S. B. Schultz, D. Scolnic, L. Strolger, A. Szalay, S. Seitz, E. Small, K. W. Smith, D. R. Soderblom, P. Taylor, R. Thomson, A. N. Taylor, A. R. Thakar, J. Thiel, D. Thilker, D. Unger, Y. Urata, J. Valenti, J. Wagner, T. Walder, F. Walter, S. P. Watters, S. Werner, W. M. Wood-Vasey, and R. Wyse. The Pan-STARRS1 Surveys. *arXiv e-prints*, art. arXiv:1612.05560, Dec. 2016. doi: 10.48550/arXiv.1612.05560.

S. Chatterjee, C. J. Law, R. S. Wharton, S. Burke-Spolaor, J. W. T. Hessels, G. C. Bower, J. M. Cordes, S. P. Tendulkar, C. G. Bassa, P. Demorest, B. J. Butler, A. Seymour, P. Scholz, M. W. Abruzzo, S. Bogdanov, V. M. Kaspi, A. Keimpema, T. J. W. Lazio, B. Marcote, M. A.

McLaughlin, Z. Paragi, S. M. Ransom, M. Rupen, L. G. Spitler, and H. J. van Langevelde. A direct localization of a fast radio burst and its host. , 541(7635):58–61, Jan. 2017. doi: 10.1038/nature20797.

CHIME/FRB Collaboration, M. Amiri, K. Bandura, P. Berger, M. Bhardwaj, M. M. Boyce, P. J. Boyle, C. Brar, M. Burhanpurkar, P. Chawla, J. Chowdhury, J. F. Cliche, M. D. Cranmer, D. Cubranic, M. Deng, N. Denman, M. Dobbs, M. Fandino, E. Fonseca, B. M. Gaensler, U. Giri, A. J. Gilbert, D. C. Good, S. Guliani, M. Halpern, G. Hinshaw, C. Höfer, A. Josephy, V. M. Kaspi, T. L. Landecker, D. Lang, H. Liao, K. W. Masui, J. Mena-Parra, A. Naidu, L. B. Newburgh, C. Ng, C. Patel, U. L. Pen, T. Pinsonneault-Marotte, Z. Pleunis, M. Rafiei Ravandi, S. M. Ransom, A. Renard, P. Scholz, K. Sigurdson, S. R. Siegel, K. M. Smith, I. H. Stairs, S. P. Tendulkar, K. Vand erlinde, and D. V. Wiebe. The CHIME Fast Radio Burst Project: System Overview. , 863(1):48, Aug. 2018. doi: 10.3847/1538-4357/aad188.

CHIME/FRB Collaboration, B. C. Andersen, K. Bandura, M. Bhardwaj, P. Boubel, M. M. Boyce, P. J. Boyle, C. Brar, T. Cassanelli, P. Chawla, D. Cubranic, M. Deng, M. Dobbs, M. Fandino, E. Fonseca, B. M. Gaensler, A. J. Gilbert, U. Giri, D. C. Good, M. Halpern, A. S. Hill, G. Hinshaw, C. Höfer, A. Josephy, V. M. Kaspi, R. Kothes, T. L. Landecker, D. A. Lang, D. Z. Li, H. H. Lin, K. W. Masui, J. Mena-Parra, M. Merryfield, R. Mckinven, D. Michilli, N. Milutinovic, A. Naidu, L. B. Newburgh, C. Ng, C. Patel, U. Pen, T. Pinsonneault-Marotte, Z. Pleunis, M. Rafiei-Ravandi, M. Rahman, S. M. Ransom, A. Renard, P. Scholz, S. R. Siegel, S. Singh, K. M. Smith, I. H. Stairs, S. P. Tendulkar, I. Tretyakov, K. Vanderlinde, P. Yadav, and A. V. Zwaniga. CHIME/FRB Discovery of Eight New Repeating Fast Radio Burst Sources. , 885(1):L24, Nov. 2019. doi: 10.3847/2041-8213/ab4a80.

CHIME/FRB Collaboration, B. C. Andersen, K. M. Bandura, M. Bhardwaj, A. Bij, M. M. Boyce, P. J. Boyle, C. Brar, T. Cassanelli, P. Chawla, T. Chen, J. F. Cliche, A. Cook, D. Cubranic,

A. P. Curtin, N. T. Denman, M. Dobbs, F. Q. Dong, M. Fandino, E. Fonseca, B. M. Gaensler, U. Giri, D. C. Good, M. Halpern, A. S. Hill, G. F. Hinshaw, C. Höfer, A. Josephy, J. W. Kania, V. M. Kaspi, T. L. Landecker, C. Leung, D. Z. Li, H. H. Lin, K. W. Masui, R. McKinven, J. Mena-Parra, M. Merryfield, B. W. Meyers, D. Michilli, N. Milutinovic, A. Mirhosseini, M. Münchmeyer, A. Naidu, L. B. Newburgh, C. Ng, C. Patel, U. L. Pen, T. Pinsonneault-Marotte, Z. Pleunis, B. M. Quine, M. Rafiei-Ravandi, M. Rahman, S. M. Ransom, A. Renard, P. Sanghavi, P. Scholz, J. R. Shaw, K. Shin, S. R. Siegel, S. Singh, R. J. Smegal, K. M. Smith, I. H. Stairs, C. M. Tan, S. P. Tendulkar, I. Tretyakov, K. Vanderlinde, H. Wang, D. Wulf, and A. V. Zwaniga. A bright millisecond-duration radio burst from a Galactic magnetar. , 587 (7832):54–58, Nov. 2020. doi: 10.1038/s41586-020-2863-y.

J. S. Chittidi, S. Simha, A. Mannings, J. X. Prochaska, S. D. Ryder, M. Rafelski, M. Neeleman, J.-P. Macquart, N. Tejos, R. A. Jorgenson, C. K. Day, L. Marnoch, S. Bhandari, A. T. Deller, H. Qiu, K. W. Bannister, R. M. Shannon, and K. E. Heintz. Dissecting the Local Environment of FRB 190608 in the Spiral Arm of its Host Galaxy. , 922(2):173, Dec. 2021. doi: 10.3847/1538-4357/ac2818.

J. M. Cordes and S. Chatterjee. Fast Radio Bursts: An Extragalactic Enigma. , 57:417–465, Aug. 2019. doi: 10.1146/annurev-astro-091918-104501.

J. M. Cordes and T. J. W. Lazio. NE2001. II. Using Radio Propagation Data to Construct a Model for the Galactic Distribution of Free Electrons. *ArXiv Astrophysics e-prints*, Jan. 2003.

C. K. Day, A. T. Deller, R. M. Shannon, H. Qui, J. P. Macquart, and J. X. Prochaska. High time resolution and polarisation properties of askap-localised fast radio bursts. *, in prep.*, 2020.

C. K. Day, A. T. Deller, C. W. James, E. Lenc, S. Bhandari, R. M. Shannon, and K. W.

Bannister. Astrometric accuracy of snapshot fast radio burst localisations with ASKAP. , 38: e050, Sept. 2021. doi: 10.1017/pasa.2021.40.

K. De, M. M. Kasliwal, A. Tzanidakis, U. C. Fremling, S. Adams, I. Andreoni, A. Bagdasaryan, E. C. Bellm, L. Bildsten, C. Cannella, D. O. Cook, A. r. Delacroix, A. Drake, D. Duev, A. Dugas, S. Frederick, A. Gal-Yam, D. Goldstein, V. Z. Golkhou, M. J. Graham, D. Hale, M. Hankins, G. Helou, A. Y. Q. Ho, I. Irani, J. E. Jencson, S. Kaye, S. R. Kulkarni, T. Kupfer, R. R. Laher, R. Leadbeater, R. Lunnan, F. J. Masci, A. A. Miller, J. D. Neill, E. O. Ofek, D. A. Perley, A. Polin, T. A. Prince, E. Quataert, D. Reiley, R. L. Riddle, B. Rusholme, Y. Sharma, D. L. Shupe, J. Sollerman, L. Tartaglia, R. Walters, L. Yan, and Y. Yao. The Zwicky Transient Facility Census of the Local Universe I: Systematic search for Calcium rich gap transients reveal three related spectroscopic sub-classes. *arXiv e-prints*, art. arXiv:2004.09029, Apr. 2020.

L. Dessart. A magnetar model for the hydrogen-rich super-luminous supernova iPTF14hls. , 610: L10, Feb. 2018. doi: 10.1051/0004-6361/201732402.

X. Ding, S. Birrer, T. Treu, and J. D. Silverman. Galaxy shapes of Light (GaLight): a 2D modeling of galaxy images. *arXiv e-prints*, art. arXiv:2111.08721, Nov. 2021. doi: 10.48550/arXiv.2111.08721.

Y. Dong, T. Eftekhari, W.-f. Fong, A. T. Deller, A. G. Mannings, S. Simha, N. Sridhar, M. Rafelski, A. C. Gordon, S. Bhandari, C. K. Day, K. E. Heintz, J. W. T. Hessels, J. Leja, C. W. James, C. D. Kilpatrick, E. K. Mahony, B. Marcote, B. Margalit, K. Nimmo, J. X. Prochaska, A. Rouco Escorial, S. D. Ryder, G. Schroeder, R. M. Shannon, and N. Tejos. Mapping Obscured Star Formation in the Host Galaxy of FRB 20201124A. *arXiv e-prints*, art. arXiv:2307.06995, July 2023. doi: 10.48550/arXiv.2307.06995.

L. N. Driessen, E. Barr, D. Buckley, M. Caleb, H. Chen, W. Chen, M. Gromadzki, F. Jankowski,

R. Kraan-Korteweg, M. Kramer, J. Palmerio, K. Rajwade, B. Stappers, E. Tremou, S. Vergani, P. Woudt, M. Christiaan Bezuidenhout, M. Malenta, V. Morello, S. Sanidas, M. Surnis, and R. Fender. FRB 20210405I: a nearby Fast Radio Burst localised to sub-arcsecond precision with MeerKAT. *arXiv e-prints*, art. arXiv:2302.09787, Feb. 2023. doi: 10.48550/arXiv.2302.09787.

T. Eftekhari and E. Berger. Associating Fast Radio Bursts with Their Host Galaxies. , 849(2): 162, Nov. 2017. doi: 10.3847/1538-4357/aa90b9.

T. Eftekhari, E. Berger, B. Margalit, B. D. Metzger, and P. K. G. Williams. Wandering Massive Black Holes or Analogs of the First Repeating Fast Radio Burst? , 895(2):98, June 2020. doi: 10.3847/1538-4357/ab9015.

T. Eftekhari, Y. Dong, W. Fong, V. Shah, S. Simha, B. C. Andersen, S. Andrew, M. Bhardwaj, T. Cassanelli, S. Chatterjee, D. A. Coulter, E. Fonseca, B. M. Gaensler, A. C. Gordon, J. W. T. Hessels, A. L. Ibik, R. C. Joseph, L. A. Kahinga, V. Kaspi, B. Kharel, C. D. Kilpatrick, A. E. Lanman, M. Lazda, C. Leung, C. Liu, L. Mas-Ribas, K. W. Masui, R. Mckinven, J. Mena-Parra, A. A. Miller, K. Nimmo, A. Pandhi, S. S. Patil, A. B. Pearlman, Z. Pleunis, J. X. Prochaska, M. Rafiei-Ravandi, M. Sammons, P. Scholz, K. Shin, K. Smith, and I. Stairs. The Massive and Quiescent Elliptical Host Galaxy of the Repeating Fast Radio Burst FRB 20240209A. , 979(2):L22, Feb. 2025. doi: 10.3847/2041-8213/ad9de2.

I. Evans, Neal J., M. M. Dunham, J. K. Jørgensen, M. L. Enoch, B. Merín, E. F. van Dishoeck, J. M. Alcalá, P. C. Myers, K. R. Stapelfeldt, T. L. Huard, L. E. Allen, P. M. Harvey, T. van Kempen, G. A. Blake, D. W. Koerner, L. G. Mundy, D. L. Padgett, and A. I. Sargent. The Spitzer c2d Legacy Results: Star-Formation Rates and Efficiencies; Evolution and Lifetimes. , 181(2):321–350, Apr. 2009. doi: 10.1088/0067-0049/181/2/321.

H. A. Flewelling, E. A. Magnier, K. C. Chambers, J. N. Heasley, C. Holmberg, M. E. Huber,

W. Sweeney, C. Z. Waters, A. Calamida, S. Casertano, X. Chen, D. Farrow, G. Hasinger, R. Henderson, K. S. Long, N. Metcalfe, G. Narayan, M. A. Nieto-Santisteban, P. Norberg, A. Rest, R. P. Saglia, A. Szalay, A. R. Thakar, J. L. Tonry, J. Valenti, S. Werner, R. White, L. Denneau, P. W. Draper, K. W. Hodapp, R. Jedicke, N. Kaiser, R. P. Kudritzki, P. A. Price, R. J. Wainscoat, S. Chastel, B. McLean, M. Postman, and B. Shiao. The Pan-STARRS1 Database and Data Products. , 251(1):7, Nov. 2020. doi: 10.3847/1538-4365/abb82d.

W. Fong and E. Berger. The Locations of Short Gamma-Ray Bursts as Evidence for Compact Object Binary Progenitors. , 776(1):18, Oct. 2013. doi: 10.1088/0004-637X/776/1/18.

W. Fong, E. Berger, and D. B. Fox. Hubble Space Telescope Observations of Short Gamma-Ray Burst Host Galaxies: Morphologies, Offsets, and Local Environments. , 708(1):9–25, Jan. 2010. doi: 10.1088/0004-637X/708/1/9.

G. Fragione and A. Loeb. Constraining the milky way mass with hypervelocity stars. *New Astronomy*, 55:32–38, aug 2017. doi: 10.1016/j.newast.2017.03.002. URL `https://doi.org/10.1016%2Fj.newast.2017.03.002`.

A. S. Fruchter, A. J. Levan, L. Strolger, P. M. Vreeswijk, S. E. Thorsett, D. Bersier, I. Burud, J. M. Castro Cerón, A. J. Castro-Tirado, C. Conselice, T. Dahlen, H. C. Ferguson, J. P. U. Fynbo, P. M. Garnavich, R. A. Gibbons, J. Gorosabel, T. R. Gull, J. Hjorth, S. T. Holland, C. Kouveliotou, Z. Levay, M. Livio, M. R. Metzger, P. E. Nugent, L. Petro, E. Pian, J. E. Rhoads, A. G. Riess, K. C. Sahu, A. Smette, N. R. Tanvir, R. A. M. J. Wijers, and S. E. Woosley. Long γ-ray bursts and core-collapse supernovae have different environments. , 441 (7092):463–468, May 2006. doi: 10.1038/nature04787.

B. M. Gaensler. Cosmic magnetism with the Square Kilometre Array and its pathfinders. In K. G. Strassmeier, A. G. Kosovichev, and J. E. Beckman, editors, *Cosmic Magnetic*

Fields: From Planets, to Stars and Galaxies, volume 259, pages 645–652, Apr. 2009. doi: 10.1017/S1743921309031470.

M. Glowacki, K. Lee-Waddell, A. T. Deller, N. Deg, A. C. Gordon, J. A. Grundy, L. Marnoch, A. X. Shen, S. D. Ryder, R. M. Shannon, O. I. Wong, H. Dénes, B. S. Koribalski, C. Murugeshan, J. Rhee, T. Westmeier, S. Bhandari, A. Bosma, B. W. Holwerda, and J. X. Prochaska. WALLABY Pilot Survey: H I in the Host Galaxy of a Fast Radio Burst. , 949(1):25, May 2023. doi: 10.3847/1538-4357/acc1e3.

A. C. Gordon, W.-f. Fong, C. D. Kilpatrick, T. Eftekhari, J. Leja, J. X. Prochaska, A. E. Nugent, S. Bhandari, P. K. Blanchard, M. Caleb, C. K. Day, A. T. Deller, Y. Dong, M. Glowacki, K. Gourdji, A. G. Mannings, E. K. Mahoney, L. Marnoch, A. A. Miller, K. Paterson, J. C. Rastinejad, S. D. Ryder, E. M. Sadler, D. R. Scott, H. Sears, R. M. Shannon, S. Simha, B. W. Stappers, and N. Tejos. The Demographics, Stellar Populations, and Star Formation Histories of Fast Radio Burst Host Galaxies: Implications for the Progenitors. *arXiv e-prints*, art. arXiv:2302.05465, Feb. 2023. doi: 10.48550/arXiv.2302.05465.

R. J. J. Grand, F. A. Gómez, F. Marinacci, R. Pakmor, V. Springel, D. J. R. Campbell, C. S. Frenk, A. Jenkins, and S. D. M. White. The Auriga Project: the properties and formation mechanisms of disc galaxies across cosmic time. , 467(1):179–207, May 2017. doi: 10.1093/mnras/stx071.

D. J. Griffiths. *Introduction to electrodynamics*. Pearson, 2013.

S. Hackstein, M. Brüggen, F. Vazza, B. M. Gaensler, and V. Heesen. Fast radio burst dispersion measures and rotation measures and the origin of intergalactic magnetic fields. , 488(3): 4220–4238, Sept. 2019. doi: 10.1093/mnras/stz2033.

K. E. Heintz, J. X. Prochaska, S. Simha, E. Platts, W.-f. Fong, N. Tejos, S. D. Ryder, K. Aggarwal,

S. Bhandari, C. K. Day, A. T. Deller, C. D. Kilpatrick, C. J. Law, J.-P. Macquart, A. Mannings, L. J. Marnoch, E. M. Sadler, and R. M. Shannon. Host Galaxy Properties and Offset Distributions of Fast Radio Bursts: Implications for their Progenitors. *arXiv e-prints*, art. arXiv:2009.10747, Sept. 2020.

S. Hill. Snapshot: Tattered remains of first recorded supernova captured in new image, May 2023. URL `https://www.astronomy.com/science/snapshot-tattered-remains-of-first-recorded-supernova-captured-in-new-image/`.

A. Horowicz and B. Margalit. The Host Galaxies of Fast Radio Bursts Track a Combination of Stellar Mass and Star Formation, Similar to Type Ia Supernovae. *arXiv e-prints*, art. arXiv:2504.08038, Apr. 2025. doi: 10.48550/arXiv.2504.08038.

B. Hsu, P. K. Blanchard, E. Berger, and S. Gomez. An Extensive *Hubble Space Telescope* Study of the Offset and Host Light Distributions of Type I Superluminous Supernovae. *arXiv e-prints*, art. arXiv:2308.07271, Aug. 2023. doi: 10.48550/arXiv.2308.07271.

S. Hutschenreuter and T. A. Enßlin. The Galactic Faraday depth sky revisited. , 633:A150, Jan. 2020. doi: 10.1051/0004-6361/201935479.

S. Hutschenreuter, C. S. Anderson, S. Betti, G. C. Bower, J. A. Brown, M. Brüggen, E. Carretti, T. Clarke, A. Clegg, A. Costa, S. Croft, C. Van Eck, B. M. Gaensler, F. de Gasperin, M. Haverkorn, G. Heald, C. L. H. Hull, M. Inoue, M. Johnston-Hollitt, J. Kaczmarek, C. Law, Y. K. Ma, D. MacMahon, S. A. Mao, C. Riseley, S. Roy, R. Shanahan, T. Shimwell, J. Stil, C. Sobey, S. P. O'Sullivan, C. Tasse, V. Vacca, T. Vernstrom, P. K. G. Williams, M. Wright, and T. A. Enßlin. The Galactic Faraday rotation sky 2020. , 657:A43, Jan. 2022. doi: 10.1051/0004-6361/202140486.

A. L. Ibik, M. R. Drout, B. M. Gaensler, P. Scholz, D. Michilli, M. Bhardwaj, V. M. Kaspi,

Z. Pleunis, T. Cassanelli, A. M. Cook, F. A. Dong, J. F. Kaczmarek, C. Leung, K. J. Lu, K. W. Masui, A. B. Pearlman, M. Rafiei-Ravandi, K. R. Sand, K. Shin, K. M. Smith, and I. H. Stairs. Proposed Host Galaxies of Repeating Fast Radio Burst Sources Detected by CHIME/FRB. , 961(1):99, Jan. 2024. doi: 10.3847/1538-4357/ad0893.

C. W. James, J. X. Prochaska, J. P. Macquart, F. North-Hickey, K. W. Bannister, and A. Dunning. The z–DM distribution of fast radio bursts. *arXiv e-prints*, art. arXiv:2101.08005, Jan. 2021.

C. W. James, J. X. Prochaska, J. P. Macquart, F. O. North-Hickey, K. W. Bannister, and A. Dunning. The z-DM distribution of fast radio bursts. , 509(4):4775–4802, Feb. 2022. doi: 10.1093/mnras/stab3051.

A. G. Karapetyan. Constraining Type Ia supernovae via their distances from spiral arms. , 517 (1):L132–L137, Nov. 2022. doi: 10.1093/mnrasl/slac121.

J. Kennicutt, Robert C. Star Formation in Galaxies Along the Hubble Sequence. , 36:189–232, Jan. 1998a. doi: 10.1146/annurev.astro.36.1.189.

J. Kennicutt, Robert C. The Global Schmidt Law in Star-forming Galaxies. , 498(2):541–552, May 1998b. doi: 10.1086/305588.

R. C. Kennicutt and N. J. Evans. Star Formation in the Milky Way and Nearby Galaxies. , 50: 531–608, Sept. 2012. doi: 10.1146/annurev-astro-081811-125610.

F. Kirsten, B. Marcote, K. Nimmo, J. W. T. Hessels, M. Bhardwaj, S. P. Tendulkar, A. Keimpema, J. Yang, M. P. Snelders, P. Scholz, A. B. Pearlman, C. J. Law, W. M. Peters, M. Giroletti, Z. Paragi, C. Bassa, D. M. Hewitt, U. Bach, V. Bezrukovs, M. Burgay, S. T. Buttaccio, J. E. Conway, A. Corongiu, R. Feiler, O. Forssén, M. P. Gawroński, R. Karuppusamy, M. A. Kharinov, M. Lindqvist, G. Maccaferri, A. Melnikov, O. S. Ould-Boukattine, A. Possenti, G. Surcis, N. Wang, J. Yuan, K. Aggarwal, R. Anna-Thomas, G. C. Bower, R. Blaauw,

S. Burke-Spolaor, T. Cassanelli, T. E. Clarke, E. Fonseca, B. M. Gaensler, A. Gopinath, V. M. Kaspi, N. Kassim, T. J. W. Lazio, C. Leung, D. Z. Li, H. H. Lin, K. W. Masui, R. Mckinven, D. Michilli, A. G. Mikhailov, C. Ng, A. Orbidans, U. L. Pen, E. Petroff, M. Rahman, S. M. Ransom, K. Shin, K. M. Smith, I. H. Stairs, and W. Vlemmings. A repeating fast radio burst source in a globular cluster. , 602(7898):585–589, Feb. 2022. doi: 10.1038/s41586-021-04354-w.

J. Kocz, V. Ravi, M. Catha, L. D'Addario, G. Hallinan, R. Hobbs, S. Kulkarni, J. Shi, H. Vedantham, S. Weinreb, and D. Woody. DSA-10: a prototype array for localizing fast radio bursts. , 489(1):919–927, Oct. 2019. doi: 10.1093/mnras/stz2219.

P. Kumar, R. M. Shannon, C. Flynn, S. Osłowski, S. Bhandari, C. K. Day, A. T. Deller, W. Farah, J. F. Kaczmarek, M. Kerr, C. Phillips, D. C. Price, H. Qiu, and N. Thyagarajan. Extremely band-limited repetition from a fast radio burst source. *arXiv e-prints*, art. arXiv:2009.01214, Sept. 2020.

P. Kumar, R. M. Shannon, M. E. Lower, S. Bhandari, A. T. Deller, C. Flynn, and E. F. Keane. Circularly polarized radio emission from the repeating fast radio burst source FRB 20201124A. , 512(3):3400–3413, May 2022. doi: 10.1093/mnras/stac683.

H. Kuncarayakti, J. P. Anderson, L. Galbany, K. Maeda, M. Hamuy, G. Aldering, N. Arimoto, M. Doi, T. Morokuma, and T. Usuda. Constraints on core-collapse supernova progenitors from explosion site integral field spectroscopy. , 613:A35, May 2018. doi: 10.1051/0004-6361/201731923.

K. Labrie, K. Anderson, R. Cárdenes, C. Simpson, and J. E. H. Turner. DRAGONS - Data Reduction for Astronomy from Gemini Observatory North and South. In P. J. Teuben, M. W. Pound, B. A. Thomas, and E. M. Warner, editors, *Astronomical Data Analysis Software and*

Systems XXVII, volume 523 of *Astronomical Society of the Pacific Conference Series*, page 321, Oct. 2019.

C. J. Lada and T. M. Dame. The Mass-Size Relation and the Constancy of GMC Surface Densities in the Milky Way. , 898(1):3, July 2020. doi: 10.3847/1538-4357/ab9bfb.

T.-W. Lan and J. X. Prochaska. Constraining magnetic fields in the circumgalactic medium. , 496(3):3142–3151, Aug. 2020. doi: 10.1093/mnras/staa1750.

C. J. Law, B. J. Butler, J. X. Prochaska, B. Zackay, S. Burke-Spolaor, A. Mannings, N. Tejos, A. Josephy, B. Andersen, P. Chawla, K. E. Heintz, K. Aggarwal, G. C. Bower, P. B. Demorest, C. D. Kilpatrick, T. J. W. Lazio, J. Linford, R. Mckinven, S. Tendulkar, and S. Simha. A Distant Fast Radio Burst Associated with Its Host Galaxy by the Very Large Array. , 899(2): 161, Aug. 2020. doi: 10.3847/1538-4357/aba4ac.

C. J. Law, K. Sharma, V. Ravi, G. Chen, M. Catha, L. Connor, J. T. Faber, G. Hallinan, C. Harnach, G. Hellbourg, R. Hobbs, D. Hodge, M. Hodges, J. W. Lamb, P. Rasmussen, M. B. Sherman, J. Shi, D. Simard, R. Squillace, S. Weinreb, D. P. Woody, and N. Yadlapalli. Deep Synoptic Array Science: First FRB and Host Galaxy Catalog. *arXiv e-prints*, art. arXiv:2307.03344, July 2023. doi: 10.48550/arXiv.2307.03344.

G. Leloudas, S. Schulze, T. Krühler, J. Gorosabel, L. Christensen, A. Mehner, A. de Ugarte Postigo, R. Amorín, C. C. Thöne, J. P. Anderson, F. E. Bauer, A. Gallazzi, K. G. Hełminiak, J. Hjorth, E. Ibar, D. Malesani, N. Morell, J. Vinko, and J. C. Wheeler. Spectroscopy of superluminous supernova host galaxies. A preference of hydrogen-poor events for extreme emission line galaxies. , 449(1):917–932, May 2015. doi: 10.1093/mnras/stv320.

C. Leung, J. Mena-Parra, K. Masui, K. Bandura, M. Bhardwaj, P. J. Boyle, C. Brar, M. Bruneault, T. Cassanelli, D. Cubranic, J. F. Kaczmarek, V. Kaspi, T. Landecker, D. Michilli, N. Milutinovic,

C. Patel, Z. Pleunis, M. Rahman, A. Renard, P. Sanghavi, I. H. Stairs, P. Scholz, K. Vanderlinde, and Chime/Frb Collaboration. A Synoptic VLBI Technique for Localizing Nonrepeating Fast Radio Bursts with CHIME/FRB. , 161(2):81, Feb. 2021. doi: 10.3847/1538-3881/abd174.

Y. Li, B. Zhang, K. Nagamine, and J. Shi. The FRB 121102 Host Is Atypical among Nearby Fast Radio Bursts. , 884(1):L26, Oct. 2019. doi: 10.3847/2041-8213/ab3e41.

T. C. Licquia and J. A. Newman. Improved Estimates of the Milky Way's Stellar Mass and Star Formation Rate from Hierarchical Bayesian Meta-Analysis. , 806(1):96, June 2015. doi: 10.1088/0004-637X/806/1/96.

S. Lim, E. W. Peng, P. Côté, L. Ferrarese, J. C. Roediger, C. Liu, C. Spengler, E. Sola, P.-A. Duc, L. V. Sales, J. P. Blakeslee, J.-C. Cuillandre, P. R. Durrell, E. Emsellem, S. D. J. Gwyn, A. Lançon, F. R. Marleau, J. C. Mihos, O. Müller, T. H. Puzia, and R. Sánchez-Janssen. The Next Generation Virgo Cluster Survey (NGVS). XXVII. The Size and Structure of Globular Cluster Systems and Their Connection to Dark Matter Halos. , 966(2):168, May 2024. doi: 10.3847/1538-4357/ad3444.

C. C. Lin, C. Yuan, and F. H. Shu. On the Spiral Structure of Disk Galaxies. III. Comparison with Observations. , 155:721, Mar. 1969. doi: 10.1086/149907.

D. R. Lorimer, M. Bailes, M. A. McLaughlin, D. J. Narkevic, and F. Crawford. A Bright Millisecond Radio Burst of Extragalactic Origin. *Science*, 318(5851):777, Nov. 2007. doi: 10.1126/science.1147532.

R. Lunnan, R. Chornock, E. Berger, A. Rest, W. Fong, D. Scolnic, D. O. Jones, A. M. Soderberg, P. M. Challis, M. R. Drout, R. J. Foley, M. E. Huber, R. P. Kirshner, C. Leibler, G. H. Marion, M. McCrum, D. Milisavljevic, G. Narayan, N. E. Sanders, S. J. Smartt, K. W. Smith, J. L. Tonry, W. S. Burgett, K. C. Chambers, H. Flewelling, R. P. Kudritzki, R. J. Wainscoat, and

C. Waters. Zooming In on the Progenitors of Superluminous Supernovae With the HST. , 804 (2):90, May 2015. doi: 10.1088/0004-637X/804/2/90.

R. Lunnan, M. M. Kasliwal, Y. Cao, L. Hangard, O. Yaron, J. T. Parrent, C. McCully, A. Gal-Yam, J. S. Mulchaey, S. Ben-Ami, A. V. Filippenko, C. Fremling, A. S. Fruchter, D. A. Howell, J. Koda, T. Kupfer, S. R. Kulkarni, R. Laher, F. Masci, P. E. Nugent, E. O. Ofek, M. Yagi, and L. Yan. Two New Calcium-rich Gap Transients in Group and Cluster Environments. , 836(1):60, Feb. 2017. doi: 10.3847/1538-4357/836/1/60.

J.-P. Macquart, M. Bailes, N. D. R. Bhat, G. C. Bower, J. D. Bunton, S. Chatterjee, T. Colegate, J. M. Cordes, L. D'Addario, A. Deller, R. Dodson, R. Fender, K. Haines, P. Halll, C. Harris, A. Hotan, S. Johnston, D. L. Jones, M. Keith, J. Y. Koay, T. J. W. Lazio, W. Majid, T. Murphy, R. Navarro, C. Phillips, P. Quinn, R. A. Preston, B. Stansby, I. Stairs, B. Stappers, L. Staveley-Smith, S. Tingay, D. Thompson, W. van Straten, K. Wagstaff, M. Warren, R. Wayth, L. Wen, and CRAFT Collaboration. The Commensal Real-Time ASKAP Fast-Transients (CRAFT) Survey. *Publications of the Astronomical Society of Australia*, 27(3):272–282, June 2010. doi: 10.1071/AS09082.

J. P. Macquart, E. Keane, K. Grainge, M. McQuinn, R. Fender, J. Hessels, A. Deller, R. Bhat, R. Breton, S. Chatterjee, C. Law, D. Lorimer, E. O. Ofek, M. Pietka, L. Spitler, B. Stappers, and C. Trott. Fast Transients at Cosmological Distances with the SKA. In *Advancing Astrophysics with the Square Kilometre Array (AASKA14)*, page 55, Apr. 2015.

J. P. Macquart, J. X. Prochaska, M. McQuinn, K. W. Bannister, S. Bhandari, C. K. Day, A. T. Deller, R. D. Ekers, C. W. James, L. Marnoch, S. Osłowski, C. Phillips, S. D. Ryder, D. R. Scott, R. M. Shannon, and N. Tejos. A census of baryons in the Universe from localized fast radio bursts. , 581(7809):391–395, May 2020. doi: 10.1038/s41586-020-2300-2.

A. G. Mannings, W.-f. Fong, S. Simha, J. X. Prochaska, M. Rafelski, C. D. Kilpatrick, N. Tejos, K. E. Heintz, K. W. Bannister, S. Bhandari, C. K. Day, A. T. Deller, S. D. Ryder, R. M. Shannon, and S. P. Tendulkar. A High-resolution View of Fast Radio Burst Host Environments. , 917(2):75, Aug. 2021. doi: 10.3847/1538-4357/abff56.

B. Marcote, Z. Paragi, J. W. T. Hessels, A. Keimpema, H. J. van Langevelde, Y. Huang, C. G. Bassa, S. Bogdanov, G. C. Bower, S. Burke-Spolaor, B. J. Butler, R. M. Campbell, S. Chatterjee, J. M. Cordes, P. Demorest, M. A. Garrett, T. Ghosh, V. M. Kaspi, C. J. Law, T. J. W. Lazio, M. A. McLaughlin, S. M. Ransom, C. J. Salter, P. Scholz, A. Seymour, A. Siemion, L. G. Spitler, S. P. Tendulkar, and R. S. Wharton. The Repeating Fast Radio Burst FRB 121102 as Seen on Milliarcsecond Angular Scales. , 834(2):L8, Jan. 2017. doi: 10.3847/2041-8213/834/2/L8.

B. Marcote, K. Nimmo, J. W. T. Hessels, S. P. Tendulkar, C. G. Bassa, Z. Paragi, A. Keimpema, M. Bhardwaj, R. Karuppusamy, V. M. Kaspi, C. J. Law, D. Michilli, K. Aggarwal, B. Andersen, A. M. Archibald, K. Bandura, G. C. Bower, P. J. Boyle, C. Brar, S. Burke-Spolaor, B. J. Butler, T. Cassanelli, P. Chawla, P. Demorest, M. Dobbs, E. Fonseca, U. Giri, D. C. Good, K. Gourdji, A. Josephy, A. Y. Kirichenko, F. Kirsten, T. L. Landecker, D. Lang, T. J. W. Lazio, D. Z. Li, H. H. Lin, J. D. Linford, K. Masui, J. Mena-Parra, A. Naidu, C. Ng, C. Patel, U. L. Pen, Z. Pleunis, M. Rafiei-Ravandi, M. Rahman, A. Renard, P. Scholz, S. R. Siegel, K. M. Smith, I. H. Stairs, K. Vanderlinde, and A. V. Zwaniga. A repeating fast radio burst source localized to a nearby spiral galaxy. , 577(7789):190–194, Jan. 2020. doi: 10.1038/s41586-019-1866-z.

B. Margalit and B. D. Metzger. A Concordance Picture of FRB 121102 as a Flaring Magnetar Embedded in a Magnetized Ion-Electron Wind Nebula. , 868(1):L4, Nov. 2018. doi: 10.3847/2041-8213/aaedad.

B. Margalit, E. Berger, and B. D. Metzger. Fast Radio Bursts from Magnetars Born in

Binary Neutron Star Mergers and Accretion Induced Collapse. , 886(2):110, Dec. 2019. doi: 10.3847/1538-4357/ab4c31.

E. C. Martin, A. J. Skemer, M. V. Radovan, S. L. Allen, D. Black, W. T. S. Deich, J. J. Fortney, G. Kruglikov, N. MacDonald, D. Marques, E. C. Morris, A. C. Phillips, D. Sandford, J. Villalobos Valencia, J. J. Wang, and P. Zachary. The Planet as Exoplanet Analog Spectrograph (PEAS): design and first-light. In *Society of Photo-Optical Instrumentation Engineers (SPIE) Conference Series*, volume 11447 of *Society of Photo-Optical Instrumentation Engineers (SPIE) Conference Series*, page 114470T, Dec. 2020. doi: 10.1117/12.2560706.

T. Matsumoto, B. D. Metzger, and J. A. Goldberg. Long Plateau Doth So: How Internal Heating Sources Affect Hydrogen-rich Supernova Light Curves. , 978(1):56, Jan. 2025. doi: 10.3847/1538-4357/ad93a9.

R. Mckinven, D. Michilli, K. Masui, D. Cubranic, B. M. Gaensler, C. Ng, M. Bhardwaj, C. Leung, P. J. Boyle, C. Brar, T. Cassanelli, D. Li, J. Mena-Parra, M. Rahman, and I. H. Stairs. Polarization Pipeline for Fast Radio Bursts Detected by CHIME/FRB. , 920(2):138, Oct. 2021. doi: 10.3847/1538-4357/ac126a.

D. Michilli, A. Seymour, J. W. T. Hessels, L. G. Spitler, V. Gajjar, A. M. Archibald, G. C. Bower, S. Chatterjee, J. M. Cordes, K. Gourdji, G. H. Heald, V. M. Kaspi, C. J. Law, C. Sobey, E. A. K. Adams, C. G. Bassa, S. Bogdanov, C. Brinkman, P. Demorest, F. Fernandez, G. Hellbourg, T. J. W. Lazio, R. S. Lynch, N. Maddox, B. Marcote, M. A. McLaughlin, Z. Paragi, S. M. Ransom, P. Scholz, A. P. V. Siemion, S. P. Tendulkar, P. van Rooy, R. S. Wharton, and D. Whitlow. An extreme magneto-ionic environment associated with the fast radio burst source FRB 121102. , 553(7687):182–185, Jan. 2018. doi: 10.1038/nature25149.

J. Moustakas, A. L. Coil, J. Aird, M. R. Blanton, R. J. Cool, D. J. Eisenstein, A. J. Mendez,

K. C. Wong, G. Zhu, and S. Arnouts. PRIMUS: Constraints on Star Formation Quenching and Galaxy Merging, and the Evolution of the Stellar Mass Function from z = 0-1. , 767(1): 50, Apr. 2013. doi: 10.1088/0004-637X/767/1/50.

M. Nicholl, E. Berger, R. Margutti, P. K. Blanchard, D. Milisavljevic, P. Challis, B. D. Metzger, and R. Chornock. An Ultraviolet Excess in the Superluminous Supernova Gaia16apd Reveals a Powerful Central Engine. , 835(1):L8, Jan. 2017a. doi: 10.3847/2041-8213/aa56c5.

M. Nicholl, P. K. G. Williams, E. Berger, V. A. Villar, K. D. Alexander, T. Eftekhari, and B. D. Metzger. Empirical Constraints on the Origin of Fast Radio Bursts: Volumetric Rates and Host Galaxy Demographics as a Test of Millisecond Magnetar Connection. , 843(2):84, July 2017b. doi: 10.3847/1538-4357/aa794d.

C. H. Niu, K. Aggarwal, D. Li, X. Zhang, S. Chatterjee, C. W. Tsai, W. Yu, C. J. Law, S. Burke-Spolaor, J. M. Cordes, Y. K. Zhang, S. K. Ocker, J. M. Yao, P. Wan, Y. Feng, Y. Niino, C. Bochenek, M. Cruces, L. Connor, J. A. Jiang, S. Dai, R. Luo, G. D. Li, C. C. Miao, J. R. Niu, R. Anna-Thomas, J. Sydnor, D. Stern, W. Y. Wang, M. Yuan, Y. L. Yue, D. J. Zhou, Z. Yan, W. W. Zhu, and B. Zhang. A repeating fast radio burst associated with a persistent radio source. , 606(7916):873–877, June 2022. doi: 10.1038/s41586-022-04755-5.

S. K. Ocker, J. M. Cordes, and S. Chatterjee. Constraining Galaxy Halos from the Dispersion and Scattering of Fast Radio Bursts and Pulsars. , 911(2):102, Apr. 2021. doi: 10.3847/1538-4357/abeb6e.

S. A. Olausen and V. M. Kaspi. The McGill Magnetar Catalog. , 212(1):6, May 2014. doi: 10.1088/0067-0049/212/1/6.

Oppermann, N., Junklewitz, H., Robbers, G., Bell, M. R., Enßlin, T. A., Bonafede, A., Braun, R., Brown, J. C., Clarke, T. E., Feain, I. J., Gaensler, B. M., Hammond, A., Harvey-Smith, L.,

Heald, G., Johnston-Hollitt, M., Klein, U., Kronberg, P. P., Mao, S. A., McClure-Griffiths, N. M., O´Sullivan, S. P., Pratley, L., Robishaw, T., Roy, S., Schnitzeler, D. H. F. M., Sotomayor-Beltran, C., Stevens, J., Stil, J. M., Sunstrum, C., Tanna, A., Taylor, A. R., and Van Eck, C. L. An improved map of the galactic faraday sky. *A&A*, 542:A93, 2012. doi: 10.1051/0004-6361/201118526. URL https://doi.org/10.1051/0004-6361/201118526.

S. P. O'Sullivan, M. Brüggen, F. Vazza, E. Carretti, N. T. Locatelli, C. Stuardi, V. Vacca, T. Vernstrom, G. Heald, C. Horellou, T. W. Shimwell, M. J. Hardcastle, C. Tasse, and H. Röttgering. New constraints on the magnetization of the cosmic web using LOFAR Faraday rotation observations. , 495(3):2607–2619, July 2020. doi: 10.1093/mnras/staa1395.

R. Pakmor and V. Springel. Simulations of magnetic fields in isolated disc galaxies. , 432(1): 176–193, June 2013. doi: 10.1093/mnras/stt428.

R. Pakmor, A. Bauer, and V. Springel. Magnetohydrodynamics on an unstructured moving grid. , 418(2):1392–1401, Dec. 2011. doi: 10.1111/j.1365-2966.2011.19591.x.

R. Pakmor, F. Marinacci, and V. Springel. Magnetic Fields in Cosmological Simulations of Disk Galaxies. , 783(1):L20, Mar. 2014. doi: 10.1088/2041-8205/783/1/L20.

R. Pakmor, V. Springel, A. Bauer, P. Mocz, D. J. Munoz, S. T. Ohlmann, K. Schaal, and C. Zhu. Improving the convergence properties of the moving-mesh code AREPO. , 455(1):1134–1143, Jan. 2016. doi: 10.1093/mnras/stv2380.

R. Pakmor, F. A. Gómez, R. J. J. Grand, F. Marinacci, C. M. Simpson, V. Springel, D. J. R. Campbell, C. S. Frenk, T. Guillet, C. Pfrommer, and S. D. M. White. Magnetic field formation in the Milky Way like disc galaxies of the Auriga project. , 469(3):3185–3199, Aug. 2017. doi: 10.1093/mnras/stx1074.

R. Pakmor, T. Guillet, C. Pfrommer, F. A. Gómez, R. J. J. Grand, F. Marinacci, C. M. Simpson, and V. Springel. Faraday rotation maps of disc galaxies. , 481(4):4410–4418, Dec. 2018. doi: 10.1093/mnras/sty2601.

R. Pakmor, F. van de Voort, R. Bieri, F. A. Gómez, R. J. J. Grand, T. Guillet, F. Marinacci, C. Pfrommer, C. M. Simpson, and V. Springel. Magnetizing the circumgalactic medium of disc galaxies. , 498(3):3125–3137, Nov. 2020. doi: 10.1093/mnras/staa2530.

J. T. Palmerio, S. D. Vergani, R. Salvaterra, R. L. Sanders, J. Japelj, A. Vidal-García, P. D'Avanzo, D. Corre, D. A. Perley, A. E. Shapley, S. Boissier, J. Greiner, E. Le Floc'h, and P. Wiseman. Are long gamma-ray bursts biased tracers of star formation? Clues from the host galaxies of the Swift/BAT6 complete sample of bright LGRBs. III. Stellar masses, star formation rates, and metallicities at z ¿ 1. , 623:A26, Mar. 2019. doi: 10.1051/0004-6361/201834179.

A. Pandhi, S. Hutschenreuter, J. L. West, B. M. Gaensler, and A. Stock. A method for reconstructing the Galactic magnetic field using dispersion of fast radio bursts and Faraday rotation of radio galaxies. , 516(4):4739–4759, Nov. 2022. doi: 10.1093/mnras/stac2314.

I. Pastor-Marazuela, J. van Leeuwen, A. Bilous, L. Connor, Y. Maan, L. Oostrum, E. Petroff, D. Vohl, K. M. Hess, E. Orrù, A. Sclocco, and Y. Wang. Comprehensive analysis of the Apertif fast radio burst sample: Similarities with young energetic neutron stars. , 693:A279, Jan. 2025. doi: 10.1051/0004-6361/202450953.

R. F. Peletier and M. Balcells. Ages of Galaxies Bulges and Disks From Optical and Near-Infrared Colors. , 111:2238, June 1996. doi: 10.1086/117958.

C. Y. Peng, L. C. Ho, C. D. Impey, and H.-W. Rix. Detailed Decomposition of Galaxy Images. II. Beyond Axisymmetric Models. , 139(6):2097–2129, June 2010. doi: 10.1088/0004-6256/139/6/2097.

D. A. Perley, R. M. Quimby, L. Yan, P. M. Vreeswijk, A. De Cia, R. Lunnan, A. Gal-Yam, O. Yaron, A. V. Filippenko, M. L. Graham, R. Laher, and P. E. Nugent. Host-galaxy Properties of 32 Low-redshift Superluminous Supernovae from the Palomar Transient Factory. , 830(1): 13, Oct. 2016. doi: 10.3847/0004-637X/830/1/13.

E. Petroff, J. W. T. Hessels, and D. R. Lorimer. Fast radio bursts. , 27(1):4, May 2019. doi: 10.1007/s00159-019-0116-6.

A. L. Piro and B. M. Gaensler. The Dispersion and Rotation Measure of Supernova Remnants and Magnetized Stellar Winds: Application to Fast Radio Bursts. , 861(2):150, July 2018. doi: 10.3847/1538-4357/aac9bc.

Planck Collaboration, P. A. R. Ade, N. Aghanim, M. Arnaud, M. Ashdown, J. Aumont, C. Baccigalupi, A. J. Banday, R. B. Barreiro, J. G. Bartlett, and et al. Planck 2015 results. XIII. Cosmological parameters. , 594:A13, Sept. 2016. doi: 10.1051/0004-6361/201525830.

E. Platts, A. Weltman, A. Walters, S. P. Tendulkar, J. E. B. Gordin, and S. Kandhai. A living theory catalogue for fast radio bursts. , 821:1–27, Aug. 2019. doi: 10.1016/j.physrep.2019.06.003.

Z. Pleunis, D. C. Good, V. M. Kaspi, R. Mckinven, S. M. Ransom, P. Scholz, K. Bandura, M. Bhardwaj, P. J. Boyle, C. Brar, T. Cassanelli, P. Chawla, F. (Adam) Dong, E. Fonseca, B. M. Gaensler, A. Josephy, J. F. Kaczmarek, C. Leung, H.-H. Lin, K. W. Masui, J. Mena-Parra, D. Michilli, C. Ng, C. Patel, M. Rafiei-Ravandi, M. Rahman, P. Sanghavi, K. Shin, K. M. Smith, I. H. Stairs, and S. P. Tendulkar. Fast Radio Burst Morphology in the First CHIME/FRB Catalog. , 923(1):1, Dec. 2021. doi: 10.3847/1538-4357/ac33ac.

H. Pour-Imani, D. Kennefick, J. Kennefick, B. L. Davis, D. W. Shields, and M. Shameer Abdeen. Strong Evidence for the Density-wave Theory of Spiral Structure in Disk Galaxies. , 827(1): L2, Aug. 2016. doi: 10.3847/2041-8205/827/1/L2.

J. L. Prieto, K. Z. Stanek, and J. F. Beacom. Characterizing Supernova Progenitors via the Metallicities of their Host Galaxies, from Poor Dwarfs to Rich Spirals. , 673(2):999–1008, Feb. 2008. doi: 10.1086/524654.

J. X. Prochaska and Y. Zheng. Probing Galactic haloes with fast radio bursts. , 485:648–665, May 2019. doi: 10.1093/mnras/stz261.

J. X. Prochaska, J.-P. Macquart, M. McQuinn, S. Simha, R. M. Shannon, C. K. Day, L. Marnoch, S. Ryder, A. Deller, K. W. Bannister, S. Bhandari, R. Bordoloi, J. Bunton, H. Cho, C. Flynn, E. K. Mahony, C. Phillips, H. Qiu, and N. Tejos. The low density and magnetization of a massive galaxy halo exposed by a fast radio burst. *Science*, 366(6462):231–234, Oct. 2019a. doi: 10.1126/science.aay0073.

J. X. Prochaska, J.-P. Macquart, M. McQuinn, S. Simha, R. M. Shannon, C. K. Day, L. Marnoch, S. Ryder, A. Deller, K. W. Bannister, S. Bhandari, R. Bordoloi, J. Bunton, H. Cho, C. Flynn, E. K. Mahony, C. Phillips, H. Qiu, and N. Tejos. The low density and magnetization of a massive galaxy halo exposed by a fast radio burst. *Science*, 366(6462):231–234, Oct. 2019b. doi: 10.1126/science.aay0073.

J. X. Prochaska, M. Neeleman, N. Kanekar, and M. Rafelski. ALMA C II 158 μm Imaging of an H I-selected Major Merger at z $\sim$ 4. , 886(2):L35, Dec. 2019c. doi: 10.3847/2041-8213/ab55eb.

J. X. Prochaska, S. Simha, C. Law, N. Tejos, and mneeleman. Frbs/frb: First doi release of this repository, Sept. 2019. URL `https://doi.org/10.5281/zenodo.3403651`.

J. X. Prochaska, J. Hennawi, R. Cooke, K. Westfall, F. Wang, EmAstro, Tiffanyhsyu, A. Wasserman, A. Villaume, Marijana777, J. Schindler, D. Young, S. Simha, M. Wilde, N. Tejos, J. Isbell, A. Flörs, N. Sandford, Z. Vasović, E. Betts, and B. Holden. pypeit/PypeIt: Release 1.0.0, Apr. 2020.

J. X. Prochaska, J. F. Hennawi, K. B. Westfall, R. J. Cooke, F. Wang, T. Hsyu, F. B. Davies, E. P. Farina, and D. Pelliccia. Pypeit: The python spectroscopic data reduction pipeline. *Journal of Open Source Software*, 5(56):2308, 2020. doi: 10.21105/joss.02308. URL `https://doi.org/10.21105/joss.02308`.

H. Qiu, R. M. Shannon, W. Farah, J.-P. Macquart, A. T. Deller, K. W. Bannister, C. W. James, C. Flynn, C. K. Day, S. Bhandari, and T. Murphy. A population analysis of pulse broadening in ASKAP fast radio bursts. , 497(2):1382–1390, Sept. 2020. doi: 10.1093/mnras/staa1916.

M. Rafelski, H. I. Teplitz, J. P. Gardner, D. Coe, N. A. Bond, A. M. Koekemoer, N. Grogin, P. Kurczynski, E. J. McGrath, M. Bourque, H. Atek, T. M. Brown, J. W. Colbert, A. Codoreanu, H. C. Ferguson, S. L. Finkelstein, E. Gawiser, M. Giavalisco, C. Gronwall, D. J. Hanish, K.-S. Lee, V. Mehta, D. F. de Mello, S. Ravindranath, R. E. Ryan, C. Scarlata, B. Siana, E. Soto, and E. N. Voyer. UVUDF: Ultraviolet Through Near-infrared Catalog and Photometric Redshifts of Galaxies in the Hubble Ultra Deep Field. , 150(1):31, July 2015. doi: 10.1088/0004-6256/150/1/31.

V. Ravi, R. M. Shannon, M. Bailes, K. Bannister, S. Bhandari, N. D. R. Bhat, S. Burke-Spolaor, M. Caleb, C. Flynn, A. Jameson, S. Johnston, E. F. Keane, M. Kerr, C. Tiburzi, A. V. Tuntsov, and H. K. Vedantham. The magnetic field and turbulence of the cosmic web measured using a brilliant fast radio burst. *Science*, 354(6317):1249–1252, Dec. 2016. doi: 10.1126/science.aaf6807.

R. J. Reynolds. Pulsar dispersion measures and Halpha emission measures: limits on the electron density and filling factor for the ionized interstellar gas. , 216:433–439, Sept. 1977. doi: 10.1086/155484.

L. F. S. Rodrigues, L. Chamandy, A. Shukurov, C. M. Baugh, and A. R. Taylor. Evolution of

galactic magnetic fields. *Monthly Notices of the Royal Astronomical Society*, 483(2):2424–2440, 11 2018. ISSN 0035-8711. doi: 10.1093/mnras/sty3270. URL https://doi.org/10.1093/mnras/sty3270.

S. D. Ryder, K. W. Bannister, S. Bhandari, A. T. Deller, R. D. Ekers, M. Glowacki, A. C. Gordon, K. Gourdji, C. W. James, C. D. Kilpatrick, W. Lu, L. Marnoch, V. A. Moss, J. X. Prochaska, H. Qiu, E. M. Sadler, S. Simha, M. W. Sammons, D. R. Scott, N. Tejos, and R. M. Shannon. A luminous fast radio burst that probes the Universe at redshift 1. *Science*, 382 (6668):294–299, Oct. 2023. doi: 10.1126/science.adf2678.

M. Safarzadeh, J. X. Prochaska, K. E. Heintz, and W.-f. Fong. Confronting the Magnetar Interpretation of Fast Radio Bursts Through Their Host Galaxy Demographics. *arXiv e-prints*, art. arXiv:2009.11735, Sept. 2020.

S. Schulze, O. Yaron, J. Sollerman, G. Leloudas, A. Gal, A. H. Wright, R. Lunnan, A. Gal-Yam, E. O. Ofek, D. A. Perley, A. V. Filippenko, M. M. Kasliwal, S. R. Kulkarni, P. E. Nugent, R. M. Quimby, M. Sullivan, N. Linn Strothjohann, I. Arcavi, S. Ben-Ami, F. Bianco, J. S. Bloom, K. De, M. Fraser, C. U. Fremling, A. Horesh, J. Johansson, P. L. Kelly, S. Knezevic, K. Maguire, A. Nyholm, . Semeli Papadogiannakis, T. Petrushevska, A. Rubin, L. Yan, Y. Yang, S. M. Adams, F. Bufano, K. I. Clubb, R. J. Foley, Y. Green, J. Harmanen, A. Y. Q. Ho, I. M. Hook, G. Hosseinzadeh, D. A. Howell, A. K. H. Kong, R. Kotak, T. Matheson, C. McCully, D. Milisavljevic, Y.-C. Pan, D. Poznanski, I. Shivvers, and S. van Velzen. The Palomar Transient Factory Core-Collapse Supernova Host-Galaxy Sample. I. Host-Galaxy Distribution Functions and Environment-Dependence of CCSNe. *arXiv e-prints*, art. arXiv:2008.05988, Aug. 2020.

M. S. Seigar and P. A. James. A test of arm-induced star formation in spiral galaxies from near-infrared and Hα imaging. , 337(3):1113–1117, Dec. 2002. doi: 10.1046/j.1365-8711.2002.06007.x.

R. M. Shannon, J. P. Macquart, K. W. Bannister, R. D. Ekers, C. W. James, S. Osłowski, H. Qiu, M. Sammons, A. W. Hotan, M. A. Voronkov, R. J. Beresford, M. Brothers, A. J. Brown, J. D. Bunton, A. P. Chippendale, C. Haskins, M. Leach, M. Marquarding, D. McConnell, M. A. Pilawa, E. M. Sadler, E. R. Troup, J. Tuthill, M. T. Whiting, J. R. Allison, C. S. Anderson, M. E. Bell, J. D. Collier, G. Gürkan, G. Heald, and C. J. Riseley. The dispersion-brightness relation for fast radio bursts from a wide-field survey. , 562(7727):386–390, Oct. 2018. doi: 10.1038/s41586-018-0588-y.

R. M. Shannon, K. W. Bannister, A. Bera, S. Bhandari, C. K. Day, A. T. Deller, T. Dial, D. Dobie, R. D. Ekers, W. f. Fong, M. Glowacki, A. C. Gordon, K. Gourdji, A. Jaini, C. W. James, P. Kumar, E. K. Mahony, L. Marnoch, A. R. Muller, J. X. Prochaska, H. Qiu, S. D. Ryder, E. M. Sadler, D. R. Scott, N. Tejos, P. A. Uttarkar, and Y. Wang. The Commensal Real-time ASKAP Fast Transient incoherent-sum survey. *arXiv e-prints*, art. arXiv:2408.02083, Aug. 2024. doi: 10.48550/arXiv.2408.02083.

K. Sharma, V. Ravi, L. Connor, C. Law, S. K. Ocker, M. Sherman, N. Kosogorov, J. Faber, G. Hallinan, C. Harnach, G. Hellbourg, R. Hobbs, D. Hodge, M. Hodges, J. Lamb, P. Rasmussen, J. Somalwar, S. Weinreb, D. Woody, J. Leja, S. Anand, K. K. Das, Y.-J. Qin, S. Rose, D. Z. Dong, J. Miller, and Y. Yao. Preferential occurrence of fast radio bursts in massive star-forming galaxies. *Nature*, 635(8037):61–66, Nov. 2024. ISSN 1476-4687. doi: 10.1038/s41586-024-08074-9. URL `https://doi.org/10.1038/s41586-024-08074-9`.

K. J. Shen, E. Quataert, and R. Pakmor. The Progenitors of Calcium-strong Transients. , 887 (2):180, Dec. 2019. doi: 10.3847/1538-4357/ab5370.

S. Simha, J. N. Burchett, J. X. Prochaska, J. S. Chittidi, O. Elek, N. Tejos, R. Jorgenson, K. W. Bannister, S. Bhandari, C. K. Day, A. T. Deller, A. G. Forbes, J.-P. Macquart, S. D. Ryder,

and R. M. Shannon. Disentangling the Cosmic Web toward FRB 190608. , 901(2):134, Oct. 2020. doi: 10.3847/1538-4357/abafc3.

L. G. Spitler, P. Scholz, J. W. T. Hessels, S. Bogdanov, A. Brazier, F. Camilo, S. Chatterjee, J. M. Cordes, F. Crawford, J. Deneva, R. D. Ferdman, P. C. C. Freire, V. M. Kaspi, P. Lazarus, R. Lynch, E. C. Madsen, M. A. McLaughlin, C. Patel, S. M. Ransom, A. Seymour, I. H. Stairs, B. W. Stappers, J. van Leeuwen, and W. W. Zhu. A repeating fast radio burst. , 531(7593): 202–205, Mar. 2016. doi: 10.1038/nature17168.

V. Springel. E pur si muove: Galilean-invariant cosmological hydrodynamical simulations on a moving mesh. , 401(2):791–851, Jan. 2010. doi: 10.1111/j.1365-2966.2009.15715.x.

M. Sullivan, D. Le Borgne, C. J. Pritchet, A. Hodsman, J. D. Neill, D. A. Howell, R. G. Carlberg, P. Astier, E. Aubourg, D. Balam, S. Basa, A. Conley, S. Fabbro, D. Fouchez, J. Guy, I. Hook, R. Pain, N. Palanque-Delabrouille, K. Perrett, N. Regnault, J. Rich, R. Taillet, S. Baumont, J. Bronder, R. S. Ellis, M. Filiol, V. Lusset, S. Perlmutter, P. Ripoche, and C. Tao. Rates and Properties of Type Ia Supernovae as a Function of Mass and Star Formation in Their Host Galaxies. , 648(2):868–883, Sept. 2006. doi: 10.1086/506137.

K. M. Svensson, A. J. Levan, N. R. Tanvir, A. S. Fruchter, and L. G. Strolger. The host galaxies of core-collapse supernovae and gamma-ray bursts. , 405(1):57–76, June 2010. doi: 10.1111/j.1365-2966.2010.16442.x.

S. P. Tendulkar, C. G. Bassa, J. M. Cordes, G. C. Bower, C. J. Law, S. Chatterjee, E. A. K. Adams, S. Bogdanov, S. Burke-Spolaor, B. J. Butler, P. Demorest, J. W. T. Hessels, V. M. Kaspi, T. J. W. Lazio, N. Maddox, B. Marcote, M. A. McLaughlin, Z. Paragi, S. M. Ransom, P. Scholz, A. Seymour, L. G. Spitler, H. J. van Langevelde, and R. S. Wharton. The Host

Galaxy and Redshift of the Repeating Fast Radio Burst FRB 121102. , 834(2):L7, Jan. 2017. doi: 10.3847/2041-8213/834/2/L7.

S. P. Tendulkar, A. Gil de Paz, A. Y. Kirichenko, J. W. T. Hessels, M. Bhardwaj, F. Ávila, C. Bassa, P. Chawla, E. Fonseca, V. M. Kaspi, A. Keimpema, F. Kirsten, T. J. W. Lazio, B. Marcote, K. Masui, K. Nimmo, Z. Paragi, M. Rahman, D. Reverte Payá, P. Scholz, and I. Stairs. The 60-pc Environment of FRB 20180916B. *arXiv e-prints*, art. arXiv:2011.03257, Nov. 2020.

The CHIME/FRB Collaboration, :, M. Amiri, B. C. Andersen, K. Bandura, S. Berger, M. Bhardwaj, M. M. Boyce, P. J. Boyle, C. Brar, D. Breitman, T. Cassanelli, P. Chawla, T. Chen, J. F. Cliche, A. Cook, D. Cubranic, A. P. Curtin, M. Deng, M. Dobbs, Fengqiu, Dong, G. Eadie, M. Fandino, E. Fonseca, B. M. Gaensler, U. Giri, D. C. Good, M. Halpern, A. S. Hill, G. Hinshaw, A. Josephy, J. F. Kaczmarek, Z. Kader, J. W. Kania, V. M. Kaspi, T. L. Landecker, D. Lang, C. Leung, D. Li, H.-H. Lin, K. W. Masui, R. Mckinven, J. Mena-Parra, M. Merryfield, B. W. Meyers, D. Michilli, N. Milutinovic, A. Mirhosseini, M. Münchmeyer, A. Naidu, L. Newburgh, C. Ng, C. Patel, U.-L. Pen, E. Petroff, T. Pinsonneault-Marotte, Z. Pleunis, M. Rafiei-Ravandi, M. Rahman, S. M. Ransom, A. Renard, P. Sanghavi, P. Scholz, J. R. Shaw, K. Shin, S. R. Siegel, A. E. Sikora, S. Singh, K. M. Smith, I. Stairs, C. M. Tan, S. P. Tendulkar, K. Vanderlinde, H. Wang, D. Wulf, and A. V. Zwaniga. The First CHIME/FRB Fast Radio Burst Catalog. *arXiv e-prints*, art. arXiv:2106.04352, June 2021.

D. Thornton, B. Stappers, M. Bailes, B. Barsdell, S. Bates, N. D. R. Bhat, M. Burgay, S. Burke-Spolaor, D. J. Champion, P. Coster, N. D'Amico, A. Jameson, S. Johnston, M. Keith, M. Kramer, L. Levin, S. Milia, C. Ng, A. Possenti, and W. van Straten. A Population of Fast Radio Bursts at Cosmological Distances. *Science*, 341(6141):53–56, July 2013. doi: 10.1126/science.1236789.

S. A. Uddin, C. R. Burns, M. M. Phillips, N. B. Suntzeff, C. Contreras, E. Y. Hsiao, N. Morrell, L. Galbany, M. Stritzinger, P. Hoeflich, C. Ashall, A. L. Piro, W. L. Freedman, S. E. Persson, K. Krisciunas, and P. Brown. The carnegie supernova project-i: Correlation between type ia supernovae and their host galaxies from optical to near-infrared bands. *The Astrophysical Journal*, 901(2):143, oct 2020. doi: 10.3847/1538-4357/abafb7. URL `https://doi.org/10.3847/1538-4357/abafb7`.

X. Wang, L. Wang, A. V. Filippenko, T. Zhang, and X. Zhao. Evidence for Two Distinct Populations of Type Ia Supernovae. *Science*, 340(6129):170–173, Apr. 2013. doi: 10.1126/science.1231502.

R. Weinberger, V. Springel, and R. Pakmor. The AREPO Public Code Release. , 248(2):32, June 2020. doi: 10.3847/1538-4365/ab908c.

R. Wielebinski and R. Beck. *Cosmic Magnetic Fields*, volume 664. 2005. doi: 10.1007/b104621.

K. W. Willett, C. J. Lintott, S. P. Bamford, K. L. Masters, B. D. Simmons, K. R. V. Casteels, E. M. Edmondson, L. F. Fortson, S. Kaviraj, W. C. Keel, T. Melvin, R. C. Nichol, M. J. Raddick, K. Schawinski, R. J. Simpson, R. A. Skibba, A. M. Smith, and D. Thomas. Galaxy Zoo 2: detailed morphological classifications for 304 122 galaxies from the Sloan Digital Sky Survey. , 435(4):2835–2860, Nov. 2013. doi: 10.1093/mnras/stt1458.

M. N. Woodland, A. G. Mannings, J. X. Prochaska, S. D. Ryder, L. Marnoch, R. A. Jorgenson, S. Simha, N. Tejos, A. Gordon, W.-f. Fong, C. D. Kilpatrick, A. T. Deller, and M. Glowacki. The Environments of Fast Radio Bursts Viewed Using Adaptive Optics. , 973(1):64, Sept. 2024. doi: 10.3847/1538-4357/ad643c.

S. E. Woosley. Gamma-Ray Bursts from Stellar Mass Accretion Disks around Black Holes. , 405:273, Mar. 1993. doi: 10.1086/172359.

H. Xu, J. R. Niu, P. Chen, K. J. Lee, W. W. Zhu, S. Dong, B. Zhang, J. C. Jiang, B. J. Wang, J. W. Xu, C. F. Zhang, H. Fu, A. V. Filippenko, E. W. Peng, D. J. Zhou, Y. K. Zhang, P. Wang, Y. Feng, Y. Li, T. G. Brink, D. Z. Li, W. Lu, Y. P. Yang, R. N. Caballero, C. Cai, M. Z. Chen, Z. G. Dai, S. G. Djorgovski, A. Esamdin, H. Q. Gan, P. Guhathakurta, J. L. Han, L. F. Hao, Y. X. Huang, P. Jiang, C. K. Li, D. Li, H. Li, X. Q. Li, Z. X. Li, Z. Y. Liu, R. Luo, Y. P. Men, C. H. Niu, W. X. Peng, L. Qian, L. M. Song, D. Stern, A. Stockton, J. H. Sun, F. Y. Wang, M. Wang, N. Wang, W. Y. Wang, X. F. Wu, S. Xiao, S. L. Xiong, Y. H. Xu, R. X. Xu, J. Yang, X. Yang, R. Yao, Q. B. Yi, Y. L. Yue, D. J. Yu, W. F. Yu, J. P. Yuan, B. B. Zhang, S. B. Zhang, S. N. Zhang, Y. Zhao, W. K. Zheng, Y. Zhu, and J. H. Zou. A fast radio burst source at a complex magnetized site in a barred galaxy. , 609(7928):685–688, Sept. 2022. doi: 10.1038/s41586-022-05071-8.

E. Zapartas, S. E. de Mink, R. G. Izzard, S. C. Yoon, C. Badenes, Y. Götberg, A. de Koter, C. J. Neijssel, M. Renzo, A. Schootemeijer, and T. S. Shrotriya. Delay-time distribution of core-collapse supernovae with late events resulting from binary interaction. , 601:A29, May 2017. doi: 10.1051/0004-6361/201629685.

E. Zapartas, S. E. de Mink, S. Justham, N. Smith, A. de Koter, M. Renzo, I. Arcavi, R. Farmer, Y. Götberg, and S. Toonen. The diverse lives of progenitors of hydrogen-rich core-collapse supernovae: the role of binary interaction. , 631:A5, Nov. 2019. doi: 10.1051/0004-6361/201935854.

B. B. Zhang, B. Zhang, H. Sun, W. H. Lei, H. Gao, Y. Li, L. Shao, Y. Zhao, Y. D. Hu, H. J. Lü, X. F. Wu, X. L. Fan, G. Wang, A. J. Castro-Tirado, S. Zhang, B. Y. Yu, Y. Y. Cao, and E. W. Liang. A peculiar low-luminosity short gamma-ray burst from a double neutron star merger progenitor. *Nature Communications*, 9:447, Jan. 2018. doi: 10.1038/s41467-018-02847-3.

Z. Y. Zhao and F. Y. Wang. FRB 190520b embedded in a magnetar wind nebula and supernova

remnant: A luminous persistent radio source, decreasing dispersion measure, and large rotation measure. *The Astrophysical Journal Letters*, 923(1):L17, dec 2021. doi: 10.3847/2041-8213/ac3f2f. URL https://doi.org/10.3847/2041-8213/ac3f2f.

Appendix A

Planet as Exoplanet Spectrograph Throughput

A.1 Introduction

The Planet as Exoplanet Analog Spectrograph (PEAS) instrument observes disk integrated spectra of solar system planets. Because of the distance of exo-planetary systems, we observe exoplanets as point sources and spectra of these planets cover the entirety of the visible surface. In contrast, solar system planets range from arcsecond to arcminute angular sizes on the sky, meaning spectra are generally spatially resolved and only small portions of a solar system planet can be observed at once with a traditional slit-based spectrograph. Spectra of solar system planets change based on the local physics and chemistry of the observed location of the planet and thus are not directly comparable to the disk averaged spectra of exoplanets. PEAS is designed to observe solar system planets as if they are point source exoplanets. The instrument is described by Martin et al. (2020).

PEAS uses an integrating sphere to scramble the planetary light and mimic observations

of a distant point source. Many scientific gains can be made as we compare PEAS data to ground truth observations and theoretical models. PEAS data can test our ability to determine what tracers are present in the spectra that signify things such as atmospheric conditions, clouds, rings - characteristics of solar system planets that are non-trivial to resolve for exoplanets. However, the integrating sphere is a source of substantial light loss in the overall system. Here, we build an analytical model of the entire PEAS system, including the integrating sphere to determine where efficiency is lost. We then examine possible upgrades to the optical design to increase our throughput and therefore sensitivity.

A.2 PEAS Throughput

A.2.1 Building the throughput model

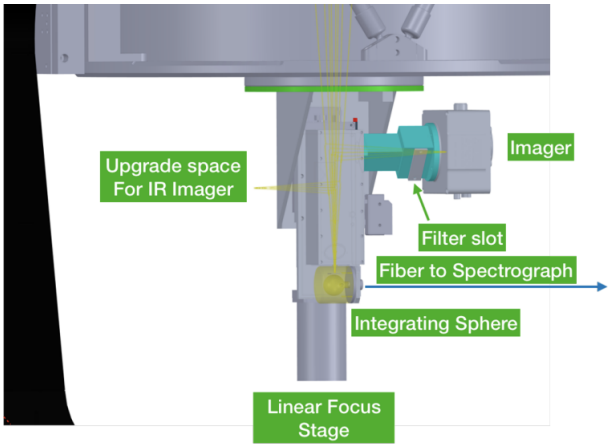

Figure A.1: A SolidWorks model of the current optical design for PEAS. The integrating sphere is responsible for the disk integration of the light that is subsequently sent to the spectrograph through a bundle of fiber optic cables.

We simulate the throughput of the entirety of the PEAS setup (Figure A.1, including

the telescope, back-end optics, and spectrograph components). In this process we account for the mirror reflectivity along with the sapphire window, integrating sphere, silver coating, grating, and quantum efficiencies. We begin with the 0.51-m Ritchey-Chrétien PlaneWave telescope [1]. The mirrors are estimated to have an aluminum coating with $\sim 96\%$ efficiency across the PEAS bandpass of $\sim$ 450-950 nm. For accuracy, we use the chromatic reflectance curve determined by testing of the PlaneWave optics coatings. The primary mirror has a size of 24 in and the secondary mirror, a size of 6.89 in. We account for the secondary mirror obstruction when determining the collecting area of the primary mirror. The light then passes through a series of four sapphire windows, with throughput curves given by Martin et al. (2020). This efficiency is wavelength dependent.

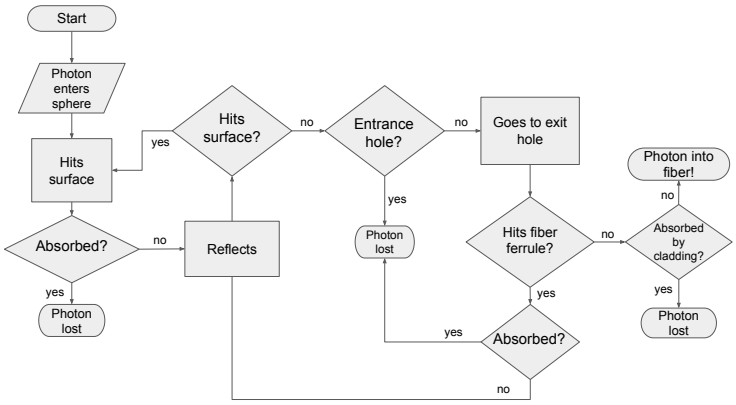

Figure A.2: This flowchart shows the possible paths for a photon as it enters the integrating sphere. The photon can be lost through absorption (by the integrating sphere surface or cladding); or leaving through the entrance hole.

[1] https://planewave.com/product/24-inch-ritchey-chretien-optical-tube-assembly/

Then, light enters the 1-in diameter integrating sphere. As seen in the flowchart in Figure A.2, we lay out the possible path of a photon entering the integrating sphere. Upon entering the sphere, the photon can either be immediately absorbed by the inner surface, or reflect. The reflectivity of the inner Spectralon coating of the sphere is quoted to be $> 99\%$ across the PEAS bandpass[2]. After reflecting, the photon will then (i) go to the exit hole, (ii) go back through the entrance hole, or (iii) hit the inner surface of the sphere once again where it will either be absorbed or reflect again. With option (i), depending on the size of the fiber ferule relative to the size of the fiber bundle, the photon may once again reflect back into the sphere or be absorbed by the aluminum coating. If the photon does make it to the fibers, depending on angle of impact, the photon can either be absorbed by the fiber cladding or make its way through the fiber to the spectrograph. The fiber acceptance area, or étendue, is:

$$étendue = (\frac{\pi^2}{4})\mathrm{d_{core}}^2\mathrm{NA}^2 \tag{A.1}$$

where NA is the numerical aperture of the fiber optic cables and d_{core} is the diameter of the fiber core. The probability of a photon making its way into a fiber is then the ratio between this area and the inner surface area of the upper hemisphere of the integrating sphere. We must also take into account the ratio between the area of the cladding and the area of the fiber, as it is still possible that a photon may satisfy the angle of entry requirement but hits the cladding surface rather than the fiber. The fiber bundle includes 91 total fibers, each with 120 micron core and a 150 micron outer diameter. Thirty of these 91 fibers form a pseudo-slit and send light into the spectrograph.

We run 10^6 photons through our probabilistic integrating sphere model to determine the relative rates of absorption and exitance. The resulting efficiency for light entering the fiber bundle from the integrating sphere is $\simeq 0.0008\%$, as shown in Figure A.3. We see also that a

[2]https://www.labsphere.com/wp-content/uploads/2021/07/Spectralon.pdf

great deal of the light is lost to absorption within the sphere - with light incident on the inner sphere surface - or light incident on the fiber cladding.

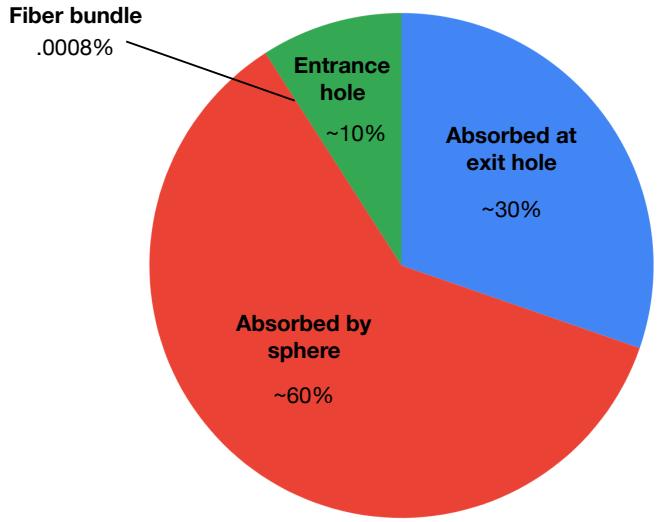

Figure A.3: Distribution of fates of 10^6 photons entering the integrating sphere. We use this result to determine approximately how many photons enter the fibers.

The light then travels to the spectrograph where it interacts with three reflective mirrors with a protected silver coating with an efficiency curve shown in Figure A.5, found in the Andor Kymera 328-i specifications manual. Here we also must account for a mismatch between the f/#s of the fiber and the first mirror in the spectrograph, f/2.4 and f/4.1, respectively. We take the ratio of the f/#s to determine how much light is lost, as the collecting area of the collimator mirror is smaller. We also consider the efficiency of the grating (matching the grating settings to that of a given PEAS spectrum). In the case presented here, we use the lowest resolution grating with ruling of 150 l/mm and a blaze angle of 800 nm. This grating has a wavelength

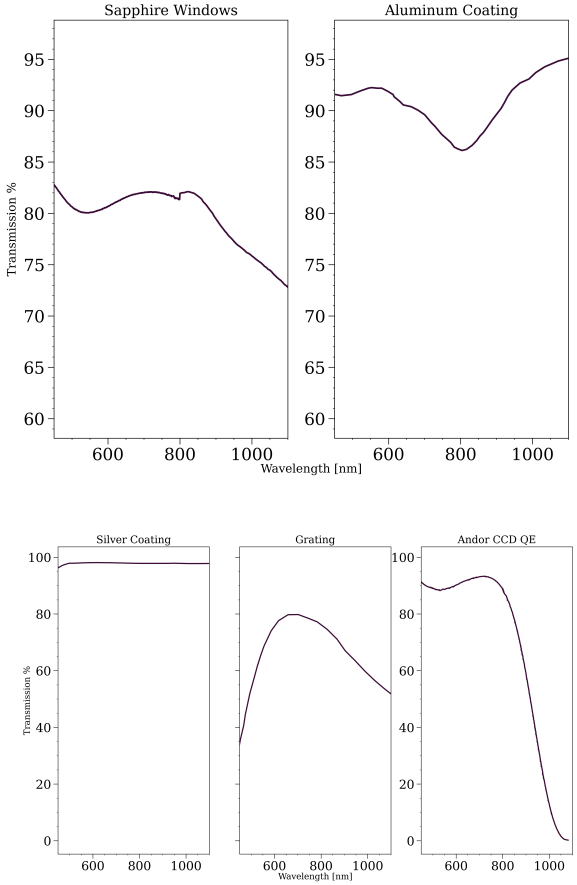

Figure A.4

Figure A.5: From left to right: Transmission of the four sapphire windows, reflectance of the aluminum and silver coatings used on spectrograph optics, and, finally, the quantum efficiency of the *Andor* CCD.

coverage of $\approx 500 - 1100nm$. Finally, the light hits the Andor iDus-420 CCD [3] and produces digital numbers which we measure as counts. We include the Andor quantum efficency (QE) and AR coating into our throughput model.

We pass the throughput simulation a sample spectrum of Jupiter provided by Pat Irwin and combined by Michael Cushing (taken with the Galileo Near-Infrared Mapping Spectrometer (NIMS)). The spectrum is given in units of W cm^{-2} sr^{-1} μm^{-1}. To convert these units we pull the date and associated ephemeris for the observations from JPL Horizons in order to determine Jupiter's angular size and distance from Earth. We also account for the energy conversion, to convert into photons s^{-1}. We test a section of the spectrum within a wavelength range of $0.7 \leq \lambda \leq 1$ micron. We also apply atmospheric corrections, using a telluric model for Lick Observatory produced by the PypeIt Telluric Fitter (Figure A.6;Prochaska et al. (2020); Prochaska et al. (2020)). We then complete the unit conversion and finally apply the gain, which we found to be 2.66 e^-/AD.

After interpolating the test spectrum onto the CCD's grid, we produce a final spectrum in units and pixel (wavelength) space that match those of the PEAS spectrum shown in Figure A.7.

A.2.2 Findings

With this model we are able to recreate the observed PEAS spectrum to within a factor of 10 (see Figure A.7). The model overestimates the efficiency of the system in some, at this point unknown, regard. Some possible components where we are overestimating efficiency include the Spectralon coating, optics coatings, or the fiber coupling to the spectrograph. As shown in Figure A.7, the total throughput of the entire system is $\simeq 0.0008\%$. This current optical design is highly inefficient compared to standard spectrograph throughputs of a few percent, and we suggest that upgrades be made to the optical design of the PEAS back-end to increase the

[3] https://andor.oxinst.com/assets/uploads/products/andor/documents/andor-idus-420-specifications.pdf

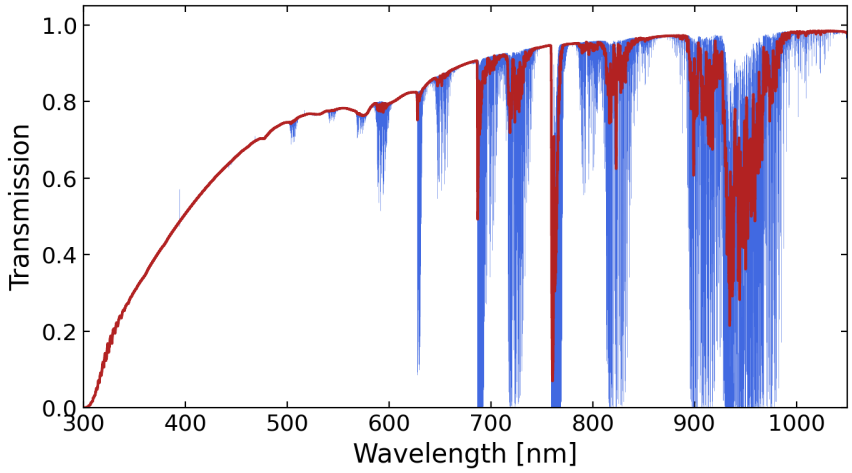

Figure A.6: Telluric transmission spectrum for Lick observatory, produced by the PyepIt Telluric Fitter (**?**Prochaska et al., 2020; Prochaska et al., 2020), with the high-resolution model in blue and the smoothed model shown in red.

throughput of the instrument. We outline those upgrades in the following section.

A.3 Upgrades to the PEAS optical design

To increase the throughput of the PEAS system, we explored two options for a new design to replace the integrating sphere component with an aspheric or achromatic lens placed just beyond the focal plane, to create a pupil plane at the back end of the telescope, where we will place a new fiber bundle (see Figure A.8). The pupil plane also produces disk-integrated light, and by matching the NA of the pupil plane to the NA of the fibers, we can achieve significantly more throughput compared to the original PEAS design.

With a goal of matching the NA and circumference of the fiber bundle while maximizing efficiency over the wavelengths of interest ($\approx 400 - 1000$ nm), the lenses chosen have radii between 6-12 mm and focal lengths of 10-12 mm. The resulting pupils have diameters that are

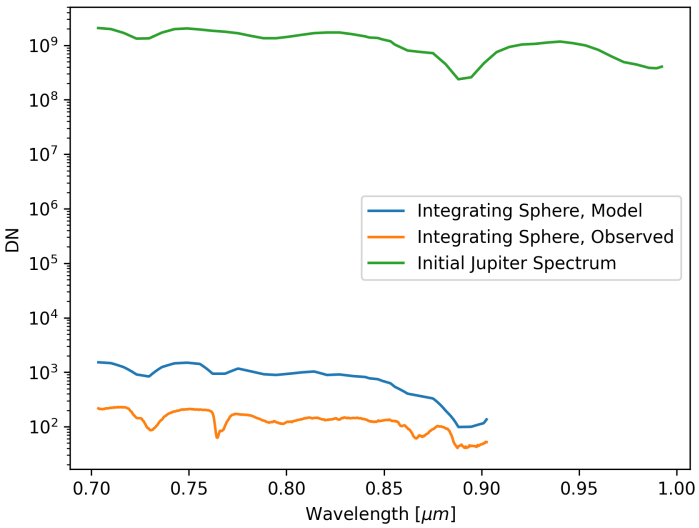

Figure A.7: A comparison of the initial and final Jupiter spectrum in units of photons. The initial Jupiter spectrum from NIMS is shown in *green*. In *blue*, we show the modeled Jupiter spectrum after it has passed through the PEAS setup including the telescope, back-end optics, spectrograph, and CCD. In *orange*, we show the observed PEAS spectrum of Jupiter. The model is within a factor of 10 of our observed spectrum. The overall efficiency loss including the atmosphere and instrument is $\sim 10^7$.

just above or below the diameter of the fiber bundle (1.8 mm and 1.4 mm, compared to 1.6 mm, respectively; see Figure A.9)). There is a slight difference in overall throughput whether the setup under- or over-fills the fiber bundle, but it is very slight (see Figure A.10).

We will also be installing a new custom fiber bundle (NA=0.32) with 36 fibers - each having a 68 micron core with a total outer diameter of 120 microns. This new fiber will improve spectral resolution, and the length of the fiber will be increased in order to wrap around the telescope whereas it previously had to be removed from the instrument in order to slew without damaging the fiber.

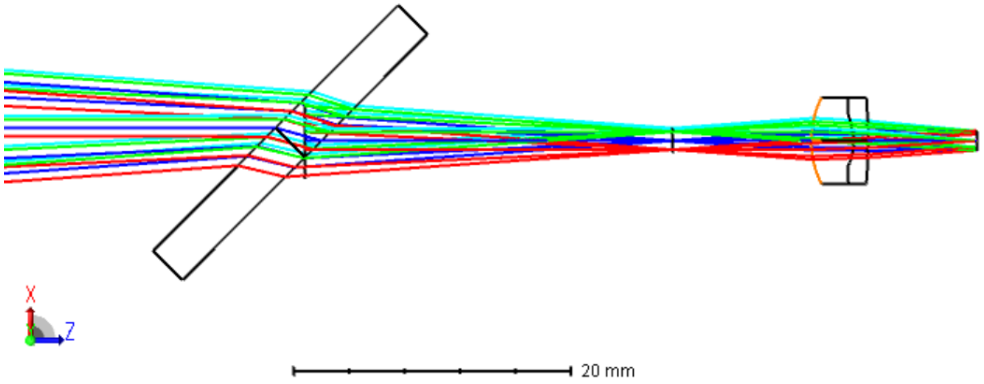

Figure A.8: A Zemax raytrace model for the upgraded PEAS design. At left is the final sapphire window. Instead of the integrating sphere at the focal plane, an achromat produces a pupil plane at far right. A new fiber bundle will be placed at the pupil plane to collect disk-integrated light and send it to the spectrograph.

We incorporate these new specifications and possible optical designs into the system throughput model and plot the resulting spectra in comparison to the integrating sphere design and the measured PEAS spectrum (shown in Figure A.10). We see an increase in throughput of a factor ≈ 10000, better matching the initial flux of the input spectrum–we lose far less light when we replace the integrating sphere with the pupil imager. There is only a slight difference between the throughput for the different types of lenses, but the achromatic lens does produce slightly higher throughput than the aspheric lens. We decide that an achromatic lens with a 6.25 mm diameter and 10 mm focal length and VIS-NIR coating from Edmund optics is the best choice for executing the upgrade. This lens will allow us to meet all of the needs required by the upgrade and parameters of the current system.

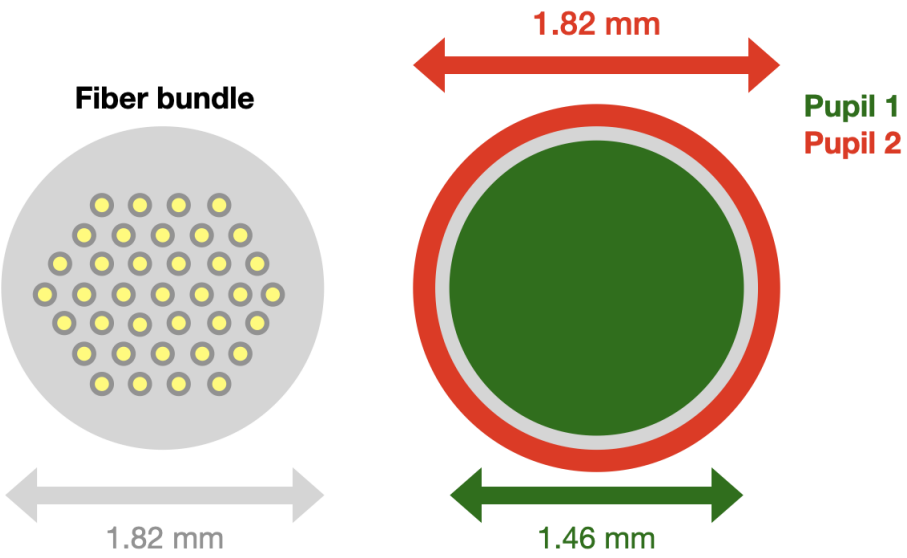

Figure A.9: Comparisons of the beam footprints relative to the size of the fiber bundle. The red shows the achromat footprint with overfills the bundle the the green shows the asphere which underfills the bundle. There is a slight throughput difference as shown in Figure A.10.

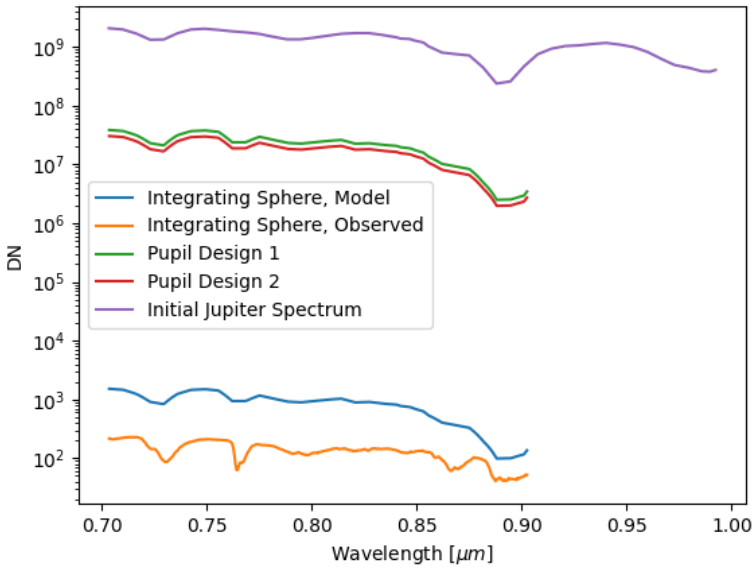

Figure A.10: Throughput of 3 different optical designs of the PEAS system. The planned upgrades increase the modeled throughput by ≈ 2 orders of magnitude over the current integrating sphere design.